Development of Novel Aerogel-Copper Composite Electrodes for Enhanced Electrochemically Mediated Amine Regeneration (EMAR) Based CO_2 Capture Using Photocatalysis

Md Akibul Halim

A THESIS SUBMITTED TO THE FACULTY OF GRADUATE STUDIES

IN PARTIAL FULFILMENT OF THE REQUIREMENTS

FOR THE DEGREE OF

MASTER OF APPLIED SCIENCE

GRADUATE PROGRAM IN MECHANICAL ENGINEERING

YORK UNIVERSITY

TORONTO, ONTARIO

APRIL 2026

Abstract

Electrochemically Mediated Amine Regeneration (EMAR) is an alternative to thermal amine scrubbing because solvent regeneration is driven by electricity rather than heat. In EMAR, CO_2 absorbed by an amine solvent is released by electrochemically generated Cu^{2+} ions that compete with the amine for CO_2, enabling regeneration without heat input. However, practical systems remain limited by charge-transfer resistance and mass-transport constraints.

This work investigates TiO_2 aerogel–modified copper foam electrodes for photo-assisted EMAR operation. TiO_2 aerogel powder was deposited on copper foam using APTES-assisted dip coating. Material structure and surface chemistry were characterized using SEM, XRD, XPS, BET, and microCT. Electrochemical performance was evaluated under dark and UV conditions. The three-cycle coated electrode (TCF3) showed lower regeneration energy and higher Faradaic efficiency than copper plate and bare copper foam electrodes. UV illumination enhanced electrochemical activity at lower current densities, demonstrating improved EMAR electrode performance.

Acknowledgements

I would like to express my gratitude to my supervisor, Professor Marina Freire-Gormaly, for her invaluable guidance, encouragement, and continuous support throughout this research. Her expertise, insight, and commitment to scientific rigor greatly influenced the direction of this work and helped shape my development as a researcher. I am especially grateful to her for her patience, constructive feedback, and encouragement during the challenges of this project. I am also grateful for the opportunity to participate in three international conferences, including one as a conference presenter at the Electrochemical Society Conference in Montreal in May 2025. Also, her leadership to enable me to experience enriching scientific research experiences at research collaborators research facilities, and a professional development training course at the Walkerton Clean Water Centre greatly increased my professionalism and complemented my Master's research program.

I would also like to extend my sincere appreciation to my postdoctoral mentor, Dr. Robert Liang, for his technical guidance, insightful discussion, and support throughout the experimental stages of this research. His expertise in troubleshooting experimental problems and finding valuable feedback on electrochemical analysis greatly contributed to the successful completion of this research.

I am also grateful to my thesis committee member, Prof. Solomon Boakye-Yiadom for his guidance and helpful review of my research. I also appreciate my thesis defense committee member, Prof. Chris Caputo's helpful critique of my thesis.

During my thesis program, I had the distinct privilege of conducting material characterization at a research collaborator's research facility, using the high quality and unique scientific facilities was a highlight of my research experience.

I would like to acknowledge the funding support I received to do this research through the generous funding from the Natural Sciences and Engineering Research Council of Canada (NSERC) for the NSERC Discovery Grant (Number: RGPIN-2020-06087), Natural Resources Canada (NRCan) through the Energy Innovation Program (Number: CCUS-CAP-088), the York University Lassonde School of Engineering Graduate Student Fellowship, the Department of Mechanical Engineering Research Presentation Best Master's Video Award, and the YUGSA Conference Travel Award.

My sincere thanks also go to my lab mates and colleagues in the Freire-Gormaly research group for their support. Their willingness to share knowledge, provide feedback, and assist with experimental work made the research both productive and enjoyable.

I would also like to express my deepest gratitude to my family and friends for their unwavering encouragement, patience, and support throughout my academic journey. Their belief in me has been a constant source of motivation and strength.

This work would not have been possible without the support and contributions of all the individuals mentioned above.

Table of Contents

List of Figures

List of Abbreviations

CCUS	Carbon Capture, Utilization, and Storage
EMAR	Electrochemically Mediated Amine Regeneration
TAP	TiO_2 Aerogel Powder
MEA	Monoethanolamine
TSA	Temperature Swing Adsorption
PSA	Pressure Swing Adsorption
VSA	Vacuum Swing Adsorption
ESA	Electrical Swing Adsorption
CV	Cyclic Voltammetry
EIS	Electrical Impedance Spectroscopy
TCF	TiO_2 Aerogel-coated Copper Foam
TCF1	1-Time TiO_2 Aerogel-powder Dip-coated Copper Foam
TCF3	3-Times TiO_2 Aerogel-powder Dip-coated Copper Foam
TCF5	5-Time TiO_2 Aerogel-powder Dip-coated Copper Foam
TCF7	7-Times TiO_2 Aerogel-powder Dip-coated Copper Foam
EDA	Ethylenediamine
FE	Faradaic Efficiency
RE	Regeneration Energy
CP	Copper Plate
CF	Copper Foam
TTIP	Titanium Isopropoxide
APTES	(3-aminopropyl)triethoxysilane
TGA	Thermogravimetric Analysis
LDPSA	Laser Diffraction Particle Size Analysis
SEM	Scanning Electron Microscopy

BET	Brunauer Emmett Teller
DFT	Density Functional Theory
TEM	Transmission Electron Microscopy
XRD	X-Ray Diffraction
XPS	X-ray photoelectron spectroscopy
ECSA	Electrochemically Active Surface Area

Chapter 1 Introduction

1.1 Background and Motivation

Anthropogenic CO_2 emissions are among the dominant contributors to the greenhouse effect. Although it constitutes only a small fraction of the atmosphere, it accounts for approximately 70% of the overall greenhouse effect [1]. A 30% increase in atmospheric CO_2 concentration since 1950 has brought it to 410 ppm. This is the highest observed CO_2 concentration in the last 800,000 years [1]. This rapid rise is directly linked to global warming, ocean acidification, and large-scale ecosystem disruption. Climate models have predicted that the global mean temperature is likely to increase by 1.5 °C between 2030 and 2052 if current emissions trends persist [2,3].

From 1970 to 2018, global anthropogenic CO_2 emissions increased from approximately 16 GT/Year to 37.5 GT/year. The present-day emissions remain at 33 GT/year, which far exceeds the sequestration capacity of the natural carbon sinks [4,5]. While aggressive emission reduction strategies are essential, mitigation alone is insufficient to stabilize atmospheric CO_2 concentrations. As a result, Carbon Capture, Utilization, and Storage (CCUS) is widely recognized as a necessary component of long-term decarbonization pathways.

CCUS has progressed from transitional technology to a necessary component of negative-emissions pathways. Large-scale demonstrations and carbon capture projects indicate accelerating deployment interest [6–9]. However, the traditional post-combustion capture platform, aqueous amine scrubbing, remains constrained by several fundamental thermodynamic, kinetic, and process-related limitations. These include high regeneration energy demand (arising from the strong carbamate bond enthalpy and sensible heat requirements), solvent degradation (driven by thermal and oxidative pathways that reduce amine capacity), corrosion (induced by the high

basicity of the solvent), and overall complexity associated with solvent management [10]. These limitations motivate intensified capture concepts that preserve the selectivity and maturity of amine chemistry while reducing regeneration energy and improving operational flexibility [11,12].

Electrochemically Mediated Amine Regeneration (EMAR) has emerged as a promising alternative to traditional thermal amine regeneration. Conventional CCUS systems are currently dominated by post-combustion amine scrubbing. Here, CO_2 is absorbed into an aqueous amine at 40-60 °C and regenerates via thermal stripping at 120-140 °C. This regeneration step is the primary energy-intensive stage due to the combined requirement of sensible heat, latent heat of vaporization, and the enthalpy of CO_2-amine bond dissociation. Improvement in CCUS thus focuses on solvent development, process intensification, and alternative regeneration pathways to reduce energy consumption while maintaining high CO_2 loading and selectivity. Within this framework, EMAR replaces the traditional thermal stripping with an electrically driven redox-mediated cycle that operates near ambient conditions. This enables improved process flexibility and compatibility with renewable electricity sources, while also facilitating retrofit integration into existing industrial systems [13,14]. In this thesis, EMAR is further enhanced through electrode functionalization using TiO_2 aerogel powder (TAP). The introduction of sunlight illumination as a performance-enhancing element is intended to improve charge transfer, copper redox kinetics, regeneration energy, and Faradaic efficiency without altering the fundamental EMAR chemistry.

1.2 CO_2 Capture Technologies

Industrial CO_2 capture is commonly categorized into pre-combustion, oxy-fuel combustion, and post-combustion pathways [15,16]. Pre-combustion capture removes CO_2 from pressurized synthesis gas. However, this often enables physical solvents and favorable thermodynamics but requires major process reconfiguration, which limits retrofit applicability [17,18]. Oxy-fuel

combustion produces a CO_2-rich flue stream by combusting fuel in oxygen. This simplifies separation but imposes a substantial energy penalty associated with oxygen production and introduces integration challenges at scale [19,20].

Post-combustion carbon capture remains the most widely accepted route because it is easy to retrofit into existing plants. Among post-combustion options (absorption, adsorption, membranes, cryogenic separation), amine-based absorption is the most mature and commercially implemented due to its high CO_2 selectivity at low partial pressures [10,21]. Nevertheless, for the amine absorption system, the energy requirement for solvent regeneration is the dominant operating penalty, efficiency loss, and cost [22]. Consequently, advanced solvent formulations (blends [23], phase-change systems [24]) and regeneration strategies (catalytic [25], electrochemical [26]) have been developed to address these limitations while maintaining robust capture.

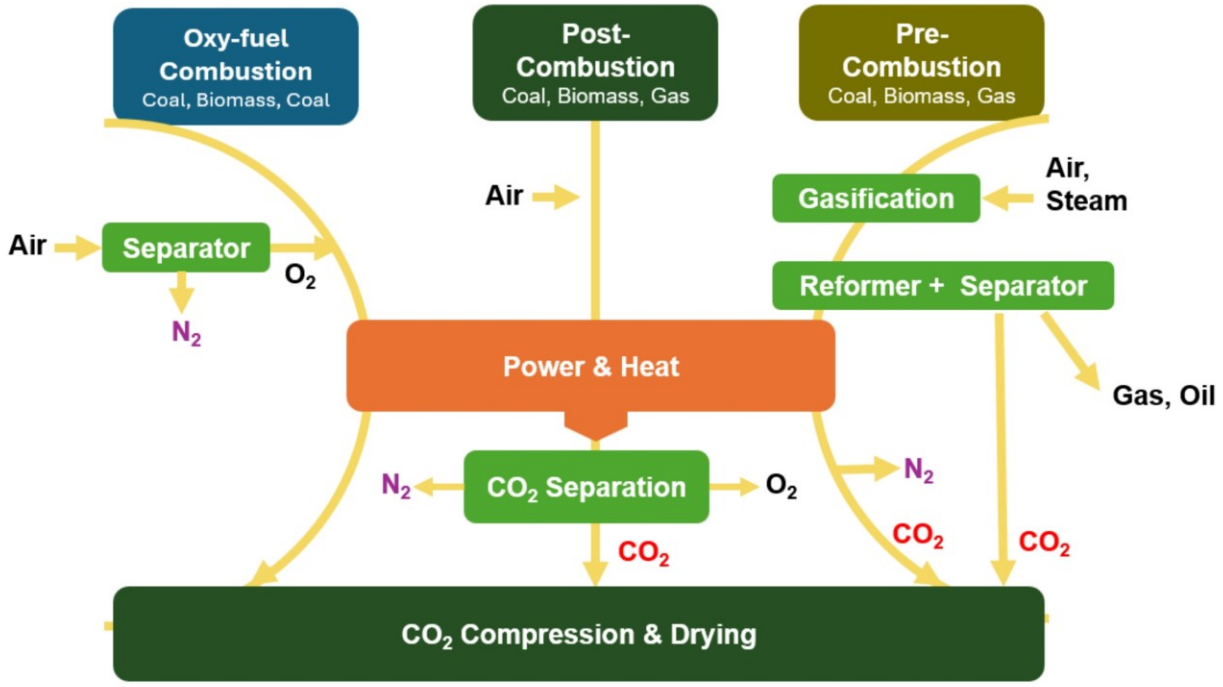

Figure 1: Schematic illustration of the three main CO_2 capture pathways: pre-combustion, oxy-fuel combustion, and post-combustion technologies.

1.3 Conventional Amine Regeneration

In conventional post-combustion absorption, CO_2 is absorbed into an aqueous amine solvent in an absorber and then released in a stripper via thermal regeneration, typically at elevated temperature [22,27]. The primary and secondary amines tend to form carbamate, while the tertiary amines tend to promote the formation of bicarbonate [28,29]. While monoethanolamine (MEA) remains a benchmark solvent due to kinetics and commercial familiarity, the regeneration step is energy-intensive because it must supply (i) sensible heat to raise solvent temperature, (ii) reaction enthalpy to reverse chemically bound CO_2, and (iii) latent heat associated with water vaporization and stripping [30,31].

Operationally, these conventional systems also need to address solvent management challenges, including oxidative and thermal degradation, corrosion, and emissions control. These challenges increase solvent replacement rates and reduce the effective capture over time, particularly under typical operating temperature of 120-140 °C required for the CO_2 desorption [32,33]. At these high temperatures, amine solvents undergo thermal degradation. These take place through irreversible side reactions, such as carbamate polarization and heat-stable salt formation. Simultaneous oxidative degradation further reduces the number of active amine sites and promotes the formation of corrosive byproducts. As a result, significant amounts of research have been focused on blending amines, catalysts, and additives that can reduce the regeneration energy and accelerate desorption kinetics [34,35]. However, these approaches continue to rely on bulk thermal regeneration. Therefore, they require an integrated steam cycle or large-scale heat-transfer equipment.

Beyond solvent chemistry modifications, regeneration can also be achieved by cyclic variations of operating conditions, commonly referred to as swing processes. These include temperature swing adsorption (TSA), pressure swing adsorption (PSA), vacuum swing adsorption (VSA), and electric swing adsorption (ESA). Each of these methods relies on external thermal, mechanical, or electrical inputs to reverse CO_2 binding and regenerate the capture medium [36,37]. Figure 2 schematically compares these regeneration strategies, highlighting their operating principles and associated energy inputs.

Swing-based regeneration approaches offer flexibility and have been widely studied. However, their dependence on thermal energy, pressure reduction, or vacuum generation continues to impose energy penalties and system complexity. This motivates interest in alternative regeneration pathways that decouple CO_2 release from bulk thermal swings.

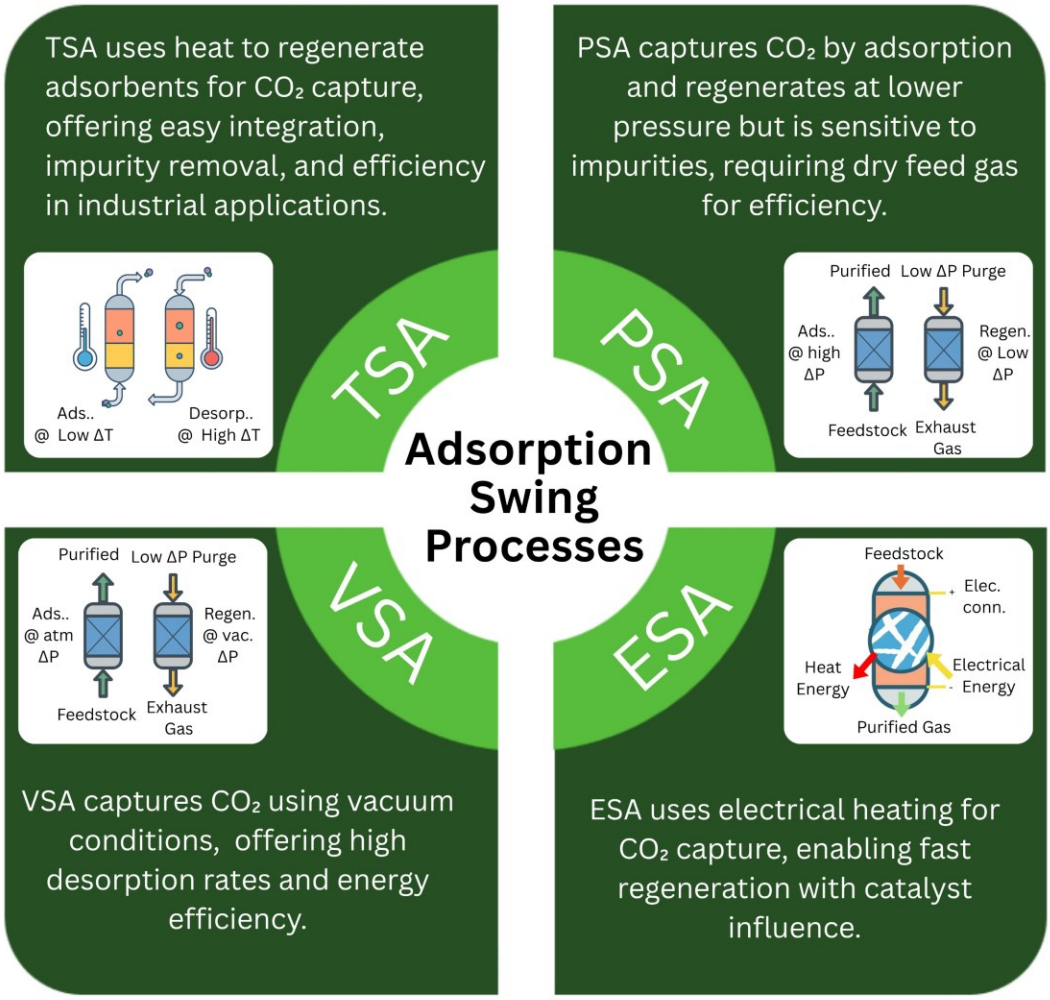

Figure 2: Schematic illustration of different adsorption swing regeneration processes used for CO_2 capture, including temperature swing adsorption (TSA), pressure swing adsorption (PSA), vacuum swing adsorption (VSA), and electrical swing adsorption (ESA).

1.4 Electrochemically Mediated Amine Regeneration (EMAR)

EMAR replaces the thermal strip with an electrochemically driven redox cycle. In EMAR, CO_2 is absorbed in a conventional absorber, and desorption is induced by the electrochemical oxidation of copper at the copper anode, which generates Cu^{2+}. This Cu^{2+} replaces CO_2 in the carbamate, forming a two-phase mixture of an amine-copper complex and CO_2. The CO_2 is

separated from this mixture in the desorber while the Cu^{2+} of the amine-copper complex gets reduced at the copper cathode, regenerating the free amine and completing the cycle [26].

As the regeneration driving force is electrical rather than thermal, EMAR is compatible with low-temperature operation. This reduces the reliance on steam and improves the retrofit feasibility [13,38]. System-level performance depends on coupled phenomena: (i) Cu^{2+}/Cu^{0} redox kinetics at electrode surfaces, (ii) amine–Cu coordination equilibria, (iii) mass transport of copper species and amine complexes, and (iv) cell ohmic losses and membrane/diaphragm transport. The net energy consumption and Faradaic efficiency are therefore governed not only by thermodynamics but also by kinetic overpotentials and transport resistances, which increase the cell voltage at a given current [39].

Recent EMAR studies have explored system design and operating conditions for flue-gas capture, including performance benchmarking, stability considerations, and solvent selection [40]. Although these developments have substantially improved the EMAR system, further improvements are needed in practical cell operation to reduce polarization losses, maintain high Faradaic efficiency across a range of current densities, and mitigate performance decay.

1.5 Photocatalysis and Aerogel Integration

Photocatalytic materials and structured porous solids have also been extensively studied. They can modify interfacial charge-transfer behavior, enhance transport through a high-surface-area network, and interact with light to influence the local reaction environment. Specifically, aerogels are an attractive option for electrode modification due to their interconnected high accessible surface area [41,42]. Aerogels have also been used for the amine functionalization and the light-assisted desorption concept [43,44]. Light can be used to reduce external energy input when coupled to an appropriately designed sorbent system.

In the present work, TiO_2 aerogel powder is used as a coating on EMAR cell electrodes and operated under UV light. The presence of TiO_2 and light improves interfacial charge transfer, decreases polarization losses, and facilitates mass transport and Cu redox kinetics, thereby reducing the regeneration energy and faradaic efficiency. At the same time, copper-mediated complexation remains the primary pathway for CO_2 release. Accordingly, TiO_2 and UV are not considered standalone photocatalytic routes for CO_2 conversion. They are employed to enhance electrochemical performance and improve overall EMAR performance.

1.6 Research Gap

The EMAR process is a promising alternative to traditional thermally driven regeneration. It shows the potential to lower the energy of regeneration and reduce solvent degradation. Prior studies of the EMAR system have explored system-level energetics [45,46], demonstrated bench-scale operation using both conventional amines and high-capacity polyamine solvents [40]. These investigations collectively confirm that EMAR can perform the CO_2 desorption without any high-temperature operations while maintaining effective capture performance.

Despite this progress, reported EMAR performance remains strongly influenced by electrochemical polarization losses, non-uniform current distribution, and mass transport limitations within the electrochemical cell [39,47]. These factors directly impact cell voltage, faradaic efficiency, and overall regeneration energy. This highlights the critical role of electrode structure and interfacial charge-transfer behavior in determining system performance. While extensive studies have been conducted on solvent chemistry and redox reactions, limited attention has been paid to electrode-level strategies to mitigate these electrochemical limitations.

In contrast, porous aerogels and light-assisted systems have also been shown to enhance the interfacial transport, surface accessibility, and charge transfer processes in electrochemical and

CO_2- related applications [41,44]. Aerogels provide an interconnected pore network and high surface area, while photo-assisted effects can improve the utilization of electrons under UV light and reduce overpotential. However, these approaches have not been integrated into the EMAR system, nor has their quantitative evaluation been conducted for the system's regeneration energy and Faradaic efficiency.

Accordingly, a clear research gap exists for the EMAR electrochemistry, electrode architecture, and photo-assisted enhancement. Specifically, few experimental studies examine how the TiO_2 aerogel-coated electrode operates under UV illumination, how it influences electrochemical behavior, and how it enhances the overall EMAR process while preserving the fundamental copper-amine regeneration mechanism.

1.7 Thesis Objectives

The primary objective of this thesis is to enhance the performance of the EMAR system by integrating the TiO_2 aerogel powder coating on the EMAR cell electrode. By applying UV illumination, the aim is to reduce the energy required for regeneration and improve faradic efficiency while preserving the fundamental EMAR chemistry.

The specific objectives of this work are to:

1. Synthesize and characterize TiO_2 aerogel–integrated copper foam electrodes, with high surface area, photo-assisted charge transfer capability, and electrochemical stability.
2. Evaluate electrochemical and photo-assisted electrochemical performance using cyclic voltammetry (CV), electrochemical impedance spectroscopy (EIS) analysis under dark and illuminated conditions.

3. Assess the performance of TiO_2 aerogel-coated copper foam (TCF) electrode in EMAR through quantified regeneration energy and faradic efficiency

1.8 Thesis Structure

This thesis is organized into five chapters. Chapter 1 introduces the motivation for CO_2 capture, reviews post-combustion capture technologies, and presents the principles of electrochemically mediated amine regeneration. It then identifies the research gap and the objectives of this work. Chapter 2 provides the theoretical background on amine-based CO_2 capture, EMAR chemistry and system design, aerogel materials, and photo-assisted electrochemical enhancement relevant to the present study. Chapter 3 details the experimental methodology, including electrode fabrication, electrochemical cell configuration, material and electrochemical characterization, and CO_2 absorption–desorption procedures. Chapter 4 presents and discusses the experimental results, focusing on electrode characterization, electrochemical performance, CO_2 desorption behavior, regeneration energy, and Faradaic efficiency. Finally, Chapter 5 summarizes the key findings, outlines the contributions and limitations of this work, and provides recommendations for future research.

Chapter 2 Background

2.1 Amine-based CO_2 capture

Amine-based CO_2 capture remains the most mature and widely implemented technology for post-combustion CO_2 capture due to its high selectivity towards CO_2 and its compatibility with large-scale industrial flue gas streams [22]. In this approach, CO_2 is selectively absorbed by the amine sorbent and then released during regeneration, making it suitable for cyclic operations. Extensive pilot plant testing and commercial deployment have made amine scrubbing a benchmark technology for post-combustion CO_2 capture, especially in power plants and energy-intensive sectors [48,49].

The performance of an amine-based system depends on chemical equilibria, absorption kinetics, and mass-transfer characteristics. Although amine-based absorption has high CO_2 capture efficiency, it still requires substantial regeneration energy due to the thermal regeneration step. This motivates the ongoing research to improve the solvent formulations and alternative regeneration energy [50] .

2.1.1 Amine Chemistry and CO_2 Absorption Mechanisms

For primary and secondary amines, CO_2 absorption proceeds through a series of elementary reactions. In these reactions, the nucleophilic amine nitrogen attacks the electrophilic carbon atom of CO_2. This initial interaction leads to the formation of charged intermediate species. This mechanism is commonly described as a zwitterionic mechanism, in which CO_2 reacts with an amine to form an unstable, internally charged zwitterionic species that undergoes deprotonation to yield a stable carbamate.

The overall reaction can be represented as:

$$RNH_2 + CO_2 \rightleftharpoons RNHCOO^- + H^+ \quad (1)$$

Followed by a proton transfer to a second amine molecule:

$$RNH_2 + H^+ \rightleftharpoons RNH_3^+ \quad (2)$$

resulting in an overall stoichiometry of approximately 0.5 mol CO_2 per mol amine, which limits theoretical loading capacity [30,51]. Monoethanolamine (MEA) is considered a benchmark solvent due to its high reactivity towards CO_2 and fast absorption kinetics [52].

Secondary amine follows a similar carbamate formation pathway. However, stearic hindrance can reduce carbamate stability, partially shifting the absorption towards bicarbonate formation. This increases the cyclic capacity in a certain solvent system [53].

In contrast, tertiary amines do not form stable carbamates. Instead, they promote CO_2 absorption through base-catalyzed hydration to bicarbonate [54]:

$$CO_2 + H_2O \rightleftharpoons HCO_3^- + H^+ \quad (3)$$

$$R_3N + H^+ \rightleftharpoons R_3NH^+ \quad (4)$$

This pathway allows higher theoretical CO_2 loading. However, it shows relatively slower absorption kinetics compared to the primary amine [54,55].

Polyamines such as ethylenediamine (EDA) contain multiple amine functionalized groups. This allows them to form both carbamate and bicarbonate simultaneously, thereby enhancing absorption capacity and accelerating reaction kinetics. However, higher reaction sites increase the required heat of absorption, which ultimately increases the overall regeneration energy requirement [28].

2.1.2 Degradation and Energy Penalties in Traditional Systems

In conventional amine-based CO_2 capture systems, solvent regeneration is achieved by raising the solvent temperature to break the chemical bond between CO_2 and the amine. The total regeneration energy demand is composed of three principal contributions: sensible heat required to raise solvent temperature, reaction enthalpy associated with breaking CO_2–amine bonds, and latent heat losses due to solvent vaporization [56]. Collectively, these contributions result in high reboiler heat duty and impose a significant efficiency penalty on capture systems.

Thermal regeneration also accelerates the amine degradation through both oxidative and thermal pathways. Oxidative degradation occurs via dissolved oxygen and flue-gas contaminants. Thermal degradation occurs through the high operating stripping temperature. These degradations lead to irreversible degradation products and heat-stable salts [32].

In addition, acid gases and trace contaminants in the flue gas can also react with the amine and form nitrosamines and nitramines. This raises environmental and regulatory concerns. These degradation processes increase the corrosion rates and shorten the solvent lifetime, further increasing the operating costs [57].

As a result, the combination of high regeneration energy demand and solvent degradation remains the principal limitation of traditional amine-based CO_2 capture systems. These challenges have driven the development of alternative solvent formulations, catalytic regeneration strategies, and non-thermal regeneration approaches to reduce energy consumption while maintaining robust capture performance.

2.2 Electrochemically Mediated Amine Regeneration (EMAR)

Electrochemically mediated amine regeneration (EMAR) is an alternative approach to traditional thermally driven amine regeneration. Instead of elevating the solvent temperature, it electrically drives the regeneration process. In EMAR, absorption occurs in a conventional absorber. However, regeneration occurs by altering the amine's coordination environment, enabling CO_2 release at near-ambient temperature. This fundamental distinction allows EMAR to mitigate many of the energy and degradation challenges associated with the traditional thermal stripping [58].

The EMAR concept is based on competitive coordination between CO_2- bound amine and electrochemically generated metal ions, most commonly the Cu^0/Cu^{2+} redox couple. The applied potential or current governs the metal ion generation, which in turn reversibly alters amine coordination for cyclic CO_2 capture and release [58,59].

2.2.1 Cu–Amine Coordination Chemistry

The main mechanism of EMAR relies on the strong affinity of Cu^{2+} towards the amine ligands. During electrochemical oxidation, Cu metal oxidizes to Cu^{2+} ions.

$$Cu \rightarrow Cu^{2+} + 2e^- \quad (5)$$

This anodic dissolution creates Cu^{2+} ions in situ, which shows a strong affinity towards nitrogen-containing ligands such as ethylenediamine (EDA) [13]. The Cu^{2+} ions generated react with free amine molecules to form amine-Cu complexes in solution.

$$Cu^{2+} + EDA \rightleftharpoons [Cu\ (EDA)_n]^{2+} \quad (6)$$

In aqueous amine solution, this coordination shifts the equilibrium away from amine-CO_2 complexes. As a result, CO_2 is released from the solvent, whether it is present as carbamate or

bicarbonate. This process is best described as an equilibrium shift rather than a single-step reaction, because Cu^{2+} binds preferentially to the amine and releases CO_2 in a manner that depends on amine coordination and solution conditions [13,26].

EDA contains more than one amine group, which makes it easier for Cu^{2+} to bind with EDA more strongly than monoamines such as MEA. This stronger bond promotes the formation of more stable amine-Cu complexes and enhances CO_2 release during the electrochemical reaction [40,60]. Consequently, the EMAR system containing polyamine has shown better efficiency than the monoamine-based system under comparable conditions [40,60].

Following CO_2 release, the electrochemical cycle is completed by reducing Cu^{2+} back to metallic copper at the cathode.

$$Cu^{2+}+2e^{-}\rightarrow Cu^{0} \quad (7)$$

This reduction step regenerates both the copper electrode and the amine. This amine can be reused for repeated CO_2 absorption [13]. Because Cu^{2+}-amine coordination is reversible and does not require elevated temperatures, EMAR significantly reduces the energy required for regeneration compared with other thermally driven processes [39].

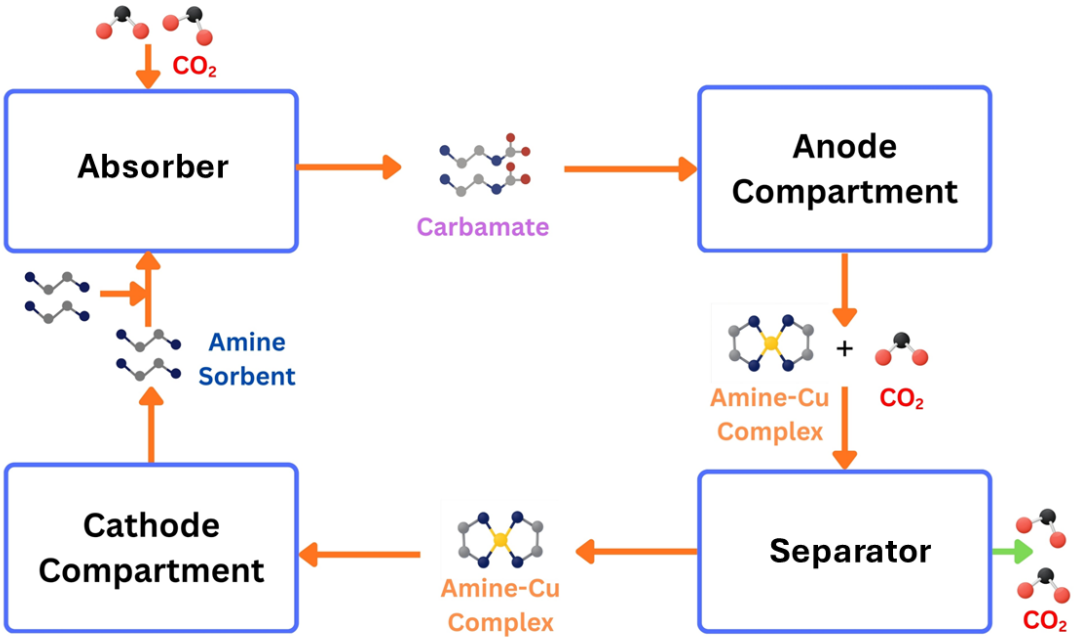

Figure 3: Block diagram illustrating the working principle of electrochemically mediated amine regeneration (EMAR) for CO_2 capture.

Conventional EMAR systems have demonstrated Faradaic Efficiency of 70-90%, and regeneration energies of 40-100 kJ/mol CO_2. These performances depend on the operating conditions and the system design [26]. These values represent a significant improvement over traditional thermal amine regeneration, which typically requires higher energy input due to sensible and latent heat demands.

In this work, the baseline performance was obtained using copper plate (CP) and copper foam (CF) electrodes. These performances were affected by multiple factors, such as electrochemical cell configuration, electrode morphology, electrolyte conductivity, mass transport limitations, and Cu-amine coordination kinetics. These combined system-level constraints resulted in lower faradaic efficiency and regeneration energy compared to the relative literature benchmarks. Nevertheless, the introduction of TiO_2 aerogel-coated copper foam (TCF3) under UV

illumination demonstrated a clear relative improvement in the performance. This enhancement is attributed to improved charge transfer, enhanced Cu redox kinetics, and reduced interfacial resistance, highlighting the effectiveness of the proposed electrode modification strategy within the given system limitations.

2.2.2 Cell Design, Electron Utilization, and Energy Efficiency

Both chemistry and electrochemical cell behavior govern the performance of the EMAR system. In an ideal EMAR cell, CO_2 is released by the copper electrochemical cycle. That means the applied electrical current is effectively used to trigger the reversible copper reaction that triggers the desorption of CO_2 from the solvent [45]. Under these conditions, the amount of CO_2 released is proportional to the amount of total charge passed, which is consistent with Faraday's law.

The overall required electrical energy depends on the applied current and voltage. The measured cell voltage includes not only the energy required for copper redox reactions, but also additional voltage losses associated with electrode kinetics, electrical resistance within the cell, and mass transport limitations [39,61]. These losses are due to the activation overpotential, ionic resistance in the electrolyte and membrane, and concentration polarization near the electrode surfaces. These make the cell's performance strongly dependent on the electrode design and operating conditions.

Electron utilization is commonly measured through Faradaic efficiency. It represents the percentage of the total charge that contributes directly to CO_2 desorption. In EMAR, Faradaic efficiency is defined with respect to the CO_2 release event [13]. Deviations from this ideal behavior can result from nonproductive copper cycling, uneven current distribution, or parasitic reactions, which increase energy consumption without contributing to regeneration [39,62].

Compared to thermal regeneration, EMAR enables CO_2 desorption by electrical work at ambient temperature. This results in a substantially lower energy regeneration as it replaces the thermal heating [13,63]. The cell's efficiency, therefore, depends heavily on optimizing the cell structure, electrode surface area, and mass-transfer effectiveness. This will reduce the polarization losses and will support the stable operation at higher current density [45].

2.2.3 Prior EMAR Developments and Limitations

Initially, the EMAR was introduced as an alternative to thermally driven regeneration. It demonstrated that CO_2 desorption can be achieved through the redox cycling of Copper at near-ambient temperature [13,58]. Early studies established the process's fundamental feasibility and highlighted its potential to reduce regeneration energy compared with the conventional method [13,26]. Following that, a system-level investigation expanded EMAR to continuous operation and quantified key metrics, such as Regeneration energy and Faradaic Efficiency, under different conditions [39,45].

Later research focused more on the process and on solvent improvement. Comparative studies of monoamine and polyamine solvents, including monoethanolamine (MEA) and ethylenediamine (EDA), showed that polyamines exhibit enhanced CO_2 capacity and regeneration behavior due to stronger coordination with Cu^{2+} ions [40,46,60]. Additional investigation focused on improving solvent stability and degradation pathways, aiming to extend EMAR operation at higher current densities and longer operating times [64,65].

Despite these advances, several challenges still limit EMAR performance. For example, elevated cell voltages and reduced faradaic efficiency are observed at high current density due to polarization losses, non-uniform copper redox activity, and mass transport limitations near the electrode surface [26,39]. In addition, lower charge transfer efficiency and non-uniform current

densities occur due to the degradation of the copper electrode and repeated cycles [46]. These limitations indicate that improving solvent performance alone will not solve these problems. Improved Electrode-level strategies are required to enhance interfacial charge transfer, stabilize copper redox behavior, and improve mass transport. Such issues motivate the exploration of advanced electrode architectures and surface modifications, including porous coatings and photo-assisted enhancements, as potential pathways to improve EMAR efficiency.

2.3 Aerogels for CO_2 Capture and Photocatalysis

Aerogels are a unique class of highly porous solids. They have ultra-low density, high specific surface area, and an interconnected three-dimensional pore structure. These features have led to the exploration of metal oxide aerogels, particularly for applications in gas-solid interactions, electrochemical processes, and photo-assisted energy conversion. In the context of carbon capture, aerogel enhances mass transport, increases the effective surface area, and improves the interfacial contact between the functional material and conductive substrates [41,66].

2.3.1 Sol–Gel Processing and Aerogel Fabrication

TiO_2 aerogel is most commonly synthesized via sol-gel processing. In this process, the titanium alkoxide precursor undergoes hydrolysis and condensation reactions to form a continuous inorganic structure. The sol-gel synthesis provides fine control over network formation, pore size distribution, and surface chemistry. These can be adjusted by controlling parameters such as precursor concentration, water-to-alkoxide ratio, solvent composition, and catalyst type [41]. Following gelation, aging, and solvent exchange steps, drying methods are employed to preserve the porous structure and prevent collapse.

Compatibility with substrate-supported fabrication is an important advantage of sol-gel processing. TiO_2 aerogels can be deposited onto conductive substrates via dip-coating or

infiltration. This forms a porous layer without the need for any polymeric binders. Phadtare et al. (2020) showed that sol-gel-derived TiO_2 aerogel can be used to coat solid supports while retaining its high porosity and mechanical integrity after drying and thermal treatment. These fabrication strategies enable the integration of aerogel networks with complex three-dimensional substrates for electrochemical applications [67,68].

2.3.2 TiO_2 Aerogels: Structure, Optical Properties, and Photocatalytic Behavior

TiO_2 aerogels combine the semiconductor properties of TiO_2 with a highly porous structure. This results in a material with a large internal surface area, abundant surface hydroxyl groups, and interconnected mesoporous structures. Proper calcination crystallizes the TiO_2 aerogels into the anatase phase, which exhibits enhanced photo-assisted performance [41]. The open network structure reduces the charge-carrier diffusion length. It also increases the accessibility of active sites compared to dense TiO_2 films or compact nanoparticle layers.

Under illumination, TiO_2 aerogels can generate additional charge carriers, improving interfacial charge transfer and electron transport to conductive materials. Zhang et al. (2017) reported that aerogel-modified metal electrodes exhibit improved charge-transfer characteristics and reduced interfacial resistance under photo-assisted conditions [69,70]. Such effects can enhance electrochemical kinetics and reduce polarization losses without underlying electrochemical reaction pathways.

2.3.3 Aerogel–Metal Foam Composite Electrodes

The integration of three-dimensional metal-foam substrates with TiO_2 aerogels is an effective strategy for constructing hierarchical composite electrodes. Metal foam substrates, such as copper foam, can serve as electrically conductive scaffolds, while a TiO_2 aerogel coating provides nanoscale porosity and significantly increases the effective surface area. Surface

functionalization strategies, such as silane-based coupling agents, are commonly used to promote adhesion between metal substrates and oxide aerogels. This improves coating stability during the electrochemical operation [67,71]. These resulting electrodes enhance electrolyte penetration and mass transport while maintaining their effective electrical pathways. Furthermore, in a photo-assisted system, it also improves the charge transfer at the electrode-electrolyte interface.

Within the context of EMAR, the TiO_2 aerogel-coated electrode offers a promising strategy at the electrode level to address limitations related to polarization losses, copper redox kinetics, and interfacial transport. By enhancing surface area, mass transport, and photo-assisted charge-transfer behavior, these composite electrodes offer a pathway to improve EMAR performance while preserving the fundamental electrochemical regeneration mechanism.

2.4 Photo-Assisted Enhancement in EMAR

The incorporation of illumination into the EMAR system provides an additional strategy to improve electrochemical performance without altering the regeneration chemistry. Unlike photoelectrochemical CO_2 conversion processes, in which light directly drives CO_2 transformation, illumination in EMAR enhances electrochemical kinetics, interfacial charge transfer, and electron utilization efficiency. Accordingly, illumination in this study is treated as a performance-enhancing input rather than a driving force for new reaction pathways.

The EMAR system relies on Cu^0/Cu^{2+} redox cycling to regenerate the solvent. Thus, any factors that reduce polarization losses or enhance charge transfer at the electrode-electrolyte interface can directly increase Faradaic Efficiency and lower the regeneration energy. Previous EMAR studies have shown that, rather than thermodynamic constraints, deviations from ideal performance come from kinetic and transport limitations. This highlights the importance of interfacial engineering for improved system efficiency [13,45,58]. In this context, photo-assisted

operation offers a potential means to enhance electrochemical behavior while preserving the intrinsic EMAR mechanism.

2.4.1 Charge Transfer and Light-Driven Enhancement

Illumination can indirectly affect the electrochemical system. It can enhance charge transfer and mass transport without requiring direct photocatalytic activation of the target reaction. Photo-assisted effects may include modification of local electric fields, reduction of interfacial charge-transfer resistance, improved carrier mobility within photoactive materials, and mild photothermal effects that enhance reaction kinetics [72–74].

In EMAR systems, improved charge transfer at the electrode surface directly benefits Cu^0/Cu^{2+} redox kinetics. It strengthens the coupling between electrical charge and CO_2 desorption. Incorporating illumination into the process thus improves Faradaic efficiency by reducing the current consumption by nonproductive processes. Importantly, this improvement does not alter the EMAR regeneration chemistry [13,26].

2.4.2 Synergistic Interactions Between TiO_2 Aerogels and Cu Foam

The combination of TiO_2 aerogel and copper foam electrodes provides a favorable platform for photo-assisted EMAR enhancement. The copper foam provides high electrical conductivity and a microporous structure. On the other hand, TiO_2 aerogel exhibits nanoscale porosity, a high surface area, and photoresponsive behavior. When integrated as a composite electrode, these materials form a hierarchical architecture that enhances both interfacial contact and mass transport.

Previous studies on aerogel-modified metal electrodes have demonstrated that such composite electrodes can reduce the charge transfer resistance and improve electrochemical stability under illumination [69,75,76]. The porous aerogel structure facilitates better electrolyte

penetration, while the TiO_2-Cu interface promotes efficient electron transfer under photo-assisted conditions.

In EMAR, this synergistic interaction is particularly relevant for stabilizing copper's redox behavior while mitigating polarization losses at higher current densities. Thus, these coated electrodes can improve the effectiveness of the EMAR system by enhancing the interfacial charge transfer, thereby reducing the energy required to recycle the absorbent.

2.5 Summary of Research Needs

Despite extensive development in amine-based CO_2 capture, conventional thermal regeneration still faces many challenges, such as high energy demand and solvent degradation. This motivates the adaptation of EMAR technology, due to its ability to use solvent regeneration by electrical means [11,77]. While EMAR demonstrated reduced regeneration energy, its performance is still limited by non-ideal Faradaic Efficiency, polarization losses, and incomplete utilization of applied electrical charge, particularly under higher current density [13,58].

Prior EMAR studies indicate that these efficiencies arise from interfacial charge transfer resistance and mass transport limitations at copper electrodes [39,45]. This suggests that further improvements in EMAR performance require targeted electrode and interface engineering to facilitate copper redox kinetics and solvent regeneration.

Recent advances in porous aerogel-based materials highlight the potential of electrode architectures to enhance electrode surface area, electrolyte accessibility, and transport properties. In particular, TiO_2 aerogels offer high porosity and photo-responsive behavior that may provide enhanced electrochemical performance without altering the EMAR chemistry [41,67]. However,

the use of TiO_2 aerogel–coated electrodes in EMAR systems, as well as the role of illumination in facilitating solvent regeneration, remains underexplored.

Therefore, there is a clear need to explore the impact of a TiO_2 aerogel-coated copper electrode in the EMAR system and to systematically quantify the regeneration energy and Faradaic efficiency under photo-assisted operation. Addressing these gaps is essential to advancing EMAR toward more energy-efficient, practically deployable CO_2 capture systems.

Chapter 3 Experimental Methodology

3.1 TiO_2 aerogel Synthesis

TiO_2 aerogel was synthesized via an acid-catalyzed sol–gel process followed by freeze-drying and thermal treatment. Titanium isopropoxide (TTIP) was used as the titanium precursor, ethanol as the solvent, deionized water as the hydrolysis agent, and nitric acid as the peptizing catalyst.

In a typical synthesis, 62.5 mL of ethanol was mixed with 2.5 mL of TTIP under continuous stirring to form solution A. Separately, 10 mL of deionized water was combined with 0.5 mL of nitric acid and 20 mL of ethanol to form solution B. Solution B was then added to solution A dropwise under continuous stirring until a transparent TiO_2 sol was obtained [78].

The sol was transferred to a container and allowed to gel and age under static conditions at 25 °C for 48 hours. Within 48 hours, the gel was immersed in tert-butanol, and the solvent was changed 4 times to remove residual water and ethanol.

The solvent-exchanged gel was frozen at -50 °C for 48 hours and then freeze-dried under vacuum for an additional 48 hours. The resulting TiO_2 aerogel powder was calcined in air at 450 °C for 4 hours with a ramp rate of 2 °C/min. After the calcination, the gel was allowed to cool naturally to room temperature [41,79].

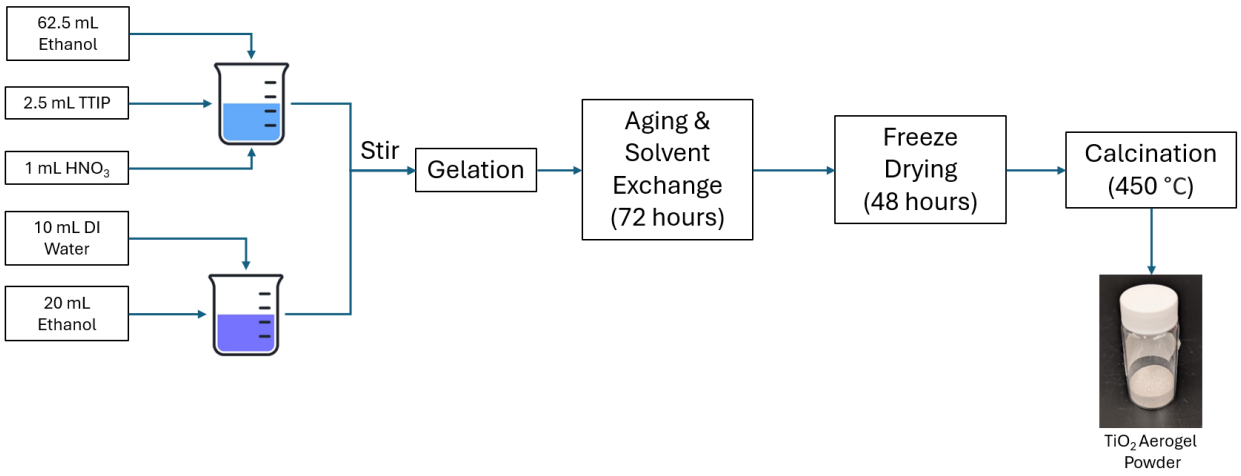

Figure 4: Schematic illustration of the preparation process of TiO_2 aerogel powder, including gelation, aging and solvent exchange, freeze drying, and calcination.[78,80]

3.2 Electrode Synthesis

Copper foam substrates were cut to the desired dimensions and cleaned prior to coating. The foam was immersed in 10 Vol% acetic acid to remove any surface oxides, rinsed thoroughly with DI water, and dried under ambient conditions.

Surface functionalization was carried out by immersing the copper foam in a 1% solution of (3-aminopropyl)triethoxysilane (APTES). The 1% APTES solution was prepared using ethanol. The cleaned copper foam was immersed in the solution and sonicated for 15 minutes to promote penetration into the porous structure. The foam was then kept in the solution for 1.5 hours undisturbed at room temperature. Following functionalization, the foam was rinsed with ethanol to remove any unbound silane species and then thermally cured at 110 °C for 1 hour to form a silane layer. The functionalized copper foams were prepared in advance prior to TiO_2 aerogel coating [81,82].

A TiO_2 aerogel suspension was prepared by mixing ethanol and DI water in a 9:1 volumetric ratio, followed by the addition of 75 mg of TiO_2 aerogel powder. The solution was sonicated for 30 minutes for uniform dispersion.

Dip coating was performed by immersing the APTES-functionalized copper foam in the TiO_2 aerogel suspension for 10 minutes, followed by 15 minutes of drying at room temperature. The foam was withdrawn from the suspension at a controlled rate of 2000 um/s to promote uniform coating. One, two, or three dip-coating cycles were applied depending on the desired coating thickness. The single coating cycle was used as the baseline condition unless otherwise specified. After coating, the electrodes were dried at 60 °C for 1 hour in a vacuum dryer until fully dry.

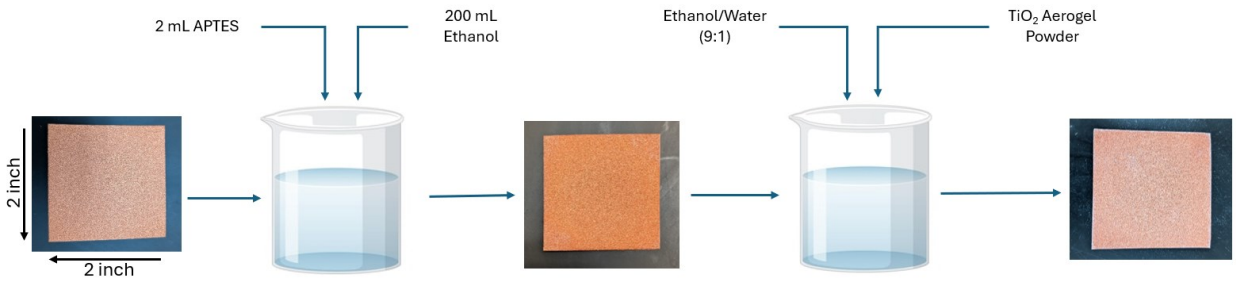

Figure 5: Schematic illustration of the coating process of copper foam with TiO_2 aerogel powder using APTES surface functionalization and dip-coating [67]

3.3 Electrochemical Cell and Materials

Two distinct experimental setups were used in this study. The laboratory-scale EMAR prototype was employed for the integrated absorption/desorption testing and overall process performance evaluation, including the CO_2 release behavior, regeneration energy, and Faradaic Efficiency. In this system, CO_2 absorption occurs via chemical absorption into the aqueous amine solution, followed by an electrochemically mediated desorption. Separately, a three-electrode system was also used for potentiostat-based measurements, including cyclic voltammetry and

electrochemical impedance spectroscopy (Section 3.4). This was done to isolate the intrinsic electrochemical behavior of the electrode materials.

The laboratory-scale continuous-flow electrochemical cell was used to investigate the EMAR system. The cell consisted of two compartments separated by a polymeric membrane (Cellgard, 3501). This membrane permits ionic transport while restricting mixing between the anodic and cathodic electrolytes. Each electrochemical compartment was integrated into a closed-loop liquid circulation system. The CO_2-rich amine solution was pumped from the absorber to the anodic compartment, and the two-phase mixture (CO_2 and amine-Cu complex) then went to the desorber, where CO_2 was separated. Subsequently, the amine-Cu complex is pumped to the cathodic compartment and then returned to the absorber.

Commercial copper foam electrodes were used in both compartments. The TiO_2 aerogel-coated electrode was used in the cathode compartment, while bare copper foam was used for the anode compartment. The copper foam had a thickness of 1 mm and a geometric area of 2 in × 2 in (25.8 cm^2). The interelectrode spacing was 1.18 inches.

The cell's external structure was constructed from stainless steel. Inside the cell, Delrin blocks were used to hold and align the electrochemical components, including the electrodes and membrane. EPDM gaskets were placed between the components to provide sealing and prevent electrolyte leakage. The electrolyte circulation between the absorber, electrochemical cell, and desorber was maintained using a peristaltic pump with Tygon tubing.

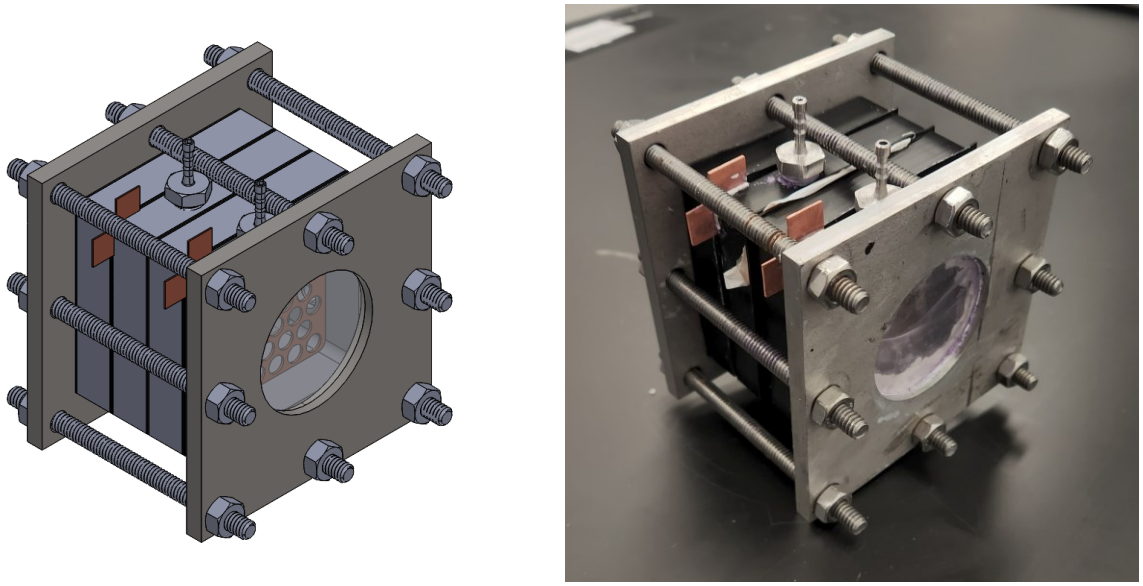

(a) (b)

Figure 6: (a) (a) Computer-aided design (CAD) model and (b) photograph of the laboratory-scale EMAR electrochemical cell

The EMAR electrolyte was a 1 M aqueous ethylenediamine (EDA) solution. Copper ions were introduced using copper (II) sulfate pentahydrate ($CuSO_4 \cdot 5H_2O$) at a concentration of 0.10 M to establish the Cu^{2+}/Cu^0 redox couple required for electrochemically mediated amine regeneration. Potassium nitrate (KNO_3) was used as a supporting electrolyte to increase the ionic conductivity of the solution [13,83]. Unless otherwise stated, these concentrations were maintained at baseline, while systematic variations were applied in selected experiments to evaluate parametric effects.

Illumination was provided using a solar simulator and was applied only to the coated electrodes. The incident light was directed towards the cathode-facing side of the electrochemical cell through a quartz window. Experiments conducted without illumination served as electrochemical references.

3.4 Electrochemical Analysis

Electrochemical analysis was performed using an Autolab potentiostat in potentiostatic mode. The three-electrode configuration was employed, consisting of the TiO_2 aerogel-coated copper foam as the working electrode, graphene as the counter electrode, and an Ag/AgCl reference electrode. All electrochemical measurements were conducted at room temperature under static conditions. The electrode used for electrochemical analysis was cut to dimensions 25 X 10 mm^2. The electrolyte solution consisted of 0.30 $mol \cdot L^{-1}$ ethylenediamine (EDA), 0.70 $mol \cdot L^{-1}$ KNO_3 as supporting electrolyte, and 0.05 $mol \cdot L^{-1}$ total dissolved copper (Cu^{2+}) [40,60].

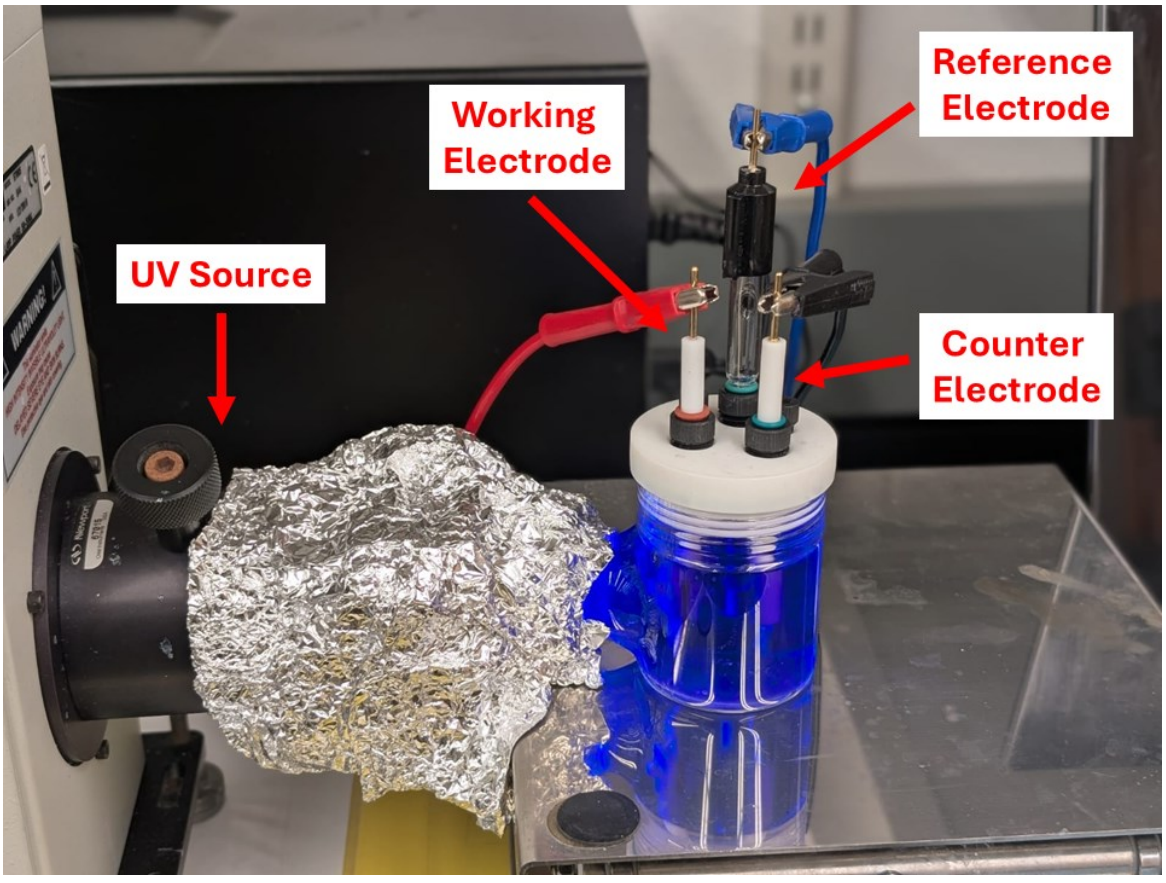

Figure 7: Experimental setup for electrochemical analysis of the TCF3 electrode under UV illumination using a three-electrode configuration.

3.4.1 Cyclic Voltammetry (CV)

Cyclic voltammetry (CV) tests were conducted to evaluate the redox behavior and the effect of coating on the electrodes. The CV tests were done using an Autolab potentiostat in a three-electrode configuration under static conditions at room temperature.

TiO_2 aerogel-coated copper electrodes were used as the working electrodes, graphite served as the counter electrode, and an Ag/AgCl electrode was employed as the reference electrode. The electrolyte consisted of 75mL of an aqueous 0.3M ethylenediamine (EDA), 0.1 Cu^{2+}, and 0.7M KNO_3.

All CV tests were conducted over a potential window from -0.8V to 0.5V versus Ag/AgCl. A constant scan rate of 0.07 V/s was applied for all measurements to ensure consistency across the experiments.

3.4.2 Electrochemical Impedance Spectroscopy (EIS)

Electrochemical impedance spectroscopy (EIS) measurements were performed using a similar three-electrode configuration. A sinusoidal AC perturbation with an amplitude of 0.01V was applied over a frequency range from 1×10^5 Hz to 1 Hz. The measurements were performed using the same electrolyte used for the CV tests.

EIS spectra were collected under both dark and illuminated conditions to evaluate the effect of UV radiation on interfacial charge-transfer processes. The obtained impedance data were analyzed using an equivalent circuit fit. The fitted parameters were used to assess changes in solution resistance and charge-transfer resistance associated with electrode modification and illumination.

3.5 CO_2 Absorption–Desorption Experiments and Data Analysis

The CO_2 absorption and desorption test was conducted in a laboratory-scale setup. It consisted of separate absorber and desorber units. Both the absorber and desorber were implemented using three-neck round-bottom flasks containing mechanical stirring to ensure homogenous gas-liquid contact.

Pure CO_2 was used as the feed gas for absorption experiments at a controlled flow rate of 100 SCCM. Prior to data collection, the system was purged with CO_2 and allowed to reach steady-state conditions. The solvent consisted of 1 M ethylenediamine (EDA), 0.05 M Cu^{2+}, and KNO_3 prepared in deionized water, with a total volume of 250mL.

To determine the CO_2 capture performance, inlet and outlet gas flow rates were monitored during absorption. The absorbed CO_2 flow was obtained from the difference between the inlet and outlet flow rates:

$$Q_{abs} = Q_{in} - Q_{out} \tag{8}$$

The CO_2 absorption rate was calculated by converting the volumetric flow difference to molar flow, assuming standard conditions:

$$r_{CO_2} = Q_{abs} / 22.414 \tag{9}$$

Measurements were conducted every 30s ($\Delta t = 0.5$ min), and the amount of CO_2 absorbed in each interval was calculated as:

$$n_i = r_{CO_2} \times \Delta t \tag{10}$$

The cumulative CO_2 uptake was obtained by summing over time:

$$n_{CO2,cum} = \Sigma (r_{CO_2} \times \Delta t) \tag{11}$$

The CO_2 loading was determined on an EDA basis as:

$$\alpha = n_{CO_2,cum} / n_{EDA} \quad (12)$$

where n_{EDA} = 0.25 mol for 250 mL of 1 M EDA.

The CO_2 capture efficiency was calculated at each time step as:

$$\eta_{CO_2} = (Q_{in} - Q_{out}) / Q_{in} \quad (13)$$

To ensure complete saturation, CO_2 was continuously bubbled through the solvent over an extended duration (overnight). The solvent composition remained constant for all experiments unless otherwise stated.

3.5.1 Experimental Setup and Data Processing

The CO_2 concentration was measured at the desorber outlet using a Gasmet DX4030 Fourier-transform infrared (FTIR) gas analyzer. Gas-phase CO_2 concentration data were continuously recorded and processed using Calcmet software (Version 2.1).

The total amount of CO_2 released during each experiment was calculated using the total outlet gas volume measured by the flow meter totalizer and the time-averaged CO_2 mole fraction measured by the FTIR analyzer. The total moles of CO_2 released were calculated using Equation (1):

$$\dot{n}CO2 = \frac{\overline{y_{CO_2}} \cdot Q_{total}}{V_m} \quad (14)$$

where n_{CO_2} is the total moles of CO_2 released, $\bar{y}_{CO_2}$ is the time-averaged CO_2 mole fraction measured by the FTIR analyzer, Q_{total} is the total outlet gas volume measured by the flow meter totalizer, and V_m is the molar volume of gas at the reference condition of the flow measurement.

The CO_2 desorption rate was calculated using the measured outlet CO_2 concentration and the known gas flow rate. Time-resolved concentration data were multiplied by the volumetric flow rate to determine the instantaneous CO_2 release rate, which was subsequently averaged over the operating period to obtain representative values.

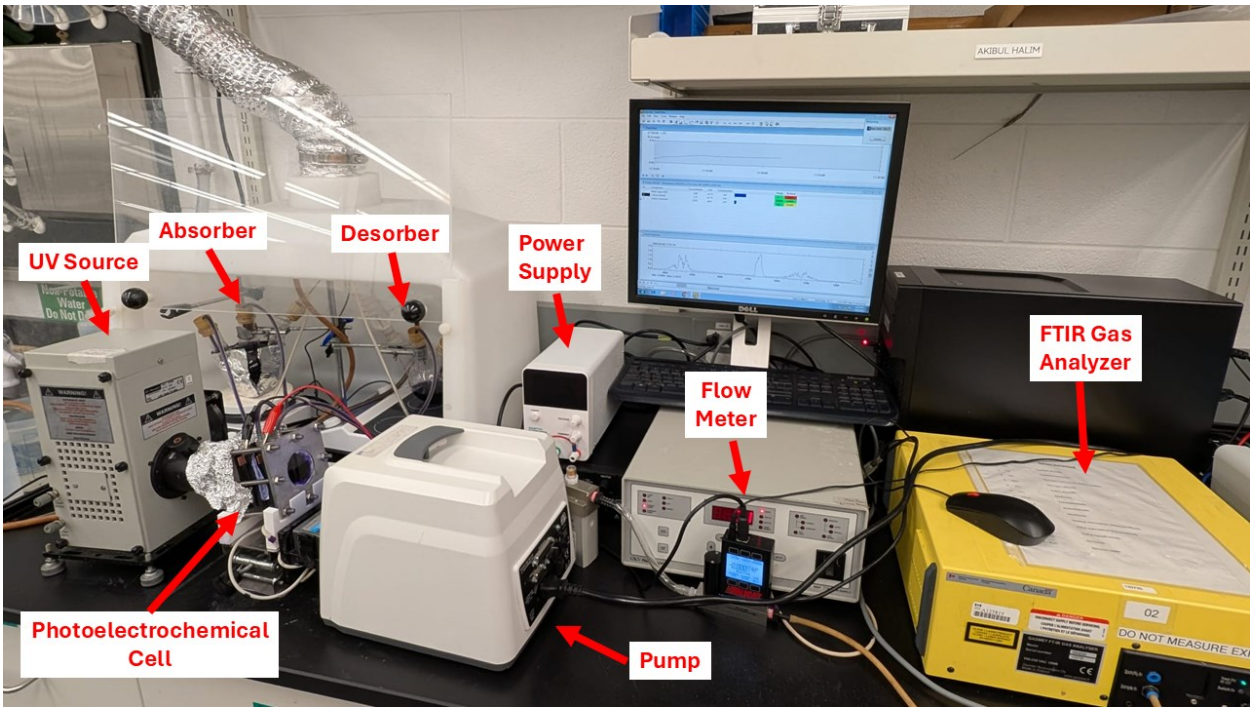

Figure 8: Bench-scale experimental setup of the EMAR system used for CO_2 absorption and electrochemical regeneration under UV illumination

3.5.2 Operating Conditions (T, rpm, Flow, Voltage)

The absorption temperature was maintained at 40 °C, while the desorber temperature was set without active temperature control. Mechanical stirring was used in both the absorber and desorber at a constant speed of 450 rpm to promote uniform mass transfer. The solvent circulation rate was maintained at 25 mL/min, unless otherwise mentioned.

Electrochemical regeneration was performed under constant-current conditions for each experiment. Each experimental run was conducted for 1 hour under steady-state operating conditions.

The Faradaic efficiency (FE) was calculated to evaluate how effectively the supplied electrical charge contributed to CO_2 release during the EMAR process. The FE was determined using Equation (9):

$$\text{FE} = \frac{n_{CO_2} Z\, F}{It}\, X\, 100 \tag{15}$$

where n_{CO_2} is the total moles of CO_2 released, z represents the number of electrons transferred per mole of CO_2 released. Although the Cu^{2+}/Cu redox couple involves a two-electron transfer ($Cu^{2+} + 2e^- \rightarrow Cu^0$), each Cu^{2+} ion typically coordinates with two amine functional groups, displacing one CO_2 molecule per Cu^{2+} formed. As a result, the effective electron requirement becomes 1 electron per mole of CO_2 released (z = 1), $F$is the Faraday constant (96485 C/mol), I is the applied current, and t is the electrolysis time.

The regeneration energy (RE) was calculated to quantify the electrical energy required to release one mole of CO_2 from the solvent, as shown in Equation (3):

$$\text{RE} = \frac{E_{cell}\, .I.t}{n_{CO_2}} \tag{16}$$

where $E_{cell}$is the average cell voltage during the experiment, I is the applied current, t is the electrolysis time, and $n_{CO_2}$is the total number of moles of CO_2 released. These performance metrics were used to quantitatively compare electrochemical regeneration efficiency and energy demand across different operating conditions and electrode configurations.

Chapter 4 Experimental Results

4.1 TiO_2 Aerogel Powder Characterization

4.1.1 Thermogravimetric Analysis (TGA)

Thermogravimetric Analysis (TGA) was performed to evaluate the thermal stability and decomposition behavior of the TiO_2 aerogel powder before and after calcination (Figure 9). For the non-calcined TiO_2 aerogel powder, a significant mass loss of approximately 23.62% was observed around 250 °C. This initial weight loss is due to the removal of physical adsorbed moisture, residual solvents, and volatile organic species remaining from the synthesis process. As the temperature increased beyond this region, a gradual decrease in mass was observed due to the removal of organic residues. As the temperature increased to 800 °C, a 5.46% mass loss was observed due to the removal of residual hydroxyl groups and further densification of the TiO_2 network. Beyond this temperature, the weight change becomes minimal as the material reaches a thermally stable oxide structure.

In contrast, the calcined TiO_2 aerogel powder shows excellent thermal stability across the entire temperature range. Only a minor 2% weight loss was observed up to 1000 °C. This is primarily attributed to the weakly bound surface species, such as adsorbed water or residual surface hydroxyl groups. This negligible change in weight confirms that the calcination process removed the volatile components and stabilized the TiO_2 framework.

Overall, the TGA results demonstrate that calcination significantly improves the thermal stability of the TiO_2 aerogel. The minimal mass loss observed for the calcined sample confirms the formation of a stable oxide structure that is suitable for many electrochemical applications.

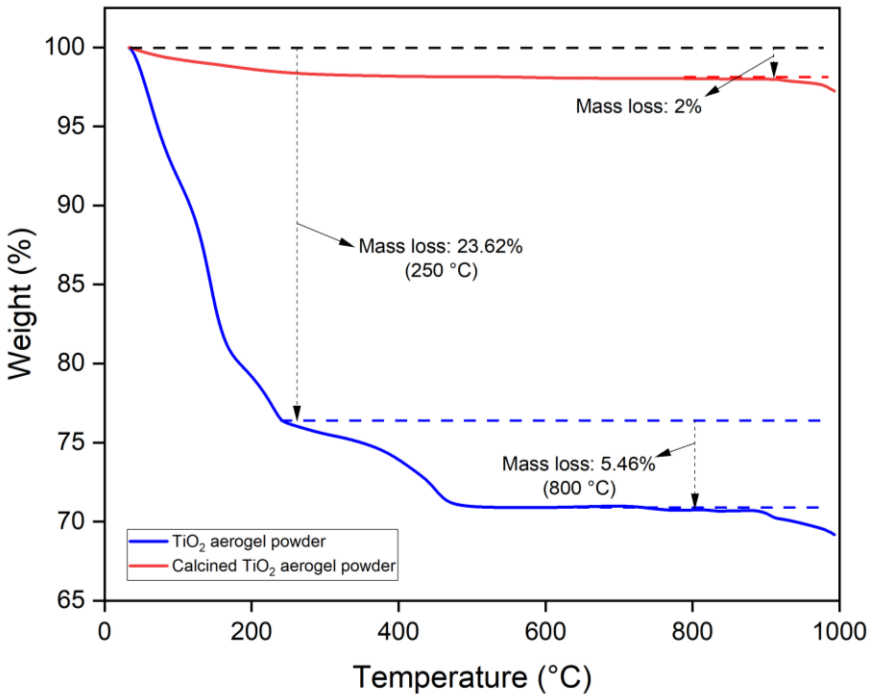

Figure 9: Thermogravimetric analysis (TGA) curves of TiO_2 aerogel powder before and after calcination. The uncalcined aerogel exhibits significant mass loss due to the removal of physically adsorbed moisture and decomposition of residual organic components, while the calcined sample shows minimal weight loss, indicating improved thermal stability after calcination.

4.1.2 Laser Diffraction Particle Size Analysis (LDPSA) and Pore Size Distribution

The particle size distribution of the TiO_2 aerogel was determined using laser diffraction particle size analysis (LDPSA), and the results are presented in Figure 10. The distribution exhibited a unimodal profile with the majority of particles falling within the 9–39 µm range. The median particle size (D50) was 19.4 µm, indicating that 50% of the sample volume consisted of particles smaller than this value. The mean particle size was slightly larger at 22.3 µm, reflecting the influence of a small fraction of coarser particles on the overall average. The most frequently occurring particle size (mode) was 18.7 µm, closely matching the median, suggesting a relatively symmetric distribution with limited skewness toward larger particle sizes.

The D10 and D90 values were 9.2 µm and 39.0 µm, respectively, confirming that 80% of the sample volume lay within this range. The moderate span (D90/D10 ≈ 4.2) indicates a controlled particle size distribution with limited coarse agglomeration. A high transmittance value of ~98% during measurement confirmed that the suspension was well-dispersed, supported by 40 seconds of ultrasonication prior to analysis.

Overall, the LDPSA results demonstrate that the synthesized TiO_2 aerogel consists of uniform particles with a characteristic size centered around ~20 µm. This particle size range is favorable for reproducible dispersion in the coating suspension and uniform deposition onto CF. The absence of excessive coarse agglomerates reduces the likelihood of pore blockage within the macroporous foam.

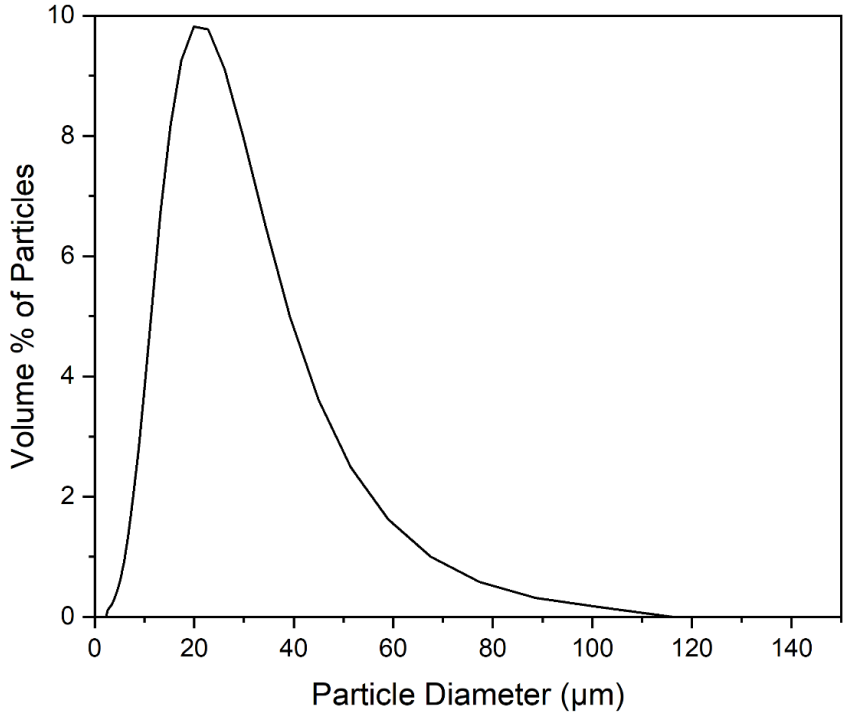

Figure 10: Laser diffraction particle size distribution of calcined TiO_2 aerogel powder showing the volume-based particle size distribution as a function of particle diameter.

4.1.3 SEM Analysis of TiO_2 aerogel powder

Scanning electron microscopy (SEM) was performed to compare the morphology of the calcine TiO_2 powder (Figure 11). The objective was to evaluate structural features that influence the charge transfer and mass transport during the Cu redox cycling in EMAR.

The calcined TiO_2 aerogel powder (Figure 11a-b) exhibits a porous and loosely interconnected structure. The particles are composed of irregularly shaped aggregates. No dense sintering regions were observed. This indicates that calcination preserved the aerogel framework while stabilizing the oxide phase. A rough and heterogeneous surface was observed at higher magnification. Such morphology provides increased surface roughness and accessible interfacial area when deposited onto a conductive substrate.

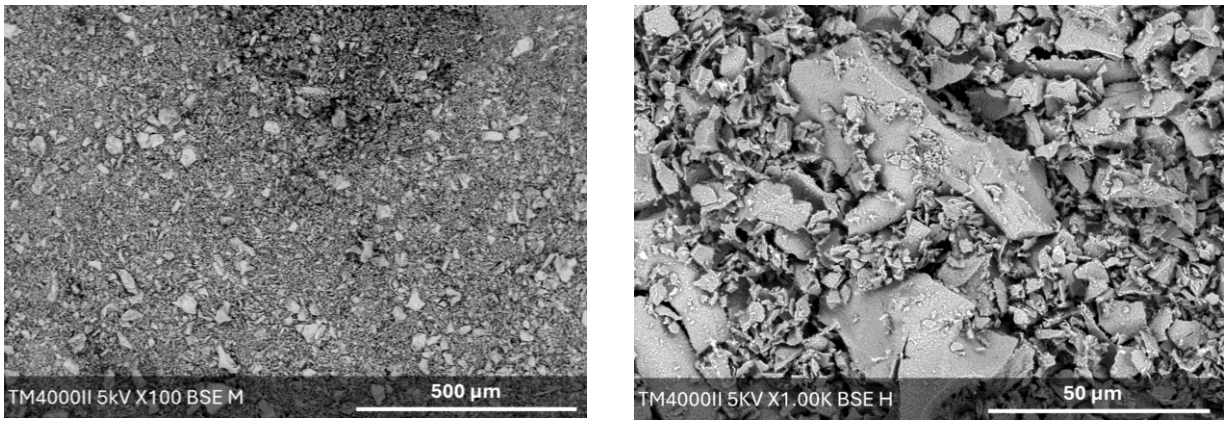

(a) (b)

Figure 11: SEM images of calcined TiO_2 aerogel powder at different magnifications showing (a) overall particle distribution and morphology (500 µm scale bar) and (b) fractured and irregular particle structures of the aerogel powder (50 µm scale bar).

4.1.4 BET Surface Area Analysis of TiO_2 Aerogel Powder

Nitrogen adsorption-desorption isotherm measurements were performed to evaluate the surface area and pore characteristics of the calcined TiO_2 aerogel powder. The calcined aerogel's mesoporous structure was confirmed from its type IV isotherm with a pronounced hysteresis loop.

The BET surface area was determined to be 81.79 m^2g^{-1} with a total volume of 0.1165 cm^3g^{-1}. Density functional theory (DFT) analysis revealed a dominant pore diameter of approximately 12 nm. These results confirm that calcination preserved a stable mesoporous network.

The relatively high surface area and well-defined mesoporous structure of the calcined aerogel indicate that the material can provide abundant interfacial contact when integrated with conductive substrates. Such structural characteristics are beneficial for increasing surface roughness and enhancing electrode–electrolyte interaction when the aerogel is deposited onto copper foam electrodes.

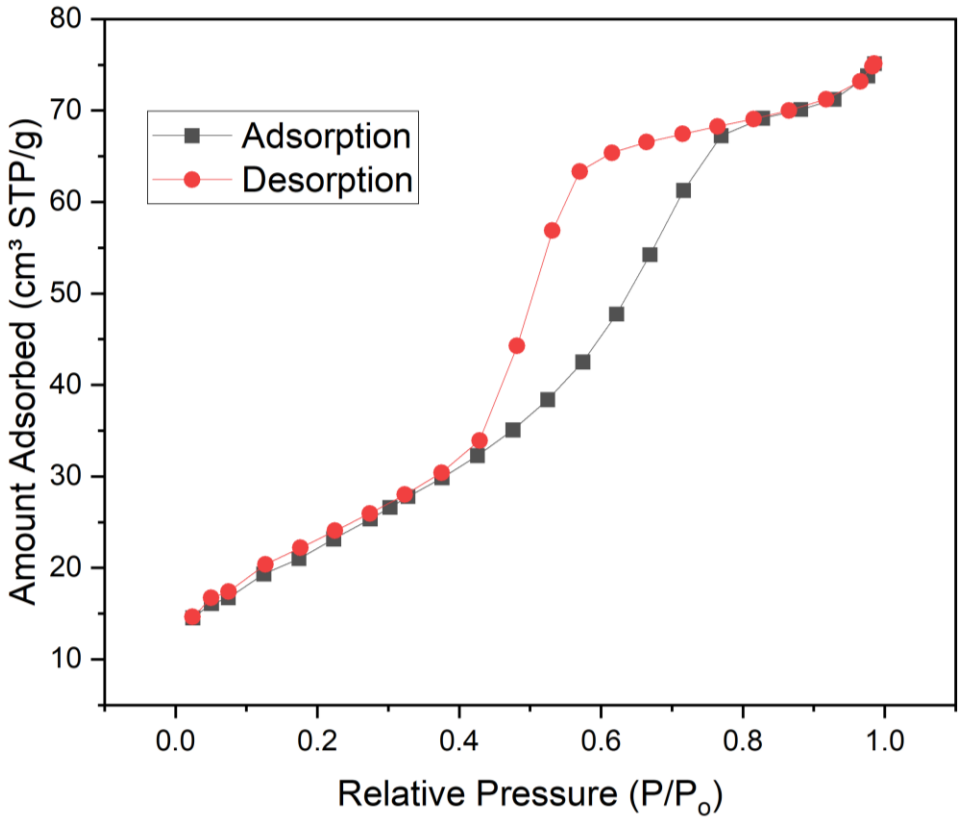

Figure 12: Nitrogen adsorption–desorption isotherm of calcined TiO_2 aerogel powder obtained from a single adsorption–desorption cycle showing the relationship between the amount adsorbed and the relative pressure (P/P_0).

4.1.5 TEM Analysis of TiO_2 Aerogel Powder

Transmission electron microscopy (TEM) was employed to examine the morphology, porosity, and crystallinity of the TiO_2 aerogel powder. Low-magnification TEM images revealed that the material forms large, loosely aggregated clusters composed of smaller primary nanoparticles. The aggregates show diffuse, cloud-like contrast rather than dense, compact regions. This indicates a highly porous internal framework consistent with aerogel-derived structures.

At higher magnification, the aerogel exhibited a sponge-like architecture consisting of fused nanoparticles with irregular and finely textured edges. Interparticle voids are clearly visible, which confirms the presence of interconnected mesoporosity within the aggregate structure. Partial necking between the adjacent nanoparticles gives rise to the porous network during the calcination. This nanoscale connectivity was consistent with the mesoporous structure which was identified from BET analysis.

High-resolution TEM (HRTEM) provided direct evidence of crystallinity. Distinct lattice fringes with an interplanar spacing of ~0.35 nm were observed, corresponding to the (101) planes of anatase TiO_2. The presence of multiple fringe orientations confirms that the aerogel consists of polycrystalline anatase domains rather than amorphous material. The primary crystallite size was estimated to be ~10–20 nm, which agrees with the nanoparticle dimensions observed in the micrographs and supports the mesoporous framework identified by nitrogen adsorption analysis.

Overall, the TEM results demonstrate that the TiO_2 aerogel is composed of anatase nanocrystals (~15 nm) arranged into a porous, interconnected network. This hierarchical morphology, nanoparticles forming micron-scale aggregates with interparticle mesoporosity, which yields a large accessible surface area and high crystallinity. These structural features are

well known to enhance the performance of TiO_2 aerogels in photocatalytic and CO_2 capture applications.

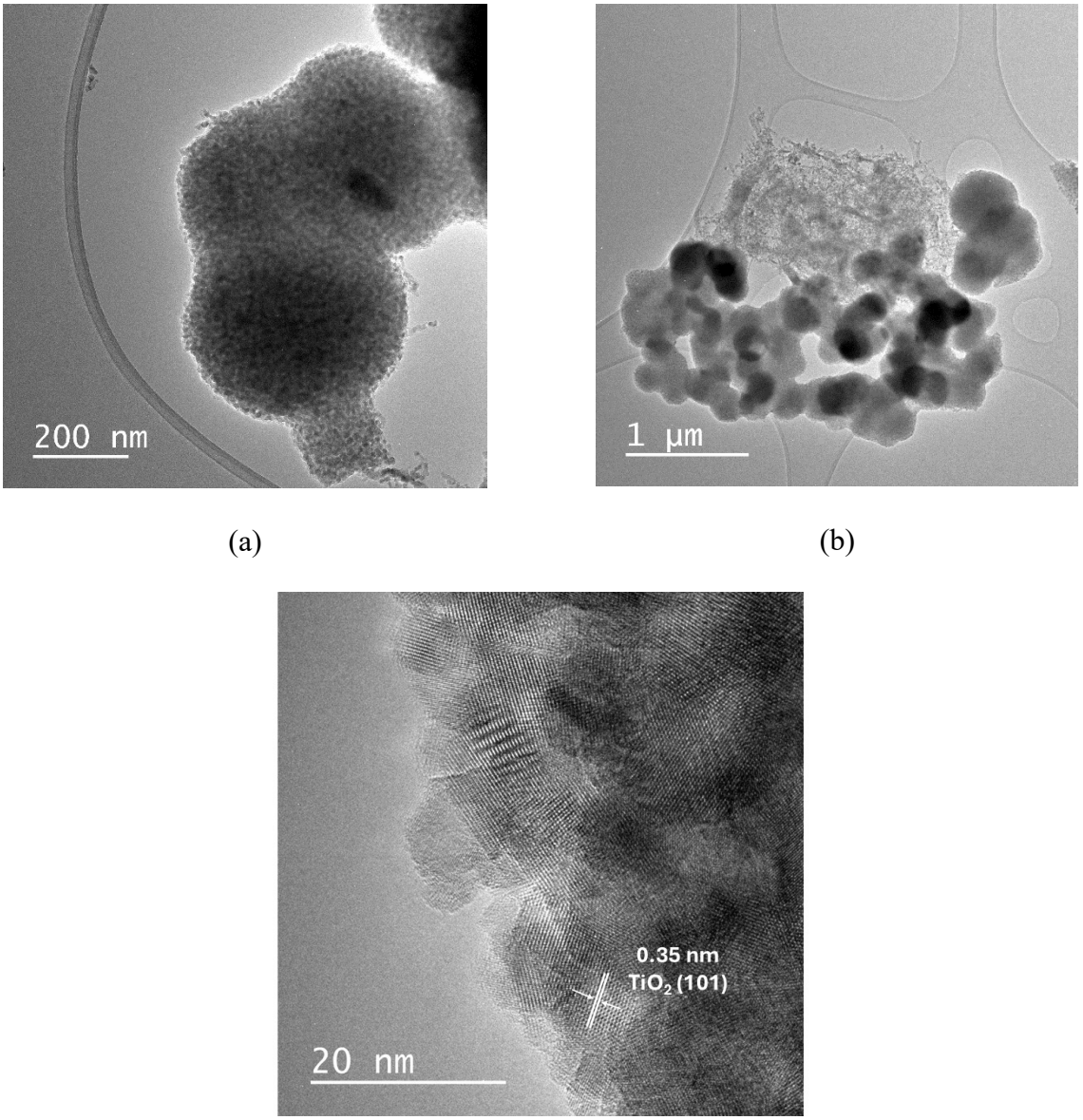

(a) (b)

(c)

Figure 13: TEM images of calcined TiO_2 aerogel at different magnifications showing (a) porous nanoparticle aggregate (200 nm scale), (b) micron-scale loosely aggregated clusters (1 µm scale), and (c) a high-resolution image displaying lattice fringes corresponding to the anatase TiO_2 crystal structure, confirming the nanocrystalline nature of the aerogel

4.1.6 XRD Structural Analysis of TiO_2 Aerogel Powder

The crystalline phase of the TiO_2 aerogel powder was confirmed from the X-ray diffraction (XRD) analysis. The diffraction pattern is shown in Figure 14. At approximately 25.3° (2θ), a dominant plane (101) was observed together with other planes (004), (200), (211), (204), (220), (215). These planes match well with the standard diffraction pattern of anatase TiO_2 [84], confirming successful phase transformation during calcination.

No diffraction peak was observed corresponding to the rutile or brookite phase. The sharpness and intensity of the anatase phase suggest good crystallinity following calcination at 450 °C. The strong (101) reflection and the characteristics of anatase confirm that the thermal treatment was sufficient to induce crystallization while preserving the porous structure, as confirmed by BET and TEM analysis.

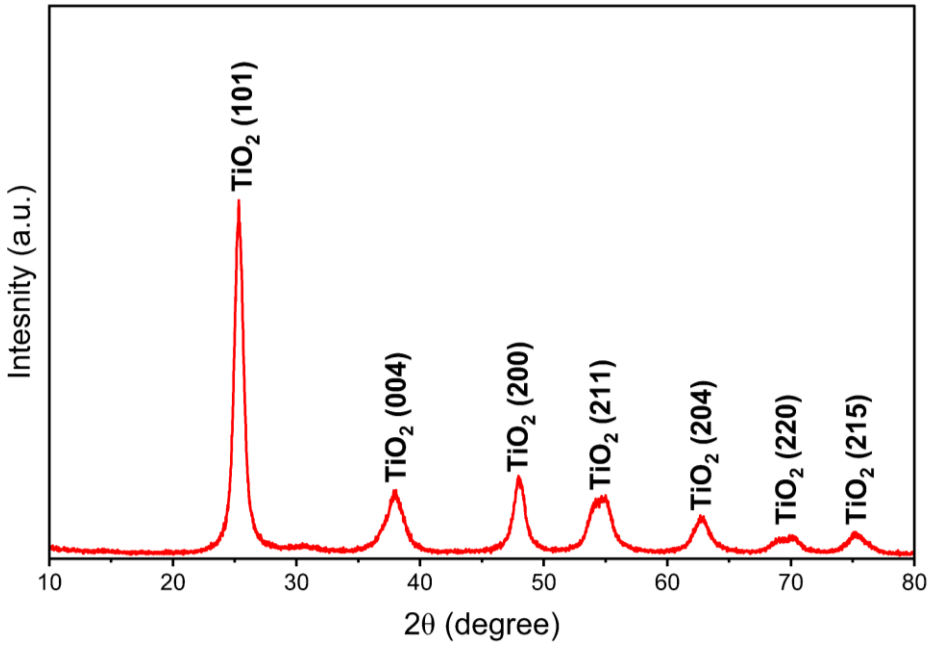

Figure 14: X-ray diffraction (XRD) pattern of the calcined TiO_2 aerogel powder showing characteristic diffraction peaks corresponding to the anatase phase of TiO_2. The dominant peak at approximately $2\theta \approx 25°$ corresponds to the (101) plane, confirming the crystalline anatase structure of the synthesized aerogel.

4.1.7 Raman Spectroscopy Analysis of TiO_2 Aerogel Powder

Raman spectroscopy was further employed to confirm the crystalline phase and structure of the calcined aerogel powder (Figure 15). Raman analysis is a sensitive technique for identifying TiO_2 polymorphs due to the distinct vibrational fingerprints associated with different crystal structures.

The Raman spectrum of the calcined TiO_2 aerogel powder showed clear peaks at approximately 168, 395, 515, 635 cm^{-1}. This corresponds to the vibrational mode characteristics of anatase TiO_2. The strong peak near 635 cm^{-1} is assigned to the Eg mode while the bands at 395 and 515 cm^{-1} correspond to the B1g and A1g/B1g modes, respectively. These vibrational modes represent the typical Raman fingerprint of anatase TiO_2 and confirm that the aerogel retained the anatase phase after calcination [84].

The presence of well-defined high-intensity peaks indicates that, after calcination, the oxide framework was successfully stabilized while preserving the aerogel structure. In addition, the absence of additional rutile and brookite phases suggests that the material consists predominantly of the anatase polymorph.

The slightly shifted low-frequency peak observed around 168 cm^{-1} may be associated with lattice strain or structural disorder within the aerogel framework. Such minor shifts are common in nanostructured or porous TiO_2 materials where the surface effects and nanoscale domains can influence vibrational behavior [84].

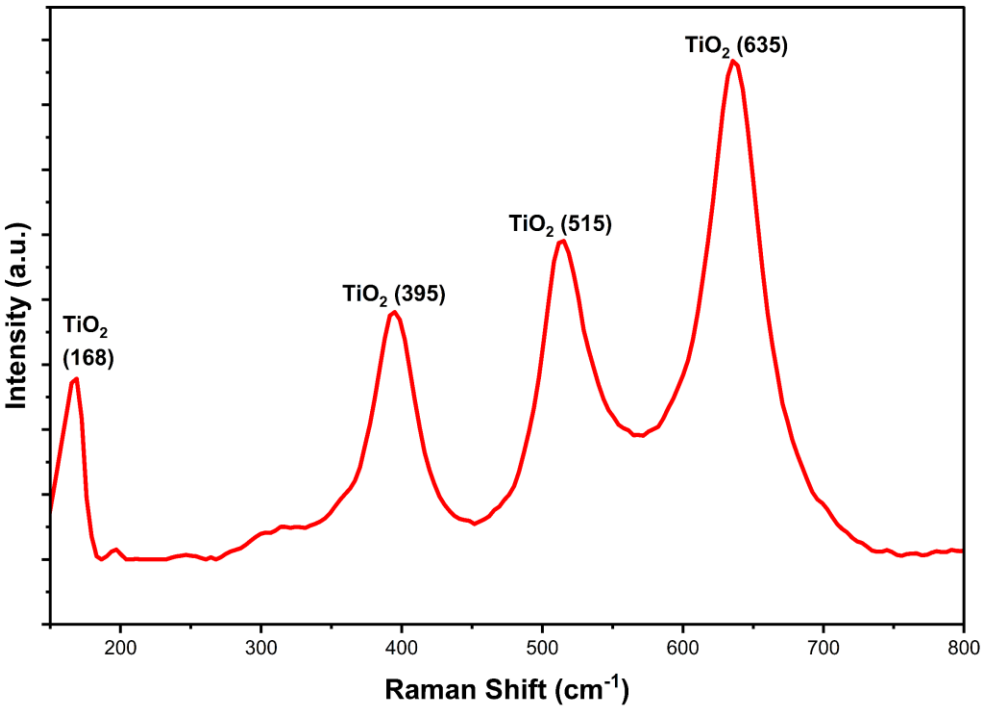

Figure 15: Raman spectrum of the calcined TiO_2 aerogel showing characteristic vibrational modes associated with anatase TiO_2. The observed peaks correspond to the Eg, B1g, and A1g Raman-active modes, confirming the presence of the anatase phase.

4.1.8 X-ray Photoelectron Spectroscopy (XPS) Analysis of TiO_2 Aerogel Powder

X-ray photoelectron spectroscopy (XPS) was performed to analyze the surface chemical composition of the calcined TiO_2 aerogel powder (Figure 16). XPS is a surface-sensitive technique that provides information regarding the elemental composition and chemical bonding states.

The survey spectrum of the TiO_2 aerogel powder confirms the presence of Ti and O as the dominant elements on the material surface. Trace N 1S and C 1S signals were also observed, which is commonly attributed to contamination during sample handling.

High-resolution analysis of the Ti 2P region (Figure 16b) shows two distinct peaks at 457.79 eV and 463.54 eV, corresponding to Ti $2p_{3/2}$ and Ti $2p_{1/2}$, respectively. The measured spin-orbit splitting is 5.75 eV, which is a characteristic of Ti^{4+} in TiO_2.

The absence of any lower binding energy indicates that the titanium remains in a fully oxidized state, confirming the formation of stoichiometric TiO_2 within the aerogel framework.

The O 1S spectrum (Figure 16c) shows a dominant peak around 529eV, corresponding to lattice oxygen (Ti-O-Ti) in TiO_2. Overall, the XPS results confirm that the calcined aerogel powder consists primarily of Ti^{4+} species bonded to lattice oxygen, consistent with the anatase TiO_2 phase identified by XRD and Raman spectroscopy.

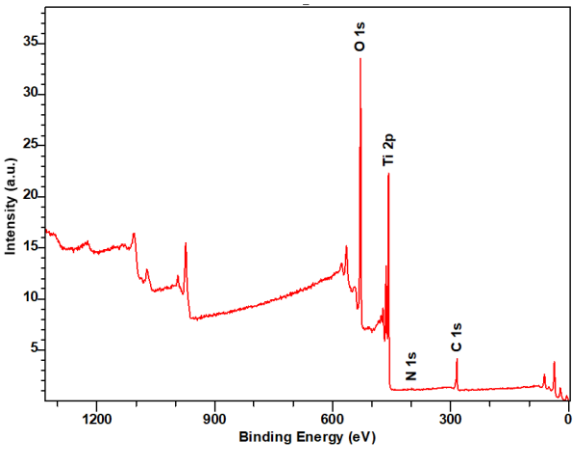

(a)

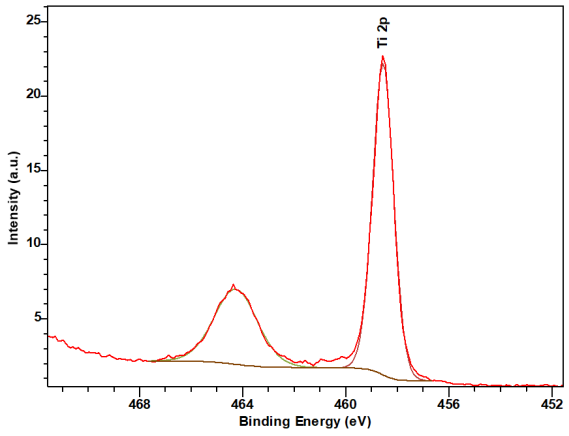

(b)

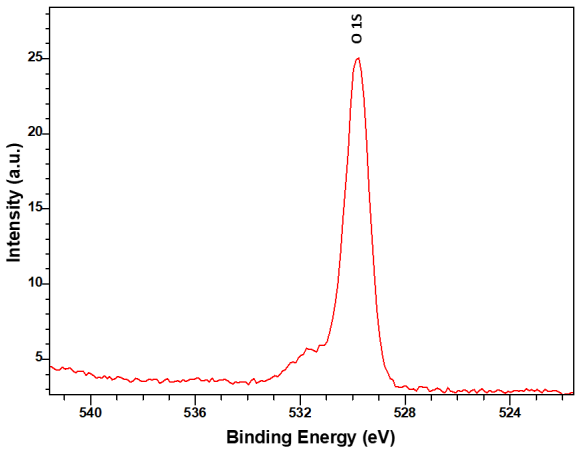

(c)

Figure 16: X-ray photoelectron spectroscopy (XPS) analysis of calcined TiO_2 aerogel powder showing (a) survey spectrum confirming the presence of Ti and O elements, (b) high-resolution Ti 2p spectrum indicating the Ti^{4+} oxidation state characteristic of TiO_2, and (c) high-resolution O 1s spectrum corresponding to lattice oxygen in the TiO_2 structure.

4.2 TCF Characterization

4.2.1 SEM Analysis of CF and TCF3

Scanning electron microscopy (SEM) was further used to examine the morphology of the bare copper foam and the TiO_2 aerogel-coated copper foam electrode (TCF3) (Figure 17). The objective was to evaluate structural features that influence the charge transfer and mass transport during the Cu redox cycling in EMAR.

The bare copper foam (Figure 17a-b) displays a three-dimensional open-cell architecture with interconnected macropores and smooth metallic ligaments. This macroporous structure supports bulk electrolyte transport, which is essential for the EMAR chemistry. The relatively smooth ligament surface provides limited microscopic electrochemically active surface area (ECSA), which increases the effective local current density at a fixed applied current.

In contrast, the TCF3 electrode (Figure 17c-d) shows successful deposition of the TiO_2 aerogel onto the copper ligaments while preserving the overall macroporous structure. No significant pore blockage was observed. This indicates bulk transport pathways remain accessible. At higher magnification, the coating appears conformal and textured, indicating an increased surface roughness relative to the bare foam without forming a dense barrier layer.

This structural modification increases the effective interfacial area while maintaining macroscopic mass transport. The local current density is expected to decrease due to this enhanced surface roughness. Meanwhile, the preserved macropores maintain effective Cu^{2+} transport and reduce concentration polarization. Overall, TCF3 morphology provides a balanced architecture that supports improved interfacial charge transfer without compromising electrolyte accessibility.

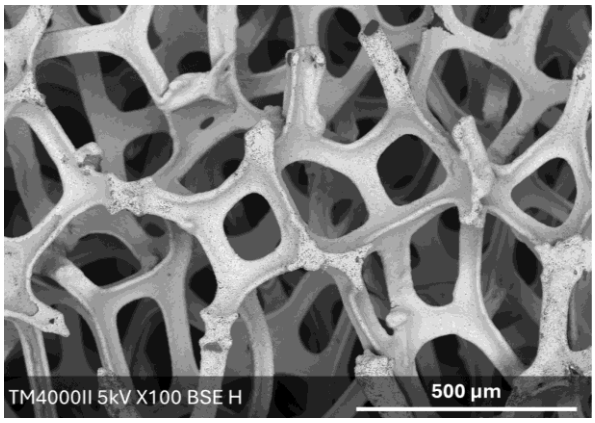

(a)

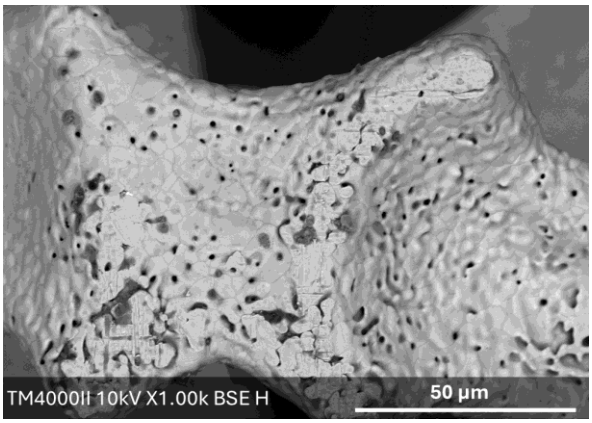

(b)

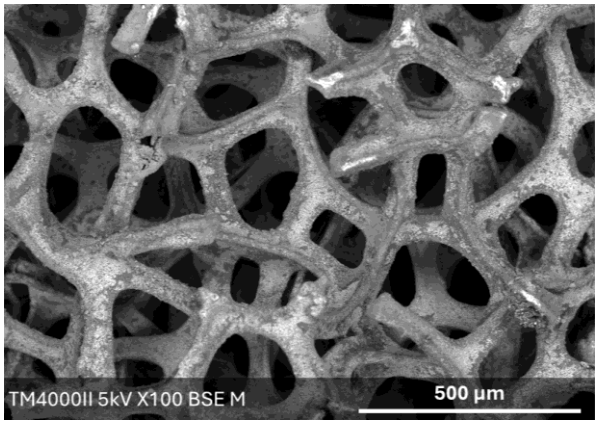

(c)

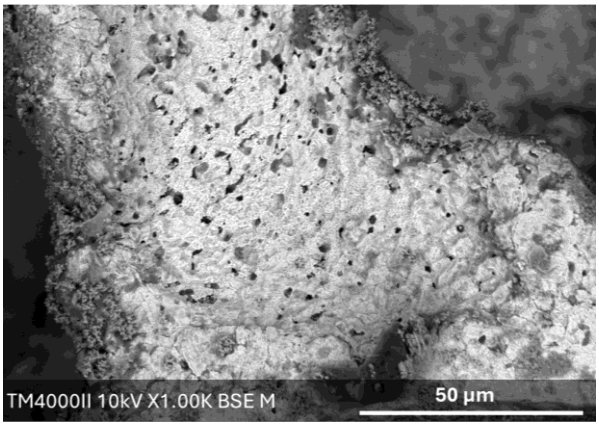

(d)

Figure 17: SEM images of (a) bare copper foam showing the original porous structure (500 µm scale bar), (b) magnified view of the bare copper foam surface (50 µm scale bar), (c) TiO_2 aerogel–coated copper foam (TCF5) showing the preserved foam morphology after coating (500 µm scale bar), and (d) magnified view of the coated surface illustrating the aerogel particle deposition on the copper struts (50 µm scale bar).

4.2.2 Micro-CT (µCT) Structural Analysis

Micro-computed tomography (µCT) was performed to analyze the macroporous structure of the bare copper foam and TiO_2 aerogel-coated copper foam. This is a non-destructive analysis that visualizes the pore connectivity, ligament structure, and bulk porosity. It provides insight into whether TiO_2 deposition alters the macroscopic transport framework of the electrode.

The μCT images (Figure 18) reveal that the open cell structure of the CF is preserved even after coating. No visible pore obstruction or structural collapse is observed. Quantitative analysis was performed using ImageJ on the reconstructed μCT images to determine the porosity, mean pore size, and pores per inch (PPI). The porosity (ε) was calculated as

$$\varepsilon = \frac{V_{Void}}{V_{Total}} X\ 100 \tag{17}$$

Where V_{Void} represents the void volume, and V_{Total} represents the total analyzed volume. The average pore diameter (d_{avg}) was obtained from

$$d_{avg} = \frac{1}{n} \sum_{i=1}^{n} d_i \tag{18}$$

Where d_i is the diameter of individual pores. The PPI value was determined from

$$PPI = \frac{N_p}{L} \tag{19}$$

Where N_p is the number of pores intersecting a measurement line of length L. Using this approach, the porosity was observed to vary slightly from 83% (CF) to 86% (TCF3). The mean pore size remained unchanged (0.59mm). The pores per inch (PPI) value also showed negligible variation (43 for uncoated and 42 for coated). These results confirmed that TiO_2 deposition does not significantly modify the foam's macroscopic structure.

The absence of a measurable reduction in pore size or PPI indicates that the coating forms a thin layer rather than a thick blocking film. To minimize hydraulic pressure within the cell and maintain convective electrolyte transport, preserving macroporosity is critical. Because electrolyte transport primarily occurs through macroscopic channels. Structural integrity at this scale ensures that mass transport limitations are not introduced by the coating process.

The slight variation in apparent porosity may be attributed to surface roughening, which was also evident from SEM and BET analyses. This suggests that TiO_2 coating on CF primarily alters the surface structure at the electrode interface without compromising the bulk transport pathways provided by the foam. Overall, µCT analysis confirms that the TiO_2 coating enhances surface structuring without compromising the macroporous framework required for efficient electrolyte circulation.

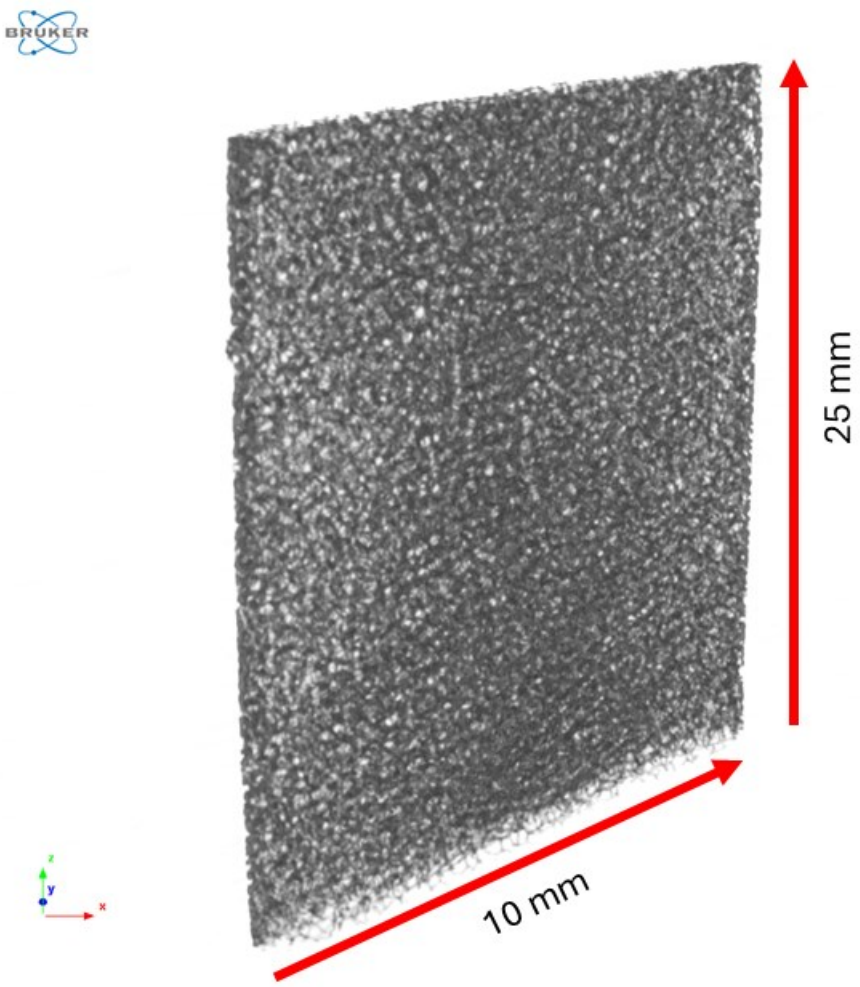

Figure 18: µCT image of the TiO_2 aerogel–coated copper foam electrode (TCF3) showing the three-dimensional porous architecture of the foam structure.

4.2.3 Raman Spectroscopy Analysis of TCF3 Electrodes

Raman spectroscopy was further used to examine the structural characteristics of the TiO_2 aerogel coating deposited on the copper foam electrode (TCF3) (Figure 19). The Raman spectrum of TCF3 shows clear peaks around 237, 430, 515, and 614 cm^{-1}.

Compared to the TiO_2 aerogel powder, the peaks in the TCF3 shifted slightly and broadened. However, the characteristics of the anatase fingerprint remain clearly identifiable. The presence of these peaks confirms that the anatase structure of TiO_2 is preserved after depositing onto the copper foam. This observation indicates that the dip-coating process used to fabricate the TCF electrode does not significantly alter the crystalline structure of the TiO_2 aerogel. The minor shifts in the peaks may arise from interaction with the copper substrate, local strain effects, or differences in measurement location on the coated foam.

In addition, the slightly broader peak shapes observed in the TCF3 spectrum may be attributed to the heterogeneous nature of the coated surface and the complex morphology of the copper foam structure. Despite these variations, the clear presence of anatase Raman modes confirms that the functional TiO_2 phase remains intact after integration with the conductive substrate.

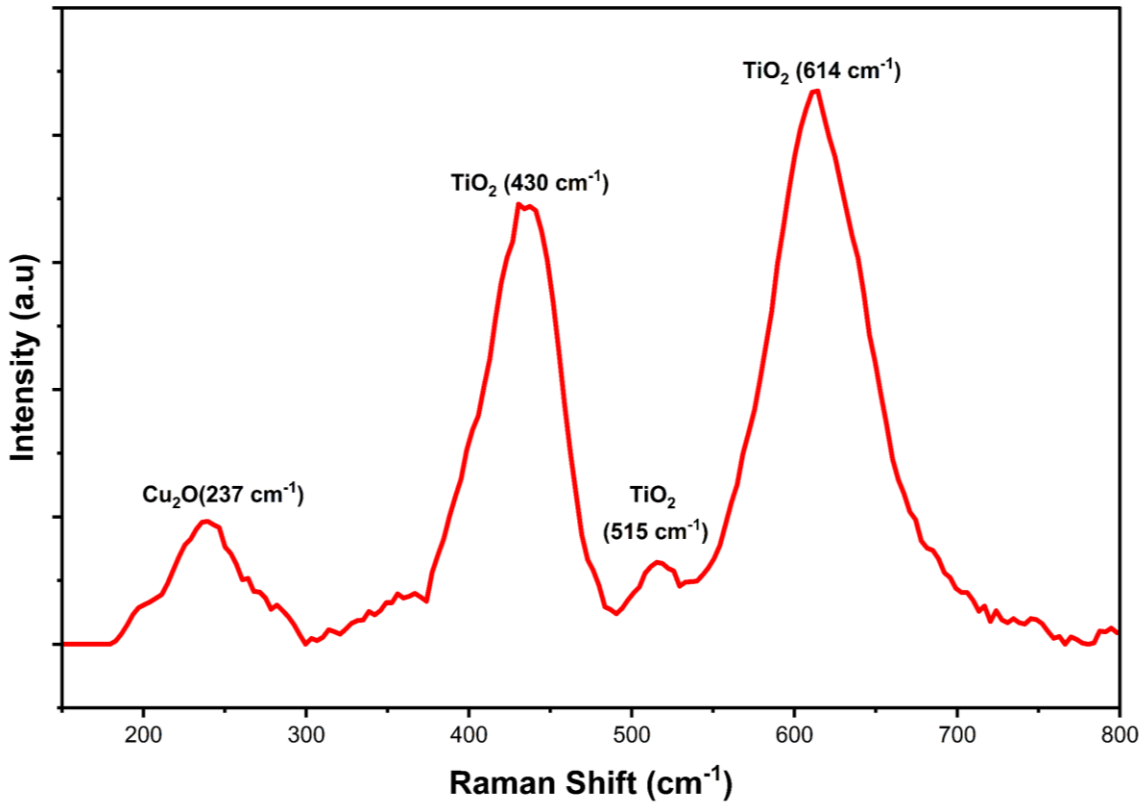

Figure 19: Raman spectrum of the TiO_2 aerogel–coated copper foam electrode (TCF3) showing characteristic Raman peaks associated with anatase TiO_2.

4.2.4 X-ray Photoelectron Spectroscopy (XPS) of TCF3

X-ray photoelectron spectroscopy (XPS) was performed to analyze the surface chemical composition of TCF3 (Figure 20). The survey spectrum (Figure 20 a) confirms the presence of Ti, O, Cu, C, N, and a minor Si signal. The detection of Cu 2P peaks indicates the copper substrate beneath the coating. The Ti 2P and O 1S signal is due to the successful deposition of TiO_2 aerogel powder onto the foam substrate. The Si 2P peak originates from the silane layer (APTES), which was used for surface functionalization prior to aerogel deposition.

High-resolution analysis of the Ti 2p region (Figure 20b) shows two distinct peaks corresponding to Ti $2p_{3/2}$ and Ti $2p_{1/2}$, indicating that titanium remains in the Ti^{4+} oxidation state

characteristic of TiO_2. No additional peaks associated with reduced Ti species were observed, confirming that the TiO_2 coating maintains its oxidized chemical state after the coating process.

The O 1S spectrum (figure 20c) shows a dominant peak around 529eV, corresponding to lattice oxygen associated with Ti–O–Ti bonds within the TiO_2 structure. This confirms the presence of oxide lattice in the aerogel coating.

The Cu 2p spectrum (Figure 20d) clearly confirms the presence of the copper substrate beneath the coating layer. The observed binding energies are consistent with metallic copper, indicating that the coating process does not significantly alter the oxidation state of the copper foam.

The Si 2p spectrum (Figure 20e) shows a peak centered near ~103–104 eV, which is characteristic of oxidized silicon in siloxane bonds (Si–O–Si or Si–O–metal). This peak confirms the presence of the APTES silane functionalization layer used to anchor the TiO_2 aerogel particles onto the copper foam surface. The presence of Si and N signals together with the Ti and Cu peaks suggests that the TiO_2 aerogel coating is attached to the copper substrate through a silane-mediated interfacial bonding layer.

Overall, the XPS results confirm that TCF3 consists of a TiO_2 coating dominated by Ti^{4+} species bonded to lattice oxygen, supported on a copper foam substrate and anchored through the APTES silane functionalization layer.

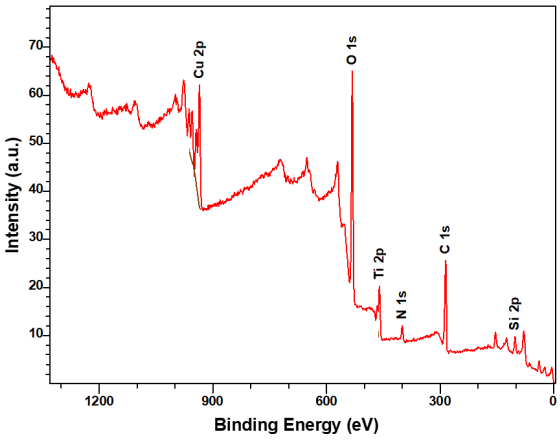

(a)

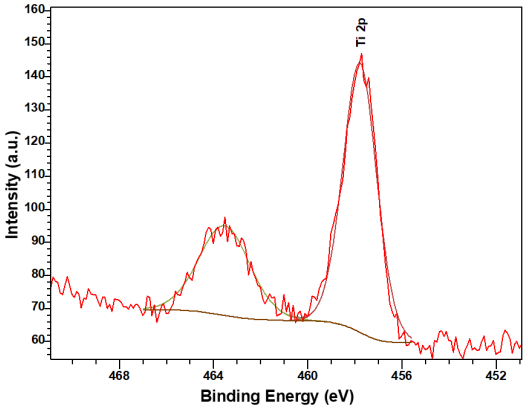

(b)

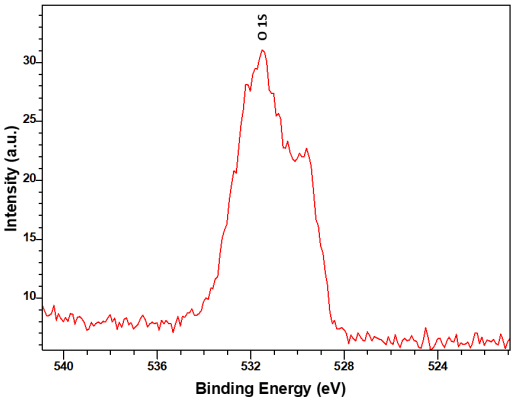

(c)

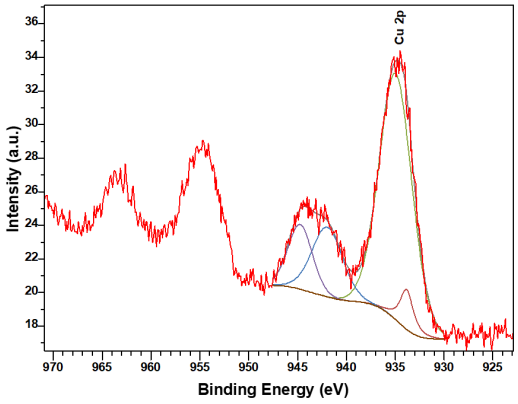

(d)

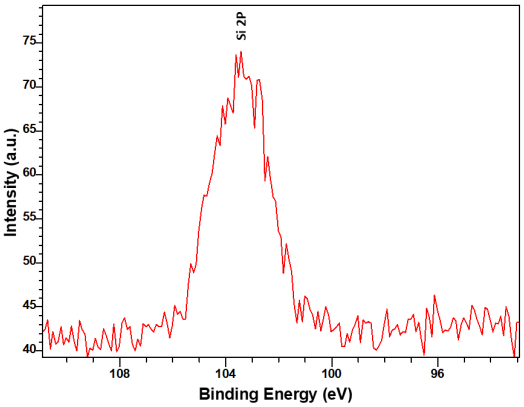

(e)

Figure 20:X-ray photoelectron spectroscopy (XPS) analysis of TiO_2 aerogel coated copper foam (TCF3) showing (a) survey spectrum confirming the presence of Ti, O, Cu, C, N, and Si elements, (b) high-resolution Ti 2p spectrum indicating Ti^{4+} species characteristic of TiO_2, (c) O 1s spectrum corresponding to lattice oxygen in the TiO_2 structure, (d) Cu 2p spectrum confirming the presence of the copper substrate beneath the coating, and (e) Si 2p spectrum indicating siloxane bonding associated with the APTES functionalization layer used to anchor the TiO_2 aerogel coating.

4.3 Electrochemical Characterization

Electrochemical characterization was conducted to evaluate the influence of the electrode structure and TiO_2 aerogel coating on the electrochemical behavior related to EMAR operation. Cyclic voltammetry (CV) was used to investigate the redox behavior and reversibility of the Cu^{2+}/Cu^0 system on different electrodes. Similarly, electrochemical impedance spectroscopy (EIS) was employed to analyze the interfacial charge transfer resistance and electrode conductivity. In addition, potential-time measurement under intermittent UV illumination was performed to evaluate the photoelectrochemical response of the TCF3, which provides insights on how UV irradiation influences the charge transfer processes and electrochemical response.

4.3.1 Cyclic Voltammetry (CV)

Cyclic voltammetry (CV) was performed to evaluate the electrochemical behavior of CP, CF, and TCF3 under both dark and UV-illuminated conditions at a scan rate of 0.07 V/s. The CV curve obtained for these electrodes is given in Figure 21.

Compared to flat CP, CF has more current density. This mainly arises from three-dimensional porous structures and a larger electrochemically active surface area. In Figure 21, a smooth, broadened curve is observed for both CF and TCF3, whereas for CP, distinct redox peaks are observed. This indicates that CP provides a more uniform surface with a more well-defined Cu^{2+}/Cu^0 redox transition, whereas CF and TCF3 distribute reactions over multiple sites due to their porous heterogeneous structure. In EMAR, Cu^{2+} forms complexes with the amine, leading to multistep redox behavior rather than a single-electron transfer reaction. Additionally, diffusion limitation within the porous structure and surface passivation (e.g. formation of Cu oxide or Cu-amine intermediate layer) may also contribute to the broader curve [85]. These combined effects

result in broadened and smoother CV curves. For EMAR, these broadened CV curves are advantageous as it indicates higher electrochemically active surface area and better Cu utilization.

The TCF3 electrodes exhibited a higher current density compared to CP and CF. The improved electrochemical performance was attributed to the TiO_2 aerogel coating on the copper foam substrate. The aerogel coating introduces additional roughness and an increased effective interfacial area, thereby enhancing the electrochemically active surface area available for redox reactions. In addition, the porous nature of the TiO_2 aerogel powder increases electrolyte penetration and improves the contact area between the electrolyte and the conductive copper substrate.

A noticeable difference was observed between the dark and UV-illuminated TCF3. Under UV illumination, TCF3 exhibited a consistently higher current density compared to dark conditions. This enhancement can be attributed to the photoactive properties of TiO_2, in which UV irradiation generates electron-hole pairs within the TiO_2 structure. The photo-generated electrons contribute to the electrochemical processes, thereby improving the charge transfer and increasing the overall current response. For CP and CF, the difference between UV-off and UV-on conditions is negligible, indicating the absence of photo-induced effects in bare copper systems.

To provide a quantitative comparison, the CV curves were also integrated to obtain the total integrated CV area ($\int j\,dV$, $mA \cdot V/cm^2$), charge density (q, mC/cm^2), and apparent areal capacitance (C_A, mF/cm^2). CP (Dark) exhibited 2.175 $mA.V/cm^2$, 31.08 mC/cm^2, and 23.91 mF/cm^2, while CF showed lower values (1.946 $mA.V/cm^2$, 27.80 mC/cm^2; 21.38 mF/cm^2). This indicates that although CF exhibits a higher current density than CP at a certain potential, its integrated CV area is lower. This suggests that the porous structure improves local electrochemical activity but also introduces distributed transport limitations, which reduce the total response over the full potential

cycle. In contrast, TCF3 showed the highest response (2.686 mA·V/cm²; 38.37 mC/cm²; 29.52 mF/cm² under UV), confirming enhanced activity. The larger reverse-scan contribution for CF and TCF3 compared to CP indicates improved Cu^{2+} reduction and reversibility. This demonstrates the potential of TCF3 for photoelectrochemical applications in the EMAR system, where improved charge-transfer kinetics can directly enhance Cu cycling and solvent regeneration efficiency.

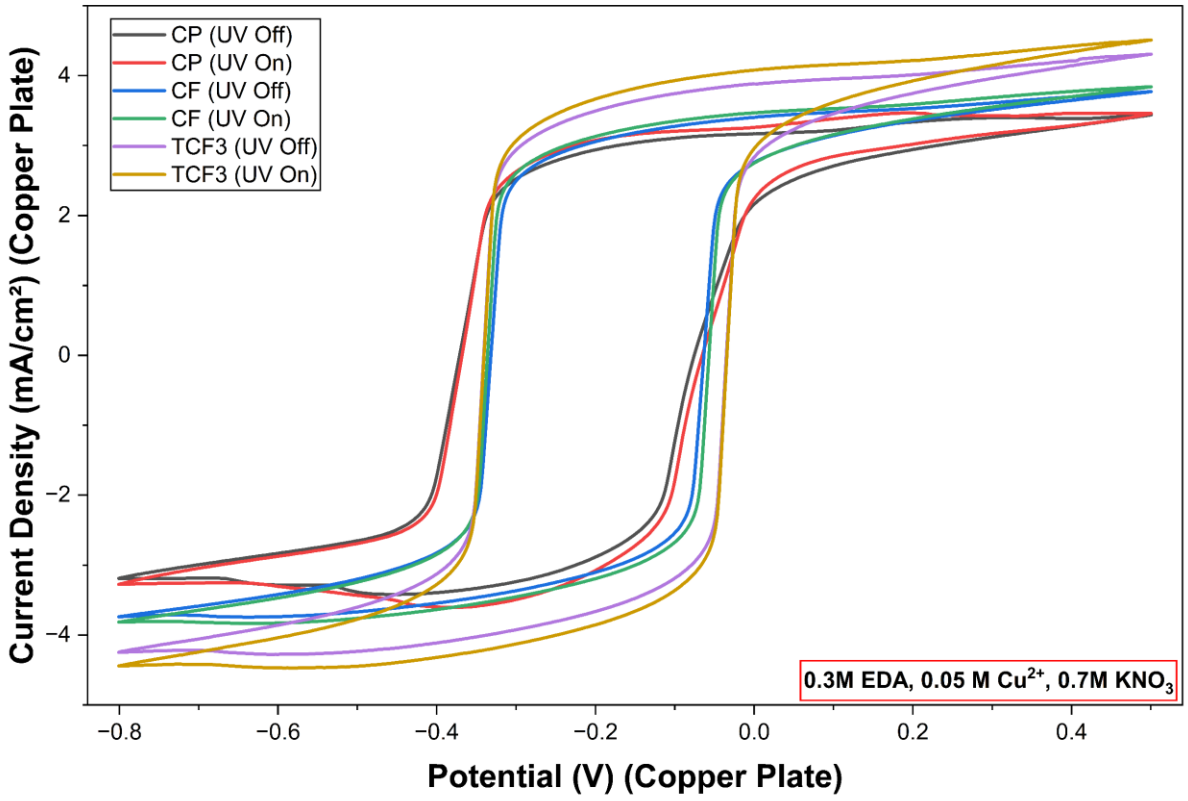

Figure 21: Cyclic voltammetry (CV) curves of copper plate (CP), copper foam (CF), and TiO_2 aerogel–coated copper foam (TCF3) electrodes under dark and UV illumination conditions.

4.3.2 Electrochemical Impedance Spectroscopy (EIS)

The electrochemical impedance spectroscopy (EIS) was conducted to further investigate the charge transfer behavior and interfacial resistance of the CP, CF, and TCF3 (Dark and illuminated

conditions). The Nyquist plot obtained from these measurements is presented in Figure 22. In a Nyquist plot, the semicircle observed in the high-to-mid-range frequency is attributed to the charge-transfer resistance (R_{ct}) at the electrode-electrolyte interface, while the low-frequency region reflects mass transport and diffusion processes.

The CP electrode exhibits the largest impedance response compared to all other electrodes, with a pronounced inclined tail extending towards higher Z' values at low frequencies. This long tail is a characteristic of diffusion-controlled behavior (Warburg impedance). This indicates significant mass transport limitations at the flat copper plate surface. The limited surface area and absence of a porous structure restrict the electrolyte penetration and slows the diffusion of electroactive species, resulting in a higher overall resistance. In comparison, the CF has a smaller semicircle and a shorter low-frequency tail compared to CP. This indicates lower charge transfer resistance, which is primarily attributed to the larger electrochemically active surface area compared to CP. The improved mass transport reduces diffusion limitations and facilitates faster electron transfer during the electrochemical reactions.

The EIS results for TCF3 show a slightly larger semicircle than for CF. These characteristics can be attributed to the presence of a TiO_2 aerogel coating that partially covers the conductive copper substrate. Since TiO_2 acts as a semiconductor under dark conditions, the coating introduces additional interfacial resistance and slightly slows charge transfer. In contrast, when UV is applied to TCF3, the impedance response changes noticeably. The semicircle decreased, indicating reduced charge transfer resistance compared to the dark condition. This improvement can be attributed to the photoactive nature of TiO_2, where UV irradiation generates electron-hole pairs within the aerogel structure. The photogenerated electrons enhance electron transport at the

electrode interface. This facilitates faster charge transfer and lowers the overall impedance of the system.

Overall, the EIS results demonstrate that the porous copper foam structure significantly improves the electrochemical kinetics compared to the flat CP. Furthermore, the addition of UV illumination enables photo-assisted charge transfer, which reduces interfacial charge resistance. This also supports the electrochemical performance observed in the CV measurement.

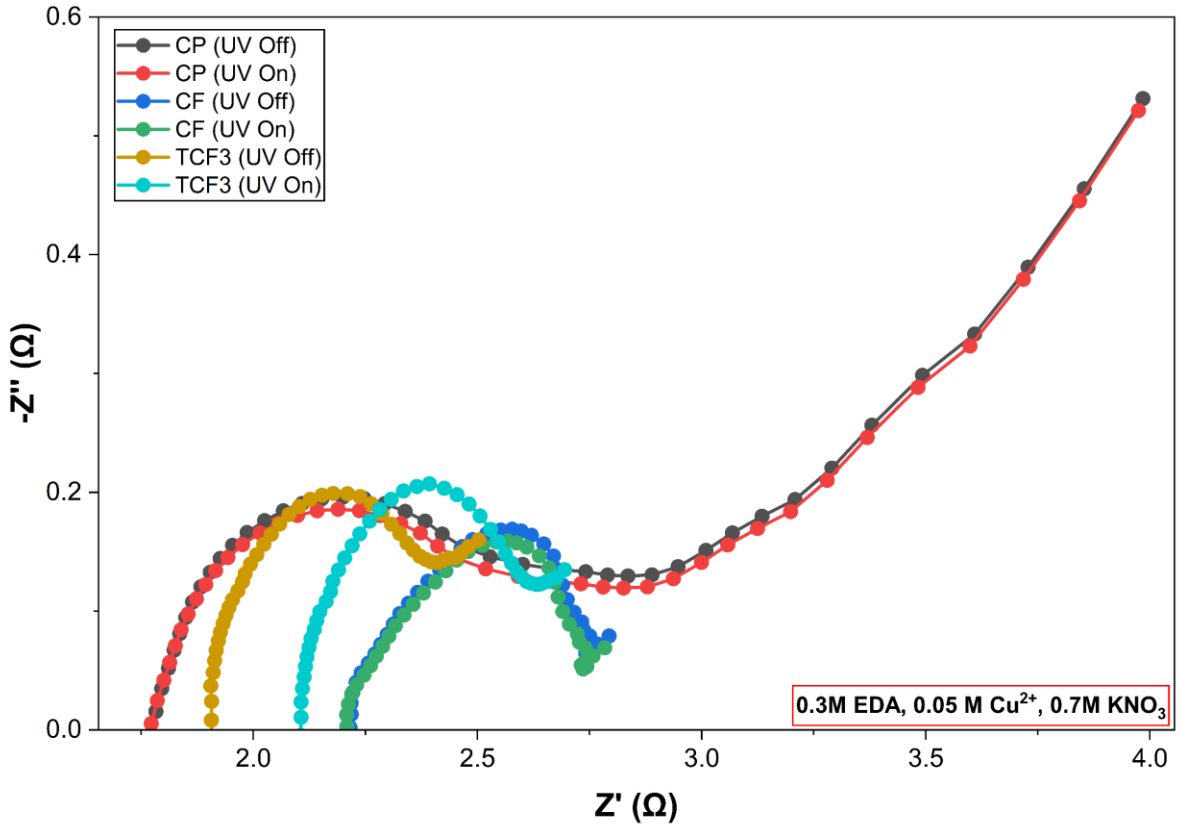

Figure 22: Nyquist plots obtained from electrochemical impedance spectroscopy (EIS) measurements of copper plate (CP), copper foam (CF), and TiO_2 aerogel–coated copper foam (TCF3) electrodes under dark and UV illumination conditions.

4.3.3 Photo-assisted Electrochemical Response Under UV Illumination

Chronopotentiometry was performed to investigate the photo-assisted electrochemical behavior of the TiO_2 aerogel-coated copper foam (TCF3). The experiment was conducted under constant cathodic current (-0.001A) while the UV source was switched on and off periodically every 20 minutes. The potential variation over time is shown in Figure 23.

When UV was applied to the electrode, the potential shifted to more positive value. This behavior indicated that the photogenerated charge carriers from the TiO_2 coating contributed to the electrochemical reduction process. Under UV illumination, TiO_2 absorbs photons and generates electron-hole pairs. The photogenerated electron can participate in the cathodic reaction, thereby reducing the external potential required to maintain the applied current.

When UV was turned off, the electrode potential returned to more negative values. This reversible behavior confirms that the observed potential shift originates from the photoactivity of the TiO_2 aerogel coating in the electrode.

The repeated and consistent response during the UV on-off cycle demonstrates that TiO_2 aerogel coating provides stable photo-assisted electrochemical behavior. These results indicate that the TiO_2 coating can facilitate charge transfer under UV illumination, which supports its potential role in improving the electrochemical regeneration process in the EMAR system.

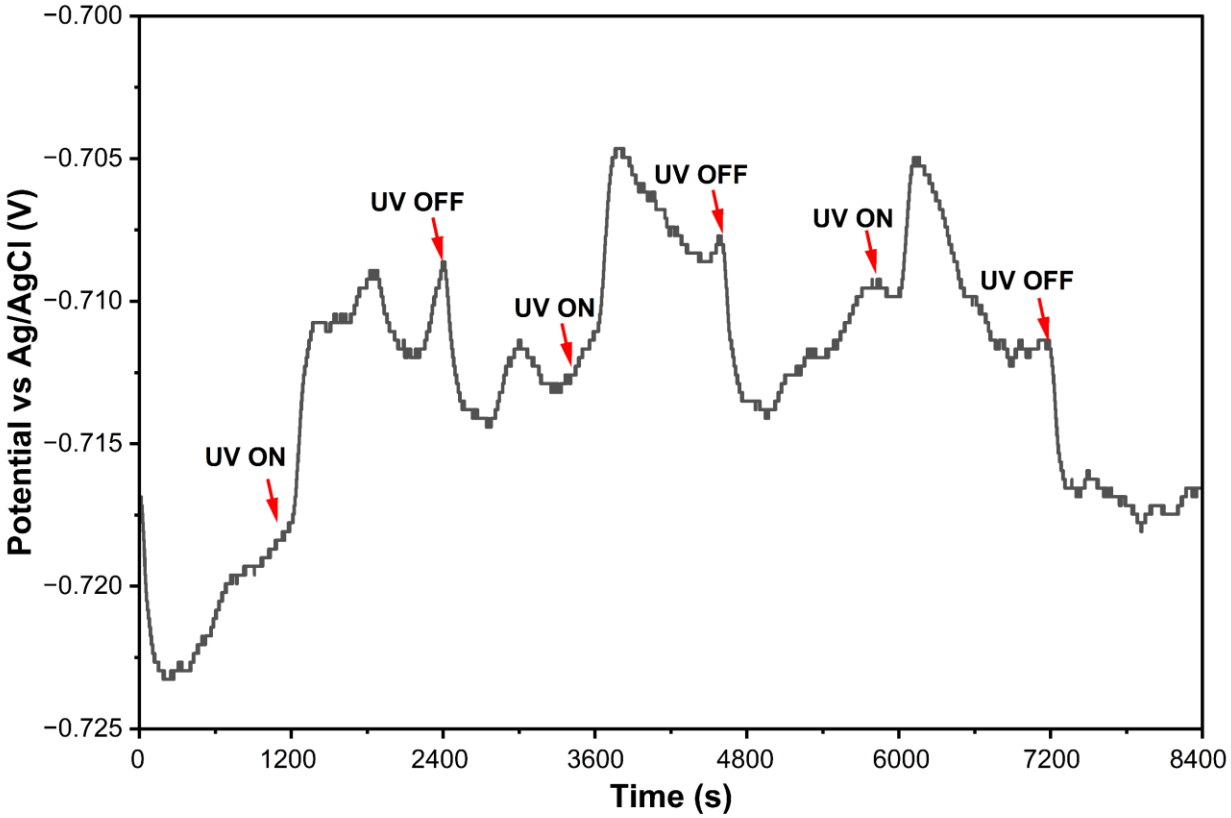

Figure 23: Chronopotentiometric response of the TiO_2 aerogel-coated copper foam electrode (TCF3) under intermittent UV illumination at a constant cathodic current

4.4 Faradaic Efficiency (FE) and Regeneration Energy (RE)

The performance of the EMAR process was evaluated by analyzing the RE and FE for different electrode configurations under both dark and UV conditions. Prior to electrochemical regeneration, the CO_2 capture behavior of the solution (1 M EDA, 1 M KNO_3, and 0.05 M Cu^{2+}) was evaluated using inlet and outlet flow measurements. The CO_2 loading increased progressively and approached ~1 mol CO_2 per mol EDA within 2 h. The CO_2 capture efficiency was initially high and decreased progressively. The absorption rate decreased from approximately 5.6×10^{-3} to below 5×10^{-4} mol min^{-1} over 120 min. This behavior reflects rapid initial CO_2 absorption and gradual decrease as the solvent becomes more loaded with CO_2. Faradaic efficiency (FE)

represents the fraction of electrical charge that contributes to the CO_2 release, while regeneration energy (RE) represents the amount of electrical energy required to regenerate the amine solvent per mole of CO_2 captured. Together, these parameters provide a comprehensive assessment of the EMAR system's electrochemical efficiency and energy performance.

4.4.1 FE and RE as a Function of Different Electrodes

The Faradaic efficiency (FE) obtained for different electrode configurations under UV and dark conditions is presented in Figure 24. In general, UV exposure enhances FE for all electrodes relative to the corresponding dark conditions. Although the improvement is modest at an applied current density of 75 mA/cm^2, all electrodes exhibit slightly higher FE under UV light. For example, the FE of the CP electrode increased from 11.7% in the dark to 12.5% under UV illumination, while CF increased from 19.6% to 20.2%. These improvements may originate from mild thermal effects associated with UV irradiation or enhanced bubble detachment at the electrode surface, both of which can promote electrochemical kinetics and local mass transport [86]. A clear effect of electrode structure is also observed. The CF exhibited higher FE compared to CP. These improvements can be attributed to the porous architecture of the copper foam, as CF has a greater electrochemically active surface area than CP.

The performance of the TiO_2 aerogel-coated copper foam (TCF) electrode strongly depends on the coating thickness. The TCF1 electrode showed a lower FE than the uncoated CF electrode, with a value of approximately 14.8% under UV illumination. These decreases suggest that the initial TiO_2 coating partially covers the conductive copper surface and introduces additional resistance to electron transfer due to TiO_2's relatively low electrical conductivity. At this stage, the TiO_2 coating is still insufficient to significantly increase surface roughness or the number of

electrochemically active sites, so the resistive effects outweigh the potential surface-enhancement benefits.

Increasing the surface layer to three dip layers (TCF3) resulted in the highest FE among all electrodes tested. The FE reached approximately 21.0% under UV illumination, representing the best photoelectrochemical performance of this study. This indicates that an optimal amount of TiO_2 coating enhances the electrode surface by increasing surface roughness and active sites while maintaining effective electron-transport pathways through the conductive copper foam.

Further increases in coating thickness led to a gradual decrease in FE performance. Thicker TiO_2 layers increase the electrical pathways that the electron needs to pass through to reach the electrolyte. Because TiO_2 layers are less conductive than copper foam, excessive thickness can increase the interfacial resistance and slow the Cu redox reactions responsible for the EMAR process. As a result, decreased FE values were observed for both TCF5 and16.1% TCF7. Under UV illumination, the FE for TCF5 was 16.1% and for TCF7 it was 15.38%. In the dark condition, the FE for TCF5 was 15.5% and the FE for TCF7 was 14.9%. This decline suggests that excessive coating thickness begins to hinder electron transfer and mass transport within the porous structure of the electrode.

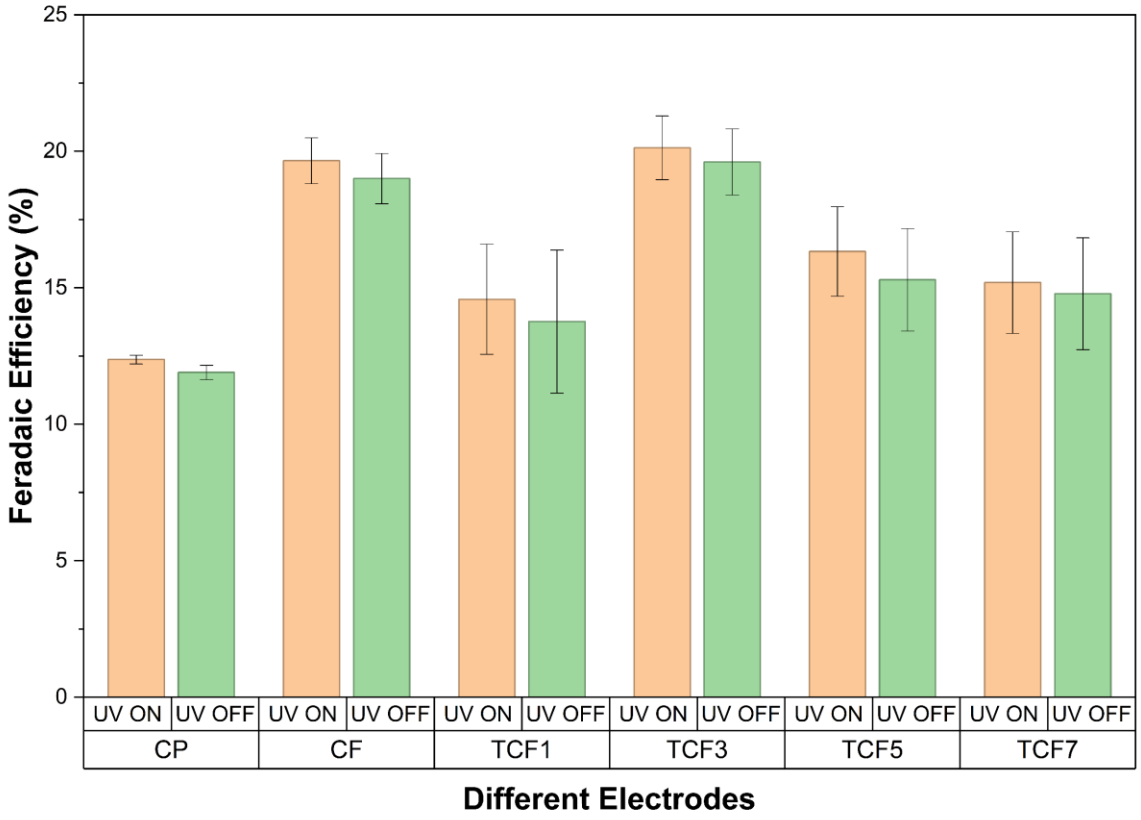

Figure 24: Faradaic efficiency (FE) obtained for different electrode configurations (CP, CF, TCF1, TCF3, TCF5, and TCF7) under UV illumination and dark conditions at 75 mA/cm^2 current density during EMAR operation using an electrolyte containing 1 M EDA, 0.05 M $CuSO_4 \cdot 5H_2O$, and 1 M KNO_3 at 40 °C with an electrolyte flow rate of 65 mL min^{-1}.

The Regeneration energy (RE) for the same set of electrodes is shown in Figure 25. The UV illumination consistently resulted in lower RE compared to dark conditions for all electrodes. For instance, RE of the CP electrode decreased from approximately 1005 kJ/mol CO_2 in dark conditions to about 943 kJ/mol CO_2 under UV illumination. Similar reduction was also observed for other electrodes too. CF decreased from 589 to 571 kJ/mol CO_2, and TCF3 reduced from 575 to 553 kJ/mol CO_2. Since RE represents the electrical energy required for the solvent regeneration, these results indicate that UV illumination has a limited impact on regeneration energy at this current density. This is because at this current density, the electrochemical driving force dominates

the system behavior. For comparison, conventional thermal amine regeneration typically requires approximately 240 kJ/mol CO_2, while optimized EMAR systems have demonstrated regeneration energies as low as 50 kJ/mol CO_2. The comparatively higher RE values observed in this study are attributed to system-level limitations, including cell configuration, ohmic resistance, electrode spacing, and mass transport constraints inherent to the present setup.

Consistent with the FE results, the TCF3 electrode demonstrated the lowest RE (553 kJ/mol CO_2) among all electrodes under UV conditions, while the regeneration energy of TCF1 was higher than that of CF, and an increasing trend was observed for both TCF5 and TCF7. The higher RE value of TCF1 suggests that the initial TiO_2 coating introduces some resistance before the coating thickness reaches an optimal level. As the coating thickness increases further, the RE increases too. These trends reinforce the conclusion that excessive coating thickness negatively affects electron transport and increases the electrical energy required for the electrochemical regeneration.

Overall, the results indicate that the TCF3 electrode provides the most favorable balance between the surface enhancement and electrical conductivity, resulting in the highest FE and lowest RE. It should also be noted that the difference between the UV and dark conditions are relatively small at the applied current density of 75mA/cm^2. Under such conditions, the electrochemical driving force dominates the system's behavior, limiting the contribution of photo effects [87]. However, the consistent small improvement under UV suggests that light-induced effects are present. The influence of current density on these UV-assisted effects is examined in greater detail in the following section.

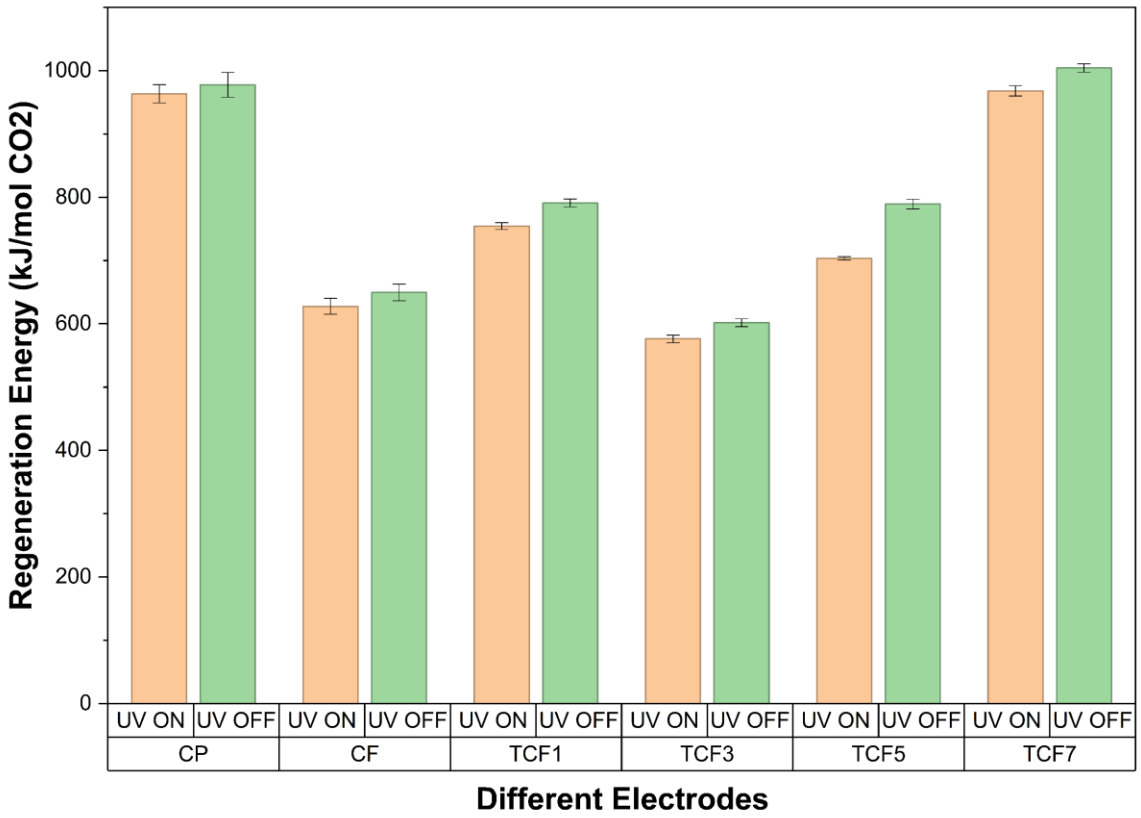

Figure 25: Regeneration energy (RE) required for different electrode configurations (CP, CF, TCF1, TCF3, TCF5, and TCF7) under UV illumination and dark conditions during EMAR operation using an electrolyte containing 1 M EDA, 0.05 M $CuSO_4 \cdot 5H_2O$, and 1 M KNO_3 at 40 °C with an electrolyte flow rate of 65 mL min^{-1}.

4.4.2 FE and RE as a Function of Current Density

The influence of current density on the FE for CP, CF, and TCF3 under both dark and UV illuminated conditions is presented in Figure 26. In general, FE increases as the current density decreases from 75 mA/cm^2 to 25 mA/cm^2 for all electrodes tested. This trend indicates that the lower current density allows for more efficient electron utilization compared to higher current density.

For the CP electrode, the FE increased from approximately 11.0% at 75 mA/cm² to 22.6% at 25 mA/cm² under dark conditions. The FE increased from 12.5% at 75 mA/cm² to 23.1% at

25 mA/cm² when UV illumination was applied. A similar trend was observed for the CF electrode, where FE increased from 19.6% to 29.5% under dark conditions and from 20.2% to 30.0% under UV illumination as the current density decreased from 75 to 25 mA cm/². These trends indicate that reducing current density significantly improves Faradaic charge utilization in the EMAR system.

Among all the tested electrodes, TCF3 showed the best FE under all conditions. Under dark conditions, the FE increased from approximately 20.5% at 75 mA/cm² to 32.8% at 25 mA/cm². When UV illumination was applied, the FE further increased from 21.0% to 35.7% over the same current-density range. The superior performance of TCF3 indicates that optimized TiO_2 coating enhances the electrochemical surface while maintaining efficient electron transport through copper foam structure.

A comparison between UV and dark conditions reveals different behavior in CP and TCF3. As the current density decreases, the FE difference between the UV and dark conditions of CP also decreases, whereas an opposite effect is observed for TCF3. In the case of CP, due to the absence of TiO_2, UV illumination doesn't generate any photoelectrons. Thus, the improvement in UV conditions compared to the dark conditions arises primarily from local heating or improved bubble detachment. However, at lower current density, the electrochemical reactions already proceed more efficiently, and these minor effects of UV become less significant. In contrast, the presence of TiO_2 in TCF3 generates photoelectrons under UV illumination. These additional charges are involved in the Cu redox reactions of EMAR chemistry. At higher current density, the reaction is dominated by the externally supplied electrons from the power source. Thus, the relative contribution of the photogenerated carrier is small. However, at lower current density, the relative

contribution of these photo-assisted processes becomes more noticeable, resulting in a higher FE under UV illumination.

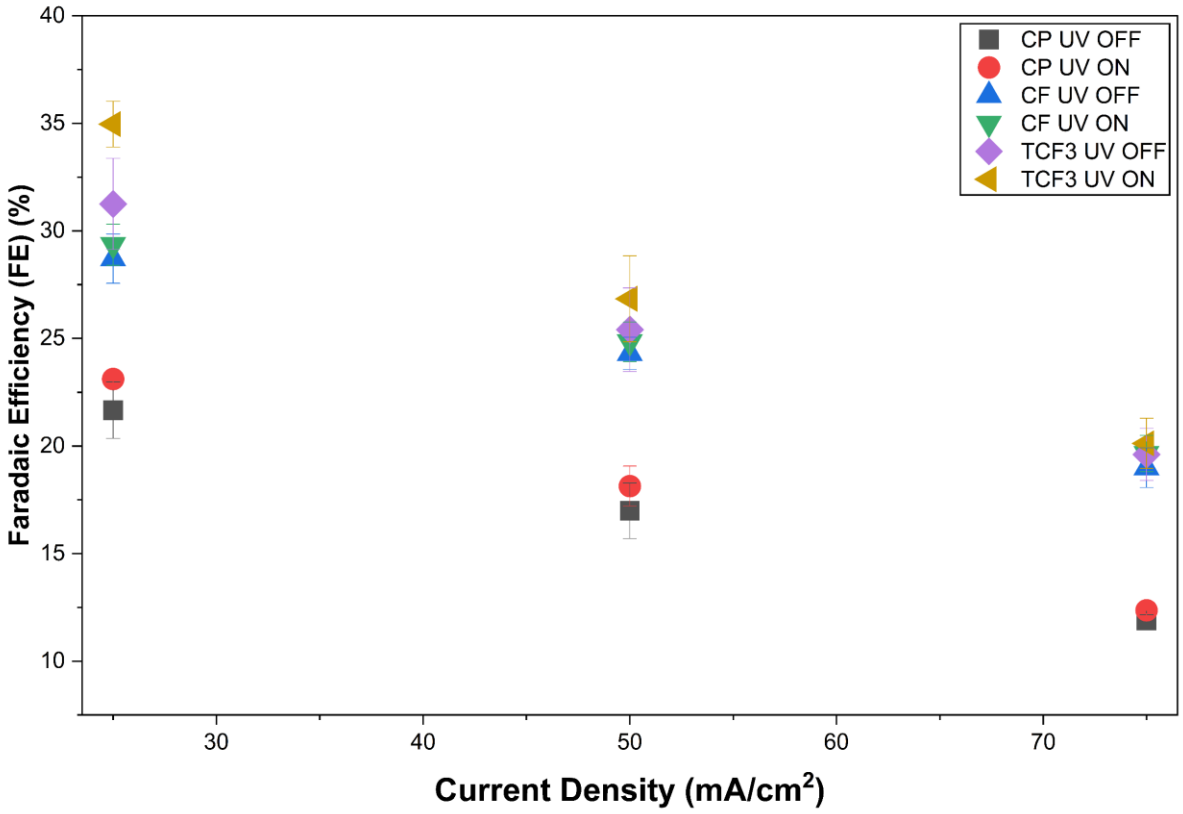

Figure 26: Faradaic efficiency (FE) as a function of current density for CP, CF, and TCF3 electrodes under UV illumination and dark conditions during EMAR operation using an electrolyte containing 1 M EDA, 0.05 M $CuSO_4 \cdot 5H_2O$, and 1 M KNO_3 at 40 °C with an electrolyte flow rate of 65mL/min

The corresponding regeneration energy (RE) as a function of current density is presented in Figure 27. In contrast to the FE trends, RE decreases as the current density decreases. For the CP electrode, the regeneration energy decreased from approximately 1069 kJ/mol CO_2 at 75 mA/cm² to about 320 kJ/mol CO_2 at 25 mA/cm² under dark conditions. Under UV illumination, the RE decreased from approximately 858 kJ/mol CO_2 to about 296 kJ/mol CO_2 over the same current density range.

Similar trend was also observed for the CF electrode, where the regeneration energy decreased from approximately 589 kJ/mol CO_2 at 75 mA/cm² to 261 kJ/mol CO_2 at 25 mA/cm² under dark conditions. When UV illumination was applied, the RE decreased further, from about 572 kJ/mol CO_2 to 244 kJ/mol CO_2, as the current density decreased from 75 to 25 mA/cm².

The TCF3 electrode again showed the most favorable energy performance among the tested electrodes. Under dark conditions, the regeneration energy decreased from approximately 575 kJ/mol CO_2 at 75 mA/cm² to about 200 kJ/mol CO_2 at 25 mA/cm². Under UV illumination, the regeneration energy decreased even further from approximately 553 kJ mol CO_2 to about 140 kJ/mol CO_2 over the same current density range. This substantial reduction reflects the improved electrochemical efficiency achieved with the optimized TiO_2-coated electrode.

Consistent with FE trends, the effect of UV illumination becomes more pronounced as the current density decreases. While the difference between the dark and UV conditions is relatively small at 75 mA/cm^2, the gap widens at lower current densities. This observation further supports the conclusion that photo-assisted effects contribute more significantly when the electrochemical driving force is reduced.

Overall, these results demonstrate that both electrode structures and operating current density strongly influence EMAR performance. Lower current densities improve Faradaic efficiency while simultaneously reducing the energy required for regeneration, and the optimized TiO_2-coated electrode (TCF3) consistently delivers the best electrochemical performance under both UV and dark conditions.

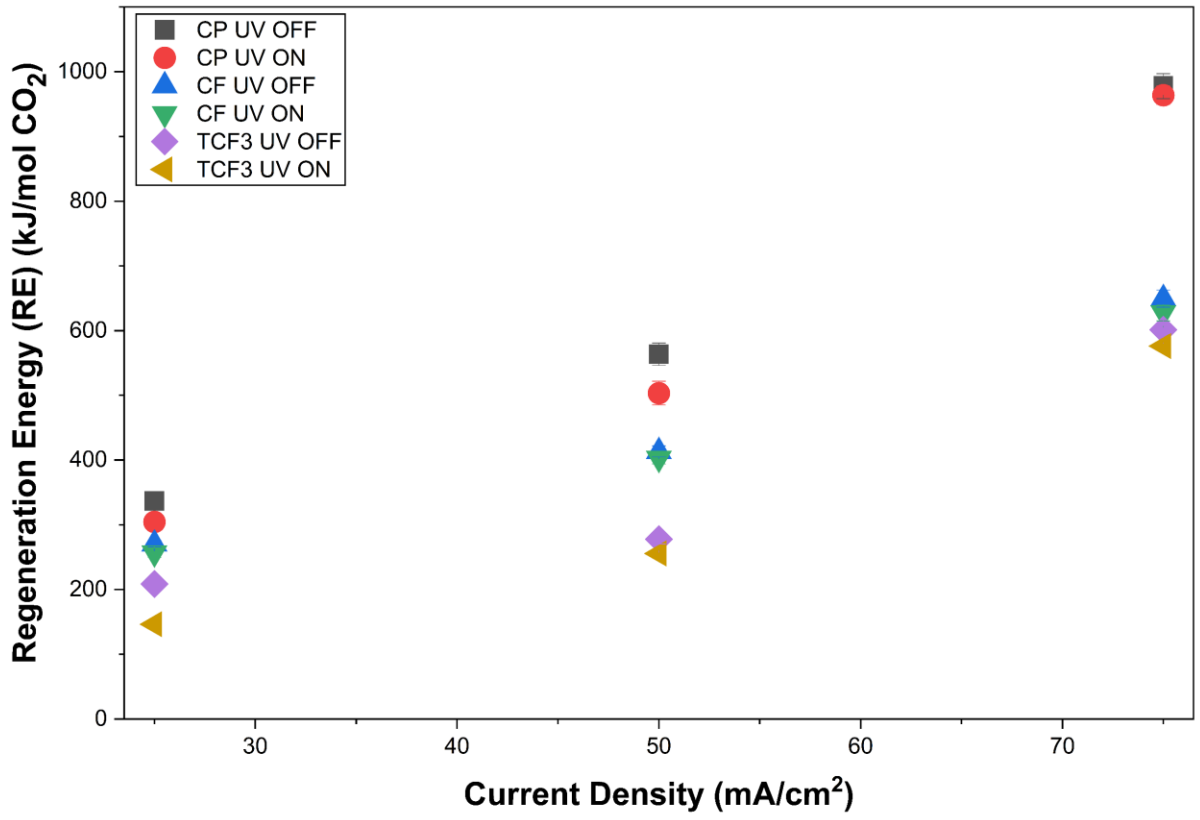

Figure 27: Regeneration Energy (RE) as a function of current density for CP, CF, and TCF3 electrodes under UV illumination and dark conditions during EMAR operation using an electrolyte containing 1 M EDA, 0.05 M $CuSO_4 \cdot 5H_2O$, and 1 M KNO_3 at 40 °C with an electrolyte flow rate of 65 mL/min

4.4.3 FE and RE as a Function of Copper Ion Concentration

The influence of copper ion concentration on the Faradaic Efficiency (FE) under both dark and illuminated conditions is presented in Figure 28. At the lowest copper concentration (0.05M), FE reached approximately 32.8% under dark conditions and increased to 35.7% under UV conditions. As the copper ion concentration increased, the FE values under the dark and UV conditions became progressively closer. At 0.10 M Cu^{2+}, the FE reached 33.2% under dark conditions and 34.5% under UV illumination, while at 0.15 M Cu^{2+}, the FE values were 33.5% and 34.3% for dark and UV conditions, respectively. This indicates that UV illumination provides

a more noticeable improvement at lower copper concentrations, whereas the difference between UV and dark conditions becomes smaller at intermediate concentrations.

To further investigate the influence of copper concentrations on photo-assisted behavior, UV-vis spectroscopy was performed on electrolytes with varying Cu^{2+} concentrations (Figure 30). The absorbance increased with increased copper concentration. The electrolyte containing 0.05 M Cu^{2+} exhibited the lowest absorbance, whereas higher-concentration solutions showed increased absorbance without significant peak shifts. This trend confirms that increasing Cu^{2+} concentration enhances optical attenuation within the solution. The increased optical absorbance suggests reduced overall light penetration through the electrolyte, which can limit the effective photon flux reaching the TiO_2-coated electrode surface and thereby reduce the enhancement of the photo-assisted charge transfer.

At higher copper concentrations, several factors may reduce the effectiveness of the photo-assisted process. Elevated Cu^{2+} concentrations may introduce mass-transfer limitations or promote parasitic side reactions in the electrolyte. In addition, higher copper loadings may lead to increased electrolyte viscosity or excessive copper deposition on the electrode surface, which can reduce the effective electrochemical surface area and hinder efficient electron transfer. This observation is consistent with the reduced improvement in Faradaic efficiency under UV illumination at higher concentrations.

In the present setup, the distance between the quartz window and the electrode surface was approximately 2.2 cm, which may further reduce the effective light intensity reaching the electrode under highly concentrated solutions. As a result, when the copper concentration was further increased to 0.20 M, the FE decreased to approximately 27.1% under dark conditions and 28.3%

under UV illumination, indicating that excessive copper loading negatively affects the overall electrochemical efficiency of the EMAR system.

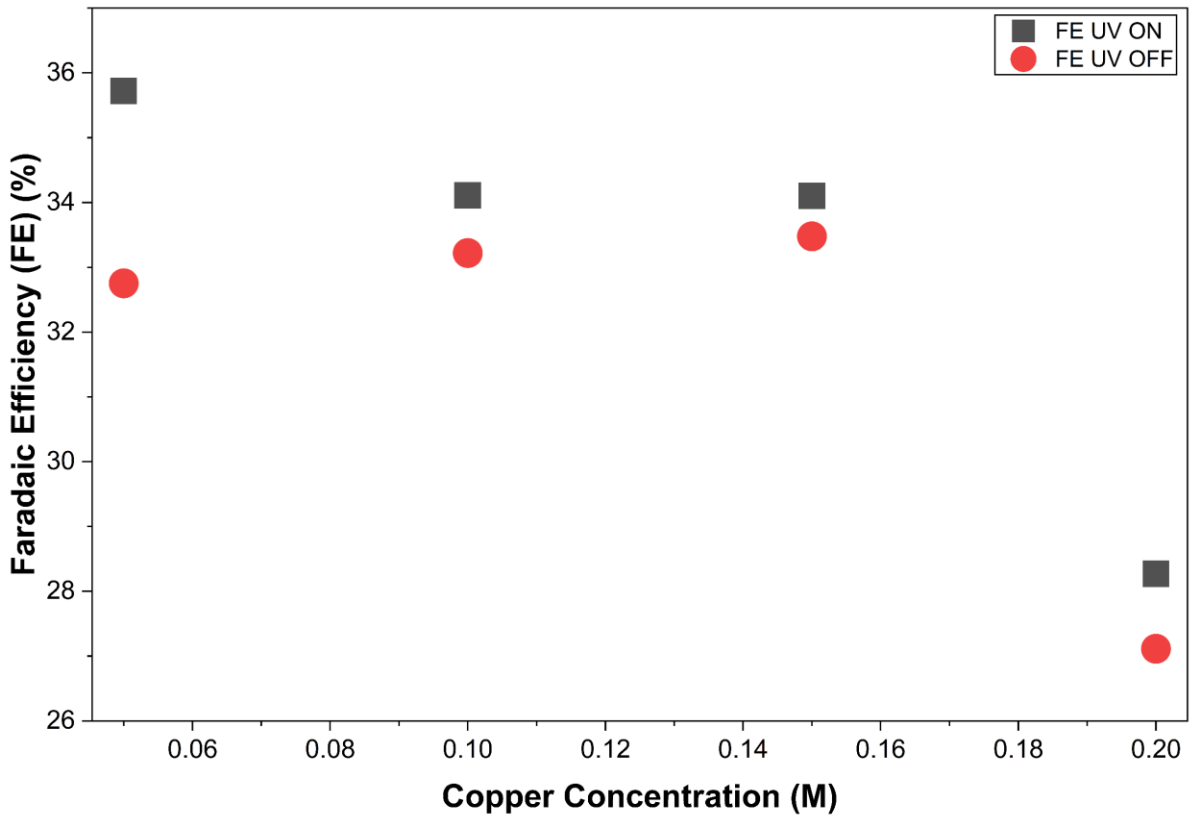

Figure 28: Faradaic efficiency (FE) as a function of Cu^{2+} concentration under dark and UV-illuminated conditions in the EMAR system.

The corresponding regeneration energy (RE) as a function of copper concentration under both dark and UV illuminated conditions is presented in Figure 29. At the lowest copper concentration (0.05 M), the RE reached approximately 200 kJ mol^{-1} CO_2 under dark conditions and decreased to about 140 kJ mol^{-1} CO_2 under UV illumination. As the Cu concentration increased, the RE values under dark and UV conditions became progressively closer. At 0.10 M Cu, the RE decreased to 186 kJ mol^{-1} CO_2 under dark conditions and 169 kJ mol^{-1} CO_2 under UV illumination, while at 0.15 M Cu, the values were 173 kJ mol^{-1} CO_2 and 170 kJ mol^{-1} CO_2,

respectively. This trend indicates that UV illumination provides the largest energy benefit at lower copper concentrations, whereas the difference between UV and dark conditions becomes smaller at intermediate concentrations.

Overall, both Figures 28 and 29 show that optimal RE and FE can be obtained at copper concentrations around 0.15 M under dark conditions. However, in the presence of UV, a better optimum point can be obtained even at lower concentrations.

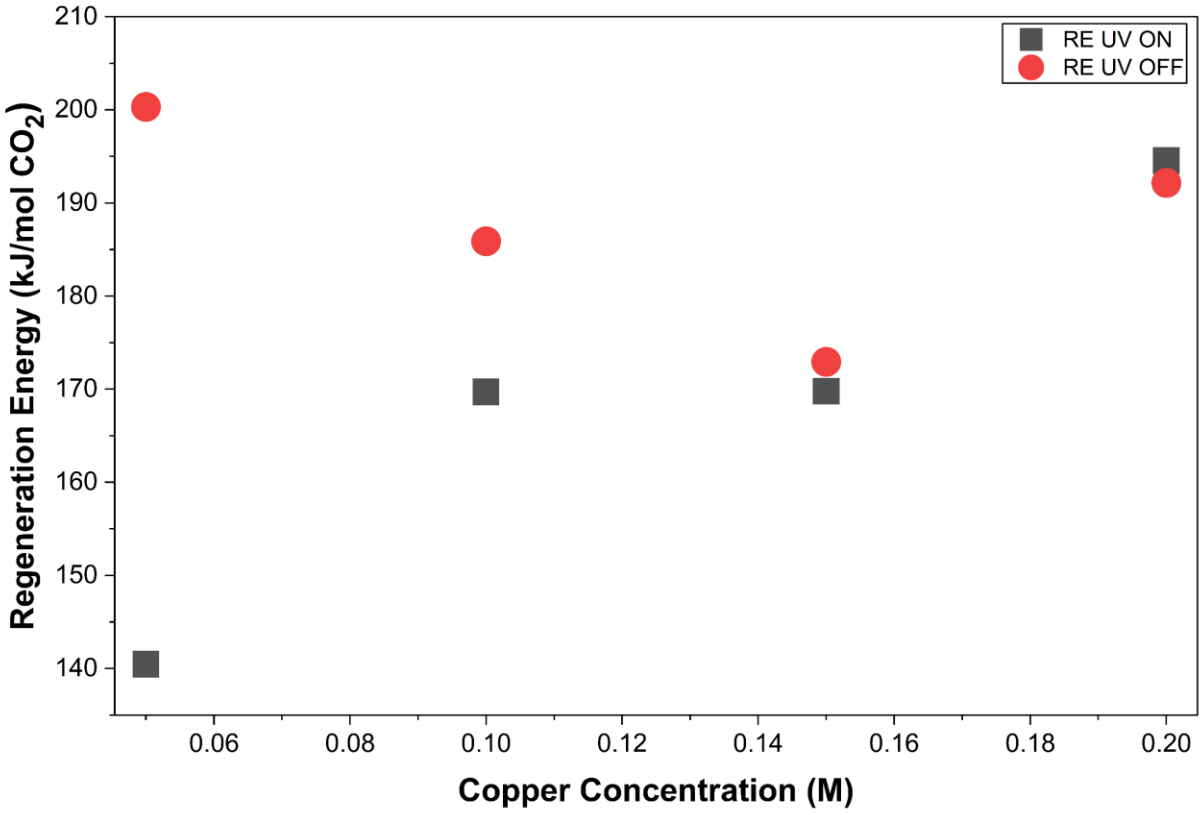

Figure 29: Regeneration energy (RE) as a function of Cu^{2+} concentration under dark and UV-illuminated conditions in the EMAR system.

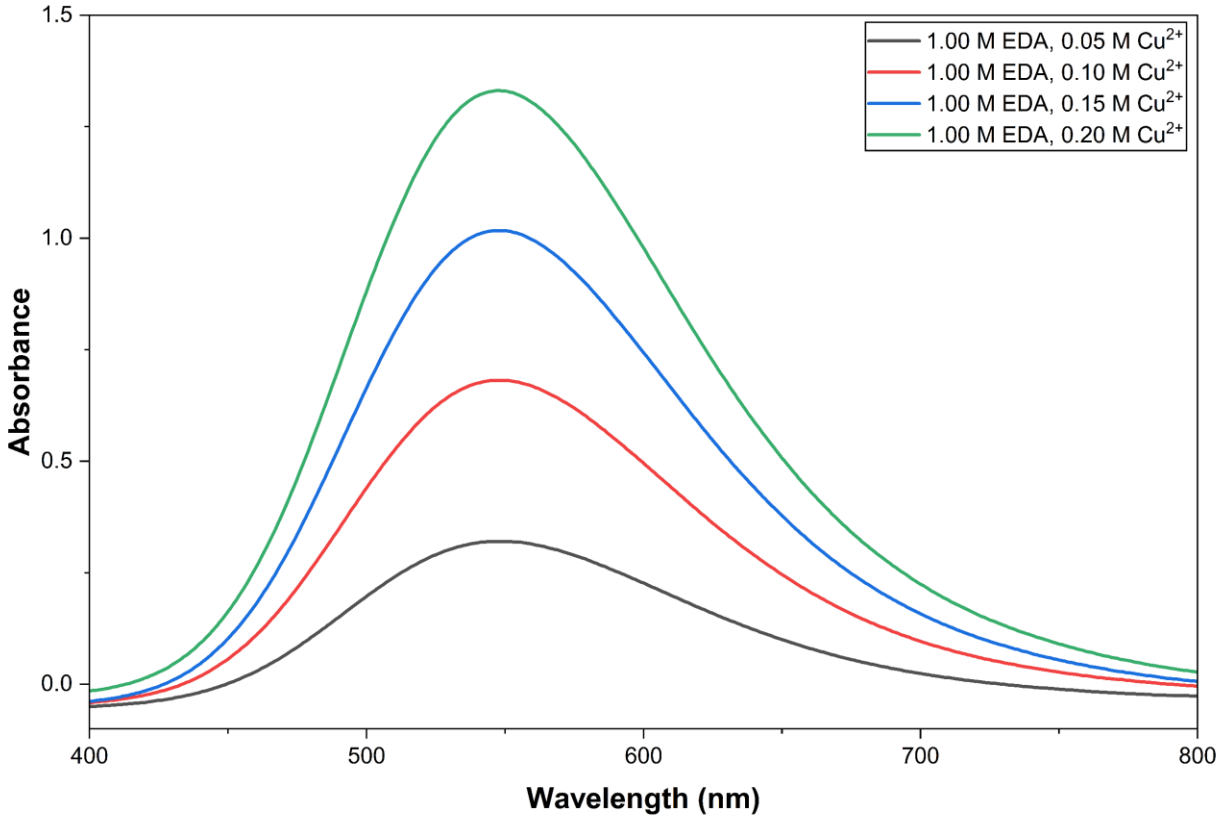

Figure 30: UV–Vis absorbance spectra of electrolytes with varying Cu^{2+} concentrations (0.05–0.20 M) at constant amine concentration (1 M EDA), showing increased optical attenuation with increasing copper concentration.

4.4.4 FE and RE as a Function of Amine Concentration Variant

The Influence of amine concentration on Faradaic efficiency (FE) under both dark and UV illuminated conditions is presented in Figure 30. Amine concentration plays a critical role in EMAR performance as it determines the availability of the reactive sites for CO_2 capture and influences the transport properties of the electrolyte.

At the lowest concentration of 0.25 M EDA, the FE was 19.37% under UV illumination and 18.35% in the dark, indicating relatively poor charge utilization. As the amine concentration increased to 0.5 M, the FE increased significantly to 27.63% (UV On) and 26.37% (UV Off). A further increase to 0.75 M resulted in the highest FE values, reaching 37.06% under UV

illumination and 35.37% in the dark. However, when the amine concentration increased further to 1.0 M, the FE decreased slightly to 35.72% (UV On) and 32.75% (UV Off). The difference between 0.75 M and 1.0 M is relatively small, indicating that the system remains near its optimum performance within this concentration range, although excessively high amine concentrations may begin to introduce transport limitations within the electrolyte.

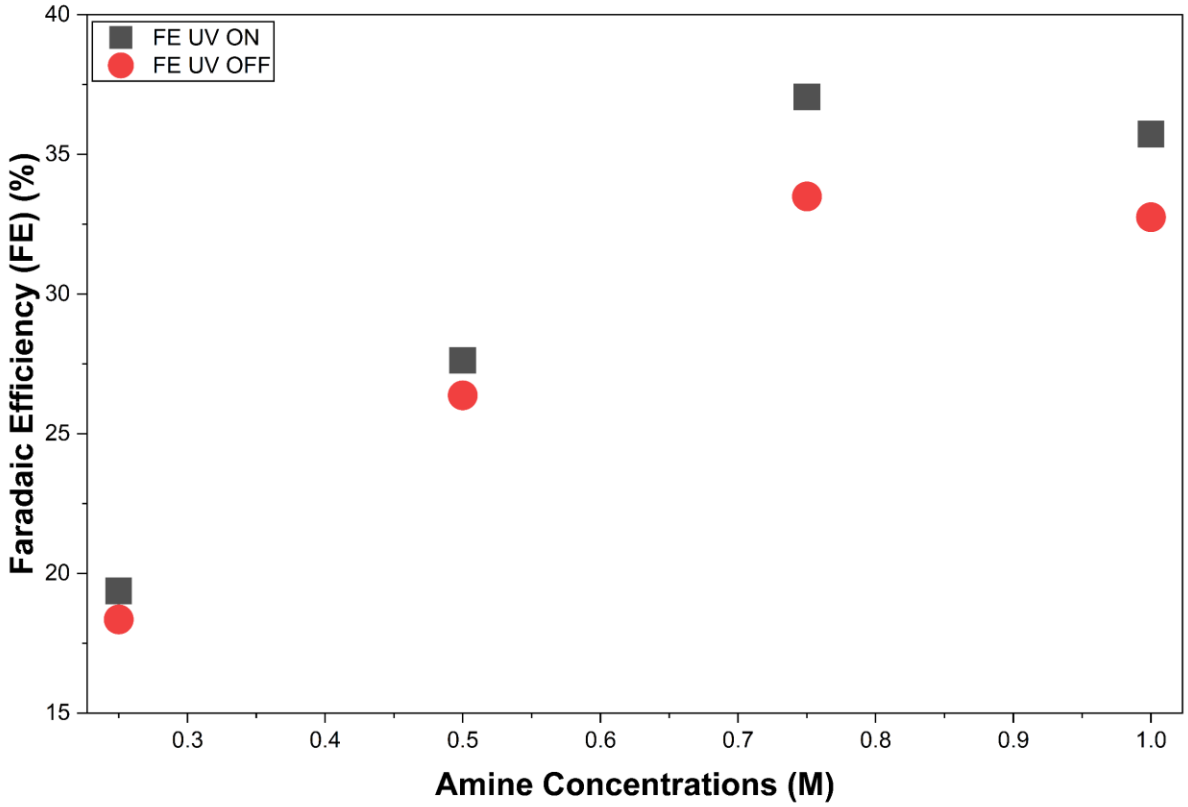

Figure 31: Faradaic efficiency (FE) as a function of ethylenediamine (EDA) concentration under dark and UV-illuminated conditions.

The corresponding regeneration energy as a function of amine concentration is presented in Figure 31. At 0.25 M, the RE was the highest, reaching 313.82 kJ mol^{-1} CO_2 under UV illumination and 368.05 kJ/mol CO_2 under dark conditions, indicating inefficient regeneration when the amine concentration is insufficient. Increasing the concentration to 0.5 M reduced the regeneration

energy substantially to 209.54 kJ/mol CO_2 (UV On) and 259.73 kJ/mol CO_2 (UV Off). The lowest regeneration energy occurred at 0.75 M, where the RE decreased to 137.98 kJ/mol CO_2 under UV illumination and 169.13 kJ/mol CO_2 under dark conditions. Similar to the FE trend, increasing the amine concentration further to 1.0 M resulted in a slight increase in regeneration energy to 140.45 kJ/mol CO_2 (UV On) and 200.31 kJ/mol CO_2 (UV Off). The change in RE between 0.75 M and 1.0 M is relatively small for the UV-illuminated case, further confirming that 0.75–1.0 M lies near the optimal operating region for the present EMAR system.

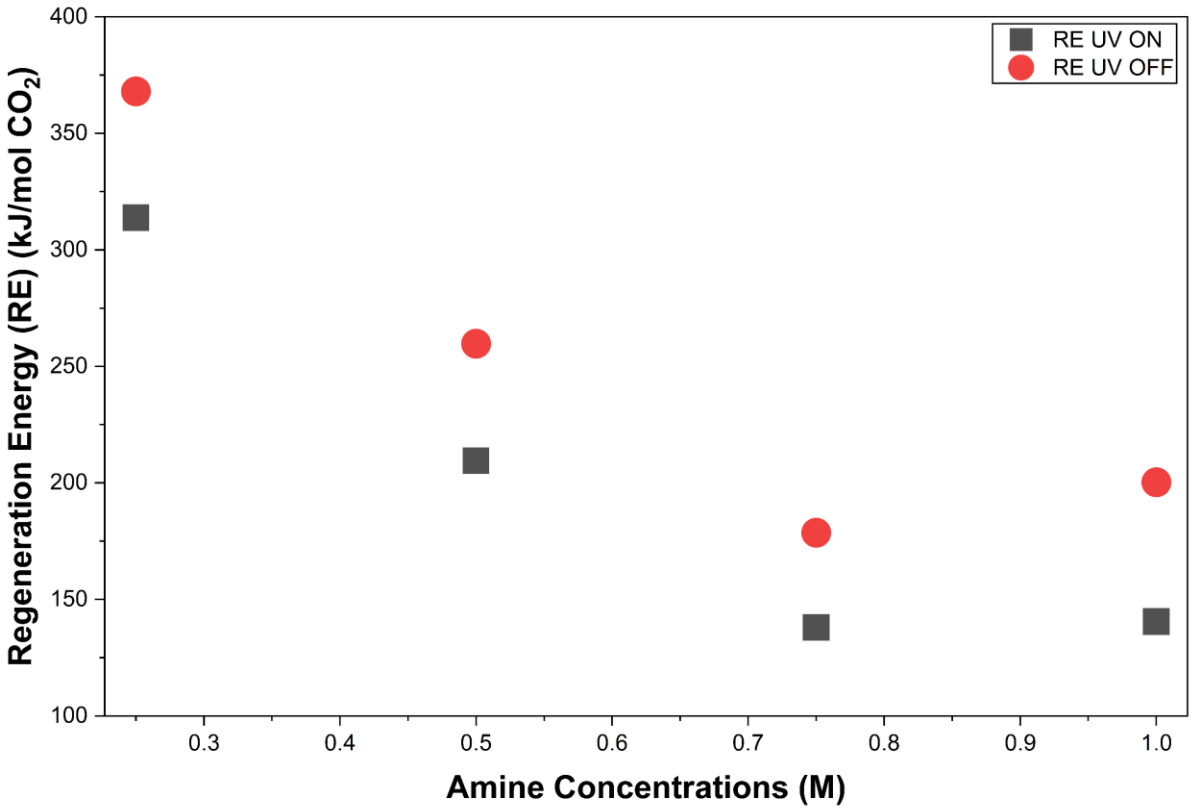

Figure 32: Regeneration energy (RE) as a function of ethylenediamine (EDA) concentration under dark and UV-illuminated conditions

Overall, the results indicate that 0.75M EDA provides the optimal concentration of the EMAR system under the present experimental conditions. At lower concentrations, the system is

limited by insufficient amine availability, which reduces carbon capture efficiency and increases electrical energy consumption. In contrast, high amine concentrations increase electrolyte viscosity and hinder the diffusion of CO_2 and copper complexes within the electrolyte. Additionally, UV illumination consistently improves the FE and RE across the entire concentration range. The photo-generated charge carriers produced by the TiO_2 aerogel coating enhance the electrochemical reduction of copper species and stabilize the electrochemical environment, enabling more efficient EMAR operation.

4.4.5 FE and RE as a Function of Flow Variant

The influence of electrolyte flow rate on the Faradaic efficiency (FE) under both dark and UV illuminated conditions is presented in Figure 32. At the lowest flow rate of 25 mL/min, the FE reached its highest value of 45.50% under UV illumination and 42.65% under dark conditions. As the flow rate increased to 45 mL/min, the FE decreased slightly to 43.51% (UV On) and 40.16% (UV Off). When the flow rate was further increased to 65 mL/min, the FE decreased more noticeably to 35.72% under UV illumination and 32.75% under dark conditions. At the highest tested flow rate of 85 mL/min, the FE decreased further to 33.72% (UV On) and 29.09% (UV Off).

The continuous decrease in FE with increasing flow rates indicates that the EMAR system is highly sensitive to electrolyte flow. At lower flow rates, the copper-amine complexes remain in contact with the electrode for a longer time. This allows sufficient time for the electrochemical reactions responsible for CO_2 release to occur. As the flow rate increases, the electrolyte moves more rapidly, reducing the contact time of the electrolyte with the electrodes. As a result, the electrochemical regeneration reaction becomes incomplete, leading to a lower FE. Despite this reduction in FE, UV illumination consistently provides slightly higher efficiencies compared to

dark conditions across all flow rates. This indicates that the photo generated charge carriers from the TiO_2 coating helps sustain the electrochemical reaction.

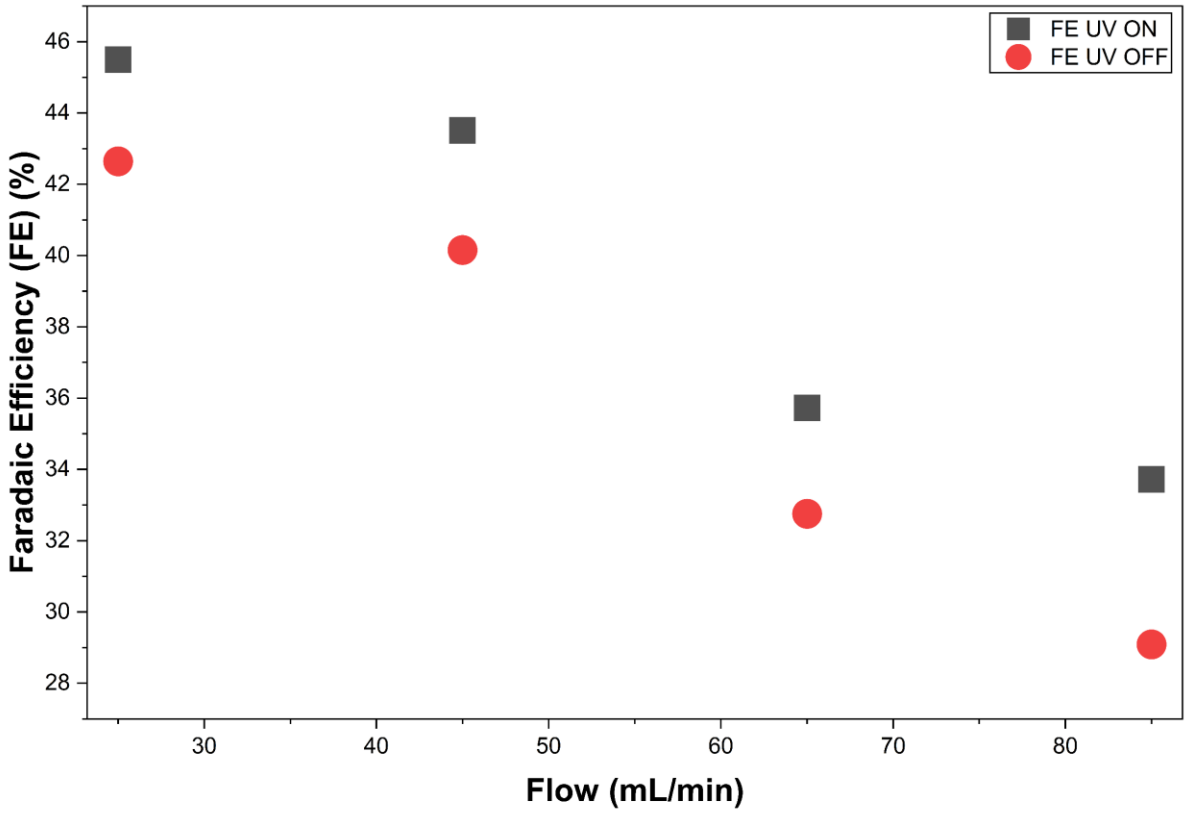

Figure 33: Faradaic efficiency (FE) as a function of electrolyte flow rate under dark and UV-illuminated conditions

The corresponding regeneration energy (RE) as a function of flow rate is presented in Figure 33. At 25 mL/min, the regeneration energy was 139.96 kJ/mol CO_2 under UV illumination and 149.33 kJ/mol CO_2 under dark conditions. Increasing the flow rate to 45 mL min^{-1} reduced the regeneration energy further to 119.74 kJ/mol CO_2 (UV On) and 144.17 kJ/mol CO_2 (UV Off), representing the lowest energy requirement for the present system.

When the flow rate increased to 65 mL/min, the regeneration energy increased to 140.45 kJ mol^{-1} CO_2 under UV illumination and 200.31 kJ/mol CO_2 under dark conditions. A

further increase to 85 mL/min resulted in regeneration energies of 157.38 kJ/mol CO_2 (UV On) and 202.31 kJ/mol CO_2 (UV Off). This increase suggests that excessively high flow rates reduce the effective residence time of copper complexes near the electrode surface, limiting the completion of the electrochemical regeneration reaction and increasing the overall energy requirement.

Overall, the results indicate that 45 mL/min represents the optimal flow rate for the present EMAR system. At lower flow rates, the system experiences concentration polarization due to insufficient electrolyte movement near the electrode surface, whereas at high flow rates, it reduces the residence time of reactive species and decreases the FE. The flow rate of 45ml/min, therefore, provides the best balance between adequate mass transport and sufficient reaction time for efficient electrochemical regeneration.

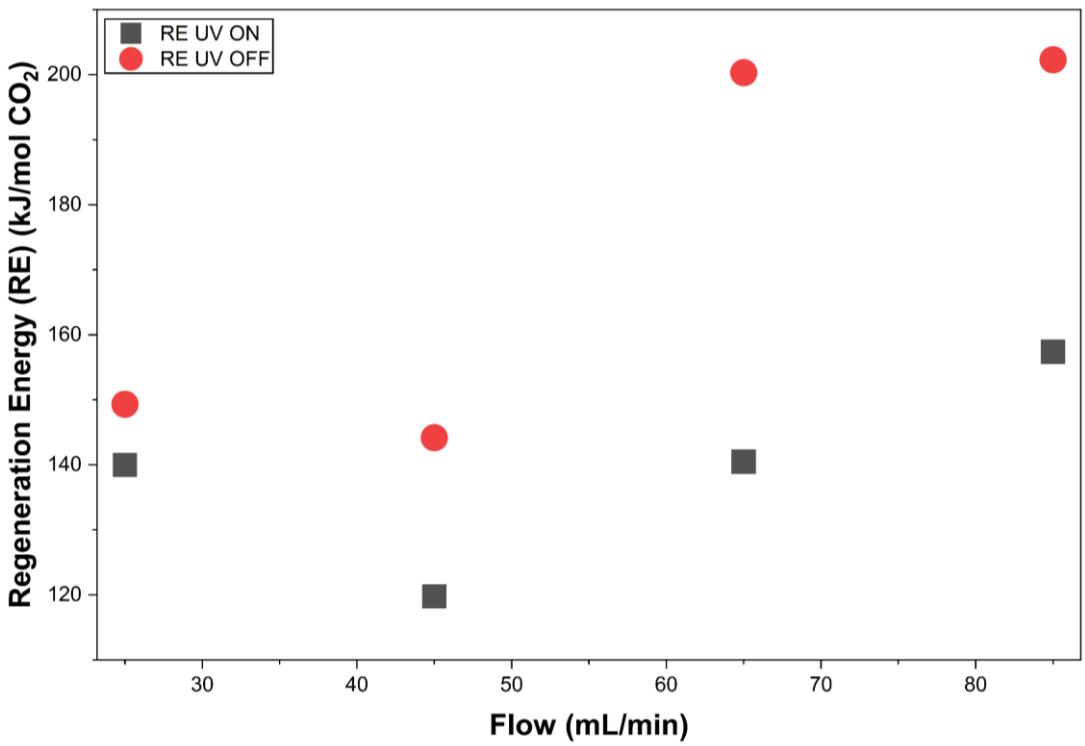

Figure 34: Regeneration energy (RE) as a function of electrolyte flow rate under dark and UV-illuminated conditions

Chapter 5 Conclusions

5.1 Summary of the Key Findings

This thesis investigated the application of TiO_2 aerogel-coated copper foam electrode in the Electrochemically Mediated Amine Regeneration (EMAR) process under UV illumination. By integrating photocatalytic TiO_2 aerogel with a three-dimensional copper foam structure, the system combines high surface area with photo-generated charge carriers that can assist the Cu redox reactions responsible for CO_2 release.

Structural characterization confirmed the successful fabrication of a TiO_2 aerogel-coated electrode. SEM images showed that the TiO_2 aerogel formed a nanostructured layer on the copper ligaments. This allowed the copper foam to retain its interconnected porous structure after coating. XPS analysis verified the presence of titanium and oxygen across the copper framework, confirming the successful deposition of photocatalytic material. In addition, XRD and Raman analysis identified the anatase phase of TiO_2, which is known for its strong photocatalytic activity and is responsible for generating photo-induced charge carriers under UV illumination.

Electrochemical comparison between different electrodes demonstrated the advantage of the TiO_2-coated copper foam structure. Bare copper plate (CP), copper foam (CF), and three times TiO_2-coated copper foam were evaluated. The results showed that copper foam electrodes significantly outperform copper plates due to their higher surface area and improved mass transport. When the TiO_2 aerogel coating was introduced on the copper foam (TCF3), additional improvements were observed due to photo assisted charge transfer under UV illumination.

At a current density of 75 mA/cm^2, the FE increased to 12.4% for CP, 20.2% for CF, and 21.0% for TCF3 under UV illumination. A similar trend was observed for a lower current density,

where FE increased for all electrodes as the current density decreased. At 25 mA/cm^2, the FE reached 23.1% for CP, 30.0% for CF, and 35.7% for TCF3 under UV illumination. These results confirm that the TiO_2-coated copper foam electrode improves charge utilization during the EMAR process.

The RE followed the opposite trend. At 75 mA/cm^2, the RE was approximately 858 kJ/mol CO_2 for CP, 572 kJ/mol CO_2 for CF, and about 553 kJ/mol CO_2 for TCF3 under UV illumination. As the current density decreased to 25 mA/cm^2, the RE decreased significantly to approximately 296 kJ/mol CO_2 for CP, 244 kJ/mol CO_2 for CF, and about 140 kJ/mol CO_2 for TCF3. These results demonstrate that the optimized TiO_2 coating significantly reduces the energy required for regeneration.

In addition, the applied current density significantly influences the effect of UV illumination. At higher current density, the difference between the UV and dark conditions was relatively small. This indicates the reaction was dominated by externally applied electrons from the power source. Under these conditions, the contribution of photogenerated charge carriers from the TiO_2 coating was comparatively minor. Therefore, the UV and non-UV results were almost similar. However, as the current density decreased, the effect of UV illumination became much more observable. At lower current densities, the electrochemical reaction rate is lower, and the contribution of photogenerated carriers becomes more significant. This leads to higher FE and lower RE under UV illumination.

Parametric studies were conducted to identify the optimal operating conditions for the system. For the variation in copper concentration, the FE increased from 32.8% at 0.05 M Cu to approximately 33.5% at 0.15 M Cu under dark conditions, whereas the maximum FE of 35.7% was obtained at 0.05 M Cu under UV illumination. The regeneration energy decreased from about

200 kJ/mol CO_2 at 0.05 M Cu to approximately 173 kJ/mol CO_2 at 0.15 M Cu under dark conditions. These results indicate that the optimal copper concentration in the absence of UV illumination is around 0.15 M, whereas UV illumination enables comparable or improved performance even at lower copper concentrations.

The influence of amine concentration was also investigated using ethylenediamine (EDA). Both FE and RE improved significantly as the amine concentration increased from 0.25 M to 0.75 M. The maximum FE values of approximately 37.06% (UV On) and 35.37% (UV Off) were obtained at 0.75 M EDA, while the regeneration energy reached its minimum value of approximately 137.98 kJ/mol CO_2 under UV illumination. Increasing the amine concentration further to 1.0 M resulted in only a slight decrease in FE and a small increase in RE, indicating that the optimal amine concentration for the present system is approximately 0.75 M.

The effect of electrolyte flow rate was examined between 25 and 85 mL/min. The highest FE was observed at the lowest flow rate of 25 mL/min, reaching approximately 45.50% under UV illumination. However, the regeneration energy reached its minimum value at an intermediate flow rate of 45 mL/min, indicating a balance between mass transport and residence time effects. Increasing the flow rate beyond this point led to a gradual decrease in FE and an increase in regeneration energy, indicating that the EMAR process is strongly influenced by electrolyte residence time.

Overall, the results demonstrate that combining TiO_2 aerogel-coated electrodes with UV illumination can enhance the electrochemical performance of EMAR systems. The optimized operating window identified in this study corresponds to the use of the TCF3 electrode, an approximately 0.15 M copper concentration (or lower under UV assistance), a 0.75 M EDA concentration, and an electrolyte flow rate of approximately 45 mL/min. Compared with industry-

relevant benchmarks, conventional thermal amine regeneration typically requires 240 kJ/mol CO2, whereas optimized EMAR systems have reported regeneration energy as low as 50 kJ/mol CO_2. The higher regeneration energy observed in this study reflects system-level limitations, including cell configuration, ohmic resistance, and mass transport constraints. Nevertheless, the relative improvement achieved with TiO_2-coated electrodes under UV illumination highlights the effectiveness of the proposed strategy in enhancing charge transfer and Cu redox kinetics within the framework.

5.2 Contributions of this Work

This study provides several important contributions to the development of a photo-assisted EMAR system for CO_2 capture. First, the work demonstrates the successful integration of TiO_2 aerogel powder onto the copper foam substrate through dip-coating. Also, providing an active electrode surface that is photocatalytic, suitable for electrochemical amine regeneration.

Second, the electrochemical and structural characterization conducted in this study provides insight into the morphology, surface chemistry, and electrochemical behavior of TiO_2 aerogel-coated electrodes. Techniques including SEM, TEM, BET surface area analysis, Raman spectroscopy, XRD, and XPS confirmed the structural integrity and anatase phase of the TiO_2 aerogel materials used in the system.

Third, this work systematically evaluates the effect of UV illumination on the electrochemical regeneration process. The results demonstrate that UV irradiation can improve Faradaic efficiency and reduce the energy required for regeneration under certain operating conditions.

Finally, the parametric studies conducted in this work establish an operational framework for the EMAR system. The study identifies optimal operating ranges for copper concentration, amine concentration, and electrolyte flow rate, which are essential for improving system efficiency and guiding future reactor design.

5.3 Limitations of the Study

Despite the promising results obtained in this work, several limitations were identified during the experimental investigation. One limitation of the system was the instability of gas flow when large amounts of CO_2 were produced during electrochemical regeneration. This occasionally led to fluctuations in the measured gas flow rates and could introduce uncertainty into the calculated Faradaic efficiency.

Another limitation involved the durability of some system components. The electrolyte caused gradual damage to the quartz window used for UV illumination, necessitating a protective layer during experiments. Additionally, the copper foam anode experienced noticeable degradation over extended operation compared to carbon plate electrodes.

The system also required a relatively long stabilization period before reliable data could be collected. This extended startup time increased the duration of experiments and limited the number of repeated tests that could be performed within the available timeframe.

5.4 Recommendations for Future Work

Future studies should focus on improving reactor design and experimental stability to further enhance the performance of UV-assisted EMAR systems. One potential improvement is to optimize the optical path between the UV source and the electrode surface. In the present system, the distance between the quartz window and the electrode was approximately 2.2 cm, which may

reduce the effective light intensity reaching the TiO_2 coating. Reducing this distance or redesigning the illumination geometry could improve photo-assisted effects.

Further research is also required to evaluate the long-term durability of TiO_2 aerogel coatings under continuous electrochemical operation. Investigating coating adhesion, mechanical stability, and potential degradation mechanisms would be important for practical applications.

Additional studies could explore the use of alternative photocatalytic materials or modified TiO_2 structures to enhance light absorption and charge separation. Finally, scaling studies and reactor design optimization would be necessary to evaluate the feasibility of implementing photo-assisted EMAR systems for industrial CO_2 capture applications.

References

[1] Godin J, Liu W, Ren S, Xu CC. Advances in recovery and utilization of carbon dioxide: A brief review. J Environ Chem Eng 2021;9:105644. https://doi.org/10.1016/j.jece.2021.105644.

[2] IPCC. 2018: Global Warming of 1.5°C.An IPCC Special Report on the impacts of global warming of 1.5°C above pre-industrial levels and related global greenhouse gas emission pathways, in the context of strengthening the global response to the threat of climate change, sustainable development, and efforts to eradicate poverty [Masson-Delmotte, V., P. Zhai, H.-O. Pörtner, D. Roberts, J. Skea, P.R. Shukla, A. Pirani, W. Moufouma-Okia, C. Péan, R. Pidcock, S. Connors, J.B.R. Matthews, Y. Chen, X. Zhou, M.I. Gomis, E. Lonnoy, T. Maycock, M. Tignor, and T. Waterfield (eds.)]. In Press. https://www.ipcc.ch/site/assets/uploads/sites/2/2019/06/SR15_Full_Report_High_Res.pdf (accessed December 5, 2024).

[3] Mohee FM, Miller C. Development of a radar based thunderstorm climatology for North Dakota. 24th Conf. Sev. Local Storms Am. Meteorol. Soc. AMS GA USA Am. Metrol. Soc. Retrieved Httpsams Confex Comams24SLStechprogrampaper142135 Htm, 2008.

[4] Zimmermann A, Kant M, Strunge T, Tzimas E, Leitner W, Arlt W, et al. CO_2 utilisation today : report 2017.

[5] Mohee FM, Al-Mayah A. Towards A Mechanical Anchor System For CFRP Plates. Can. Soc. Civ. Eng. CSCE 2017 Annu. Conf. Vanc. BC Can. Soc. Civ. Eng. CSCE, 2017.

[6] SaskPower. Boundary Dam Carbon Capture Project. 2024. https://www.saskpower.com/our-power-future/infrastructure-projects/carbon-capture-and-storage/boundary-dam-carbon-capture-project (accessed December 5, 2024).

[7] SaskEnergy. 'Clean' technology project piloted at Regina airport. 2023. https://www.saskenergy.com/about-us/stories/clean-technology-project-piloted-regina-airport (accessed December 5, 2024).

[8] Carbon Capture Demonstrations Projects Selected and Awarded Projects. EnergyGov 2025. https://www.energy.gov/oced/carbon-capture-demonstrations-projects-selected-and-awarded-projects (accessed January 10, 2025).

[9] IOGP Europe. Map of CO_2 storage Projects in Europe. 2025. https://iogpeurope.org/resource/map-of-eu-ccus-projects/ (accessed January 10, 2025).

[10] Chao C, Deng Y, Dewil R, Baeyens J, Fan X. Post-combustion carbon capture. Renew Sustain Energy Rev 2021;138:110490. https://doi.org/10.1016/j.rser.2020.110490.

[11] Halim A, Mohee FM, Liang RLF, Freire-Gormaly M. Advances in amine-based CO_2 capture technologies and future directions - A comprehensive analysis of absorption, regeneration, and emerging systems. Chem Eng J 2026:172747. https://doi.org/10.1016/j.cej.2026.172747.

[12] Freire-Gormaly M. The pore structure of indiana limestone and pink dolomite for the modeling of carbon dioxide in geologic carbonate rock formations. MASc Thesis. University of Toronto, 2013.

[13] Stern MC, Simeon F, Herzog H, Hatton TA. Post-combustion carbon dioxide capture using electrochemically mediated amine regeneration. Energy Environ Sci 2013;6:2505–17. https://doi.org/10.1039/C3EE41165F.

[14] Freire-Gormaly M, Ellis JS, Bazylak A, MacLean HL. Comparing thresholding techniques for quantifying the dual porosity of Indiana Limestone and Pink Dolomite. Microporous Mesoporous Mater 2015;207:84–9.

[15] Madejski P, Chmiel K, Subramanian N, Kuś T. Methods and Techniques for CO_2 Capture: Review of Potential Solutions and Applications in Modern Energy Technologies. Energies 2022;15:887. https://doi.org/10.3390/en15030887.
[16] Freire-Gormaly M, Bilton AM. Optimization of renewable energy power systems for remote communities. IDETC Conference, vol. 57076, American Society of Mechanical Engineers; 2015,DETC2015-47509, V02AT03A030 https://doi.org/10.1115/DETC2015-47509.
[17] Jansen D, Gazzani M, Manzolini G, Dijk E van, Carbo M. Pre-combustion CO_2 capture. Int J Greenh Gas Control 2015;40:167–87. https://doi.org/10.1016/j.ijggc.2015.05.028.
[18] Mohee FM, Kamal FM. Manufacturing of Nuclear Waste Containers and Flasks: Consideration of Transportation Load, Acceleration Load and Fatigue Load: a Structural Engineering Perspective. 36th Annu. Conf. Can. Nucl. Soc. 40th Annu. CNSCNA Stud. Conf. Tor. ON, 2016.
[19] Scheffknecht G, Al-Makhadmeh L, Schnell U, Maier J. Oxy-fuel coal combustion—A review of the current state-of-the-art. Int J Greenh Gas Control 2011;5:S16–35. https://doi.org/10.1016/j.ijggc.2011.05.020.
[20] Freire-Gormaly M, Ellis J, Maclean H, Bazylak A. Pore Structure Characterization of Indiana Limestone and Pink Dolomite from Pore Network Reconstructions. Oil Gas Sci Technol 2015;71. https://doi.org/10.2516/ogst/2015004.
[21] M. Freire-Gormaly, A.M. Bilton. Experimental quantification of the effect of intermittent operation on membrane performance of solar powered reverse osmosis desalination systems. 2018. Desalination, Volume 435, pp. 188-197, ISSN 0011-9164, https://doi.org/10.1016/j.desal.2017.09.013.
[22] Liang Z, Rongwong W, Liu H, Fu K, Gao H, Cao F, et al. Recent progress and new developments in post-combustion carbon-capture technology with amine-based solvents. Int J Greenh GAS CONTROL 2015;40:26–54. https://doi.org/10.1016/j.ijggc.2015.06.017.
[23] Du J, Yang W, Xu L, Bei L, Lei S, Li W, et al. Review on post-combustion CO_2 capture by amine blended solvents and aqueous ammonia. Chem Eng J 2024;488:150954. https://doi.org/10.1016/j.cej.2024.150954.
[24] Zhang G, Liu J, Qian J, Zhang X, Liu Z. Review of research progress and stability studies of amine-based biphasic absorbents for CO_2 capture. J Ind Eng Chem 2024;134:28–50. https://doi.org/10.1016/j.jiec.2024.01.013.
[25] Shi H, Naami A, Idem R, Tontiwachwuthikul P. Catalytic and non catalytic solvent regeneration during absorption-based CO2 capture with single and blended reactive amine solvents. Int J Greenh Gas Control 2014;26:39–50. https://doi.org/10.1016/j.ijggc.2014.04.007.
[26] Wang M, Herzog HJ, Hatton TA. CO_2 Capture Using Electrochemically Mediated Amine Regeneration. Ind Eng Chem Res 2020;59:7087–96. https://doi.org/10.1021/acs.iecr.9b05307.
[27] Freire-Gormaly M. Experimental characterization of membrane fouling under intermittent operation and its application to the optimization of solar photovoltaic powered reverse osmosis drinking water treatment systems. PhD Thesis. University of Toronto (Canada); 2018.
[28] Kim YE, Moon SJ, Yoon YI, Jeong SK, Park KT, Bae ST, et al. Heat of absorption and absorption capacity of CO2 in aqueous solutions of amine containing multiple amino groups. Sep Purif Technol 2014;122:112–8. https://doi.org/10.1016/j.seppur.2013.10.030.

[29] Freire-Gormaly M, MacLean H, Bazylak A. Microct Investigations and pore network reconstructions of limestone and carbonate-based rocks for deep geologic carbon sequestration. Energy Sustain., vol. 44816, American Society of Mechanical Engineers; 2012, p. 863–6.
[30] Hikita H, Asai S, Katsu Y, Ikuno S. Absorption of carbon dioxide into aqueous monoethanolamine solutions. AIChE J 1979;25:793–800. https://doi.org/10.1002/aic.690250507.
[31] Freire-Gormaly M, Bilton AM. Impact of intermittent operation on reverse osmosis membrane fouling for brackish groundwater desalination systems. J Membr Sci 2019;583:220–30.
[32] Zoannou K-S, Sapsford DJ, Griffiths AJ. Thermal degradation of monoethanolamine and its effect on CO_2 capture capacity. Int J Greenh Gas Control 2013;17:423–30.
[33] Horrigan L, Freire-Gormaly M. Modelling the effects of ultrasonic sonification on reverse osmosis feed channel temperature. Desalination 2022;521:115332. https://doi.org/10.1016/j.desal.2021.115332.
[34] Yang C, Li T, Sema T, Tantikhajorngosol P, Jiang J, Bai X, et al. Heat and mass transfer of a novel CO_2 desorption process integrated with highly turbulent catalytic heat exchanger. Fuel 2024;359:130028. https://doi.org/10.1016/j.fuel.2023.130028.
[35] Mohd Rozaiddin SA, Lau KK. A Review on Enhancing Solvent Regeneration in CO_2 Absorption Process Using Nanoparticles. Sustainability 2022;14:4750. https://doi.org/10.3390/su14084750.
[36] Akeeb O, Wang L, Xie W, Davis R, Alkasrawi M, Toan S. Post-combustion CO_2 capture via a variety of temperature ranges and material adsorption process: A review. J Environ Manage 2022;313:115026. https://doi.org/10.1016/j.jenvman.2022.115026.
[37] Grande CA, Ribeiro RPPL, Rodrigues AE. Challenges of Electric Swing Adsorption for CO_2 Capture. ChemSusChem 2010;3:892–8. https://doi.org/10.1002/cssc.201000059.
[38] Piluk TD, Faccio G, Letsiou S, Liang R, Freire-Gormaly M. A critical review investigating the use of nanoparticles in cosmetic skin products. Environ Sci Nano 2024;11:3674–92.
[39] Wang M, Hariharan S, Shaw RA, Hatton TA. Energetics of electrochemically mediated amine regeneration process for flue gas CO_2 capture. Int J Greenh Gas Control 2019;82:48–58. https://doi.org/10.1016/j.ijggc.2018.12.028.
[40] Wu X, Mao Y, Fan H, Sultan S, Yu Y, Zhang Z. Investigation on the performance of EDA-based blended solvents for electrochemically mediated CO_2 capture. Appl Energy 2023;349:121656. https://doi.org/10.1016/j.apenergy.2023.121656.
[41] Vinayakumar K, Palliyarayil A, Kumar NS, Sil S. Processing of aerogels and their applications toward CO_2 adsorption and electrochemical reduction: a review. Environ Sci Pollut Res 2022;29:47942–68. https://doi.org/10.1007/s11356-022-20355-2.
[42] Liang RLF, Snowdon M, Fattahi A, Cameron D, et al, 2026, Ultrasonic Processing of Graphene Nanoplatelet−Silver Nanoparticle Composite Coatings for Enhanced Mechanical and Antiviral Properties in Medical Textiles, ACS Omega, In Press, https://doi.org/10.1021/acsomega.5c06675.
[43] Begag R, Krutka H, Dong W, Mihalcik D, Rhine W, Gould G, et al. Superhydrophobic amine functionalized aerogels as sorbents for CO_2 capture. Greenh Gases Sci Technol 2013;3:30–9. https://doi.org/10.1002/ghg.1321.
[44] Kataoka T, Orita Y, Shimoyama Y. Photo-thermal CO_2 desorption from amine-modified silica/carbon aerogel for direct air capture. Chem Eng J 2024;482:148710.

[45] Wang M, Rahimi M, Kumar A, Hariharan S, Choi W, Hatton TA. Flue gas CO_2 capture via electrochemically mediated amine regeneration: System design and performance. Appl Energy 2019;255:113879. https://doi.org/10.1016/j.apenergy.2019.113879.
[46] Wu X, Fan H, Sharif M, Yu Y, Wei K, Zhang Z, et al. Electrochemically-mediated amine regeneration of CO_2 capture: From electrochemical mechanism to bench-scale visualization study. Appl Energy 2021;302:117554. https://doi.org/10.1016/j.apenergy.2021.117554.
[47] Freire-Gormaly M, Ellis JS, Bazylak A, MacLean HL. Pore Network Reconstructions and Pore-Scale Characterization of Limestone and Carbonate-Based Rocks for Deep Geologic Carbon Sequestration. 223rd ECS Meeting (May 12-17, 2013), 2013.
[48] Nessi E, Papadopoulos AI, Seferlis P. A review of research facilities, pilot and commercial plants for solvent-based post-combustion CO_2 capture: Packed bed, phase-change and rotating processes. Int J Greenh Gas Control 2021;111:103474. https://doi.org/10.1016/j.ijggc.2021.103474.
[49] Snowdon MR, Rathod S, Liang RLF, Freire-Gormaly M. Architecting Durability: Synergies in Assembly, Self-Repair, and Advanced Characterization of Carbon Nanotube Materials. Nanomaterials 2025;15:1352.
[50] Raganati F, Ammendola P. CO_2 Post-combustion Capture: A Critical Review of Current Technologies and Future Directions. Energy Fuels 2024;38:13858–905. https://doi.org/10.1021/acs.energyfuels.4c02513.
[51] Snowdon MR, Sukhanova EV, Popov ZI, Li S, Nurdiwijayanto L, Taniguchi T, et al. Iptycene-Assisted Alignment of Chirality-Sorted SWCNTs for Field-Effect Transistors. ACS Appl Nano Mater 2025;8:944–51. https://doi.org/10.1021/acsanm.4c04305.
[52] Liu S, Gao H, He C, Liang Z. Experimental evaluation of highly efficient primary and secondary amines with lower energy by a novel method for post-combustion CO_2 capture. Appl Energy 2019;233–234:443–52. https://doi.org/10.1016/j.apenergy.2018.10.031.
[53] Bishnoi S, Rochelle GT. Absorption of carbon dioxide in aqueous piperazine/methyldiethanolamine. AIChE J 2002;48:2788–99. https://doi.org/10.1002/aic.690481208.
[54] Bernhardsen IM, Knuutila HK. A review of potential amine solvents for CO_2 absorption process: Absorption capacity, cyclic capacity and pKa. Int J Greenh Gas Control 2017;61:27–48. https://doi.org/10.1016/j.ijggc.2017.03.021.
[55] Horrigan L, Liang RLF, Freire-Gormaly M. Modelling ultrasonic cavitation onset in spiral-wound reverse osmosis modules. Desalination Water Treat 2024;320:100597. https://doi.org/10.1016/j.dwt.2024.100597.
[56] Sakwattanapong R, Aroonwilas A, Veawab A. Behavior of Reboiler Heat Duty for CO_2 Capture Plants Using Regenerable Single and Blended Alkanolamines. Ind Eng Chem Res 2005;44:4465–73. https://doi.org/10.1021/ie050063w.
[57] Gouedard C, Picq D, Launay F, Carrette P-L. Amine degradation in CO_2 capture. I. A review. Int J Greenh Gas Control 2012;10:244–70.
[58] Stern MC, Simeon F, Herzog H, Hatton TA. An Electrochemically-mediated Gas Separation Process for Carbon Abatement. Energy Procedia 2013;37:1172–9. https://doi.org/10.1016/j.egypro.2013.05.214.
[59] Boualavong J, Gorski CA. Electrochemically Mediated CO_2 Capture Using Aqueous Cu(II)/Cu(I) Imidazole Complexes. ACS EST Eng 2021;1:1084–93. https://doi.org/10.1021/acsestengg.1c00068.

[60] Fan H, Mao Y, Wang H, Yu Y, Wu X, Zhang Z. Performance comparation of MEA and EDA in electrochemically-mediated amine regeneration for CO_2 capture. Sep Purif Technol 2023;311:123282. https://doi.org/10.1016/j.seppur.2023.123282.
[61] Snowdon MR, Liang RLF, Kaur A, Burton EA, Rathod S, Fang W, et al. Effects of Substituting Activated Carbon with Titanium-Dioxide-Coated Cenospheres in Conventional Aquarium Filters. Environments 2023;10:188.
[62] Freire-Gormaly M, Bilton A. Optimization of solar powered reverse osmosis water treatment systems. 15th Int. Conf. Environ. Eng. CSCE 2017 Annu. Gen. Conf. Vanc. Br. Columbia May 31-June 3, 2017.
[63] Mohee FM, Al-Mayah A, Plumtree A. Development of a novel prestressing anchor for CFRP plates: Experimental investigations. Compos Struct 2017;176:20–32.
[64] Mao Y, Sultan S, Fan H, Yu Y, Wu X, Zhang Z. Stability improvement of the advanced electrochemical CO_2 capture process with high-capacity polyamine solvents. Appl Energy 2024;369:123597. https://doi.org/10.1016/j.apenergy.2024.123597.
[65] Hassan A, Refaie A, Aleta P, Afshari M, Kalantari E, Fang Y, et al. Reviving the absorbent chemistry of electrochemically mediated amine regeneration for improved point source carbon capture. Chem Eng J 2024:149566.
[66] Mohee FM, Al-Mayah A. Effect of modulus of elasticity and thickness of the CFRP plate on the performance of a novel anchor for structural retrofitting and rehabilitation applications. Eng Struct 2017;153:302–16.
[67] Phadtare VD, Parale VG, Kim T, Lee K-Y, Pathak S, Park H-H. Facile synthesis of a lightweight three-dimensional polymer scaffold dip-coated with multiple layers of TiO_2 aerogel for X-band microwave absorption applications. J Alloys Compd 2020;823:153847. https://doi.org/10.1016/j.jallcom.2020.153847.
[68] Mohee FM, Al-Mayah A, Plumtree A. Friction Characteristics of CFRP Plates in Contact with Copper Plates under High Contact Pressure. J Compos Constr 2016;20:04016022. https://doi.org/10.1061/(ASCE)CC.1943-5614.0000673.
[69] Zhang M, Cheng J, Xuan X, Zhou J, Cen K. Pt/graphene aerogel deposited in Cu foam as a 3D binder-free cathode for CO_2 reduction into liquid chemicals in a TiO_2 photoanode-driven photoelectrochemical cell. Chem Eng J 2017;322:22–32. https://doi.org/10.1016/j.cej.2017.03.126.
[70] Halim A, Marouf L, Bourget F, Liang RLF, Freire-Gormaly M. Optimization of Electrochemical CO_2 Capture with Photocatalytic Aerogel Materials for Minimizing Energy Consumption. 2025. Electrochemical Society Meeting Abstracts 247. Vol. 56, pp. 2732.
[71] Mohee FM, Al-Mayah A. Effect of barrel, wedge material and thickness on composite plate anchor performance through analytical, finite element, experimental and 3D prototype investigations. Eng Struct 2018;175:138–54.
[72] Kortlever R, Shen J, Schouten KJP, Calle-Vallejo F, Koper MTM. Catalysts and Reaction Pathways for the Electrochemical Reduction of Carbon Dioxide. J Phys Chem Lett 2015;6:4073–82. https://doi.org/10.1021/acs.jpclett.5b01559.
[73] Fu Y, Wang G, Mei T, Li J, Wang J, Wang X. Accessible Graphene Aerogel for Efficiently Harvesting Solar Energy. ACS Sustain Chem Eng 2017;5:4665–71. https://doi.org/10.1021/acssuschemeng.6b03207.
[74] Mu P, Bai W, Zhang Z, He J, Sun H, Zhu Z, et al. Robust aerogels based on conjugated microporous polymer nanotubes with exceptional mechanical strength for efficient solar steam generation. J Mater Chem A 2018;6:18183–90. https://doi.org/10.1039/C8TA05698F.

[75] Mohee FM. Development, Analysis and Testing of Innovative Mechanical Prestressing Anchors for CFRP Plates for Structural Rehabilitation and Retrofitting 2017.
[76] Freire-Gormaly M, Bilton AM. 2019. Design of photovoltaic powered reverse osmosis desalination systems considering membrane fouling caused by intermittent operation. Renewable Energy. Vol. 135. pp. 108-121. https://doi.org/10.1016/j.renene.2018.11.065.
[77] Mohee FM. The effects of strain rate on concrete strength under dynamic impact load. J Bangladesh Electron Soc 2016;16:83–90.
[78] McEntee M, Gordon WO, Balboa A, Delia DJ, Pitman CL, Pennington AM, et al. Mesoporous Copper Nanoparticle/TiO_2 Aerogels for Room-Temperature Hydrolytic Decomposition of the Chemical Warfare Simulant Dimethyl Methylphosphonate. ACS Appl Nano Mater 2020;3:3503–12. https://doi.org/10.1021/acsanm.0c00228.
[79] Mohee FM. A review of the Effects and Control of the Mercury Emissions from Cement industry. EIC-Clim. Change Technol. Conf., 2013, p. 1–13.
[80] Rose A, Hofmann A, Voepel P, Milow B, Marschall R. Photocatalytic activity and electron storage capability of TiO_2 aerogels with adjustable surface area.
[81] Sypabekova M, Hagemann A, Rho D, Kim S. Review: 3-Aminopropyltriethoxysilane (APTES) Deposition Methods on Oxide Surfaces in Solution and Vapor Phases for Biosensing Applications. Biosensors 2022;13:36. https://doi.org/10.3390/bios13010036.
[82] Freire-Gormaly M, Bilton A. An experimental system for characterization of membrane fouling of solar photovoltaic reverse osmosis systems under intermittent operation. Desalination Water Treat 2017;73:54–63. https://doi.org/10.5004/dwt.2017.20391.
[83] Mohee FM, Kamal FM. Application of high-strength composite materials for the nuclear waste containers and flasks. Can. Soc. Civ. Eng. CSCE 2017 Annu. Conf. Vanc. Can., 2017.
[84] Pai KRN, Anjusree GS, Deepak TG, Subash D, Nair SV, Nair AS. High surface area TiO_2 nanoparticles by a freeze-drying approach for dye-sensitized solar cells. RSC Adv 2014;4:36821–7. https://doi.org/10.1039/C4RA04226C.
[85] C. Stern M, Alan Hatton T. Bench-scale demonstration of CO_2 capture with electrochemically-mediated amine regeneration. RSC Adv 2014;4:5906–14. https://doi.org/10.1039/C3RA46774K.
[86] Li W, Lv G, Liu M, Zhao F, Shuai P, Feng Y, et al. Photothermal-driven enhancing photocatalysis and photoelectrocatalysis: Advances and perspectives. J Energy Chem 2025;108:332–60. https://doi.org/10.1016/j.jechem.2025.04.027.
[87] Jilani A, Ibrahim H. Development in Photoelectrochemical Water Splitting Using Carbon-Based Materials: A Path to Sustainable Hydrogen Production. Energies 2025;18. https://doi.org/10.3390/en18071603.